Quantitative assessment of factors contributing to variations in sea surface pCO_2 in the polar oceans

（極域海洋における海洋表面二酸化炭素分圧の季節変化の定量評価）

Division of Marine Bioresource and
Environmental Science
Graduate School of Fisheries Sciences
Hokkaido University
北海道大学大学院水産科学院
海洋生物資源科学専攻

Manami Tozawa
戸澤　愛美

2025 年

Table of Contents

1. General Introduction

Atmospheric carbon dioxide (CO_2) uptake by the oceans

Global warming has become a serious issue in recent years. The Sixth Assessment Report of the Intergovernmental Panel on Climate Change (IPCC, 2021) has stated that the global mean temperature in 2010–2019 was +1.06˚C above the baseline in 1850–1900. This report indicates that the main driver of this temperature increase is emissions of greenhouse gases, of which carbon dioxide (CO_2) is the most significant. Atmospheric CO_2 concentrations increased from 278 ppm in 1750 before the Industrial Revolution (Gulev et al., 2021) to 419 ppm in 2023 (Lan et al., 2023). The cause of this rise in atmospheric CO_2 concentrations has been attributed to human activities, such as burning of fossil fuels and land use change. The majority of emitted CO_2 remains in the atmosphere and raises atmospheric CO_2 concentrations, although some is absorbed by terrestrial plants and the oceans. According to Friedlingstein et al. (2023), terrestrial plants absorbed 3.3 ± 0.8 Gt C, and the ocean absorbed 2.8 ± 0.4 Gt C of the 11.1 ± 0.8 Gt C of anthropogenic CO_2 emissions in 2022.

The ocean can uptake and store atmospheric CO_2 for long periods and is important in limiting the increase in atmospheric CO_2 concentrations. The air–sea CO_2 flux is mainly determined by the difference in partial pressure of CO_2 (pCO_2) between the ocean and the atmosphere. Although the atmospheric CO_2 concentration is consistently rising, the short-term and spatial changes are small. Therefore, observations of sea surface pCO_2 are necessary to estimate the seasonal changes and spatial distribution of the air-sea CO_2 flux. About 38.6 million pCO_2 measurements data have been recorded in the Surface Ocean CO_2 Atlas (SOCAT) database (Bakker et al., 2016; available at https://www.socat.info/) since major sea surface pCO_2 observations began in 1957 (Takahashi et al., 1961).

CO_2 uptake and environmental change in the polar oceans

The Arctic Ocean and the Southern Ocean are areas with high CO_2 solubility and low pCO_2 due to low water temperature; thus, large amounts of CO_2 are absorbed from the atmosphere into the polar oceans. Friedlingstein et al. (2023) estimated that the CO_2 influx was 0.1–0.2 Gt C year^{-1} in the Arctic Ocean and 1.5–1.6 Gt C year^{-1} in the Southern Ocean. The CO_2 absorption into the polar

oceans accounts for about half of the total CO_2 absorption by the global ocean and plays an important role in the carbon cycle. However, it is also well known that environmental change greatly affects these oceans. For example, the Arctic is warming nearly four times faster than the global average (Rantanen et al., 2022), and the smallest sea ice extent since satellite sea ice observations began in 1978 (3.4×10^6 km^2) was recorded in September 2012 (Parkinson & Comiso, 2013). In the Southern Ocean, melting ice shelves and glacier outflow are progressing (Smith et al., 2020), and that progression is associated with a rise in sea level. Environmental changes, such as rising temperatures and reduced sea ice cover, will significantly alter the oceanic carbon cycle, affecting the amount of CO_2 absorption in the Arctic and Southern Oceans. Future predictions of changes of CO_2 absorption in the polar oceans require clarification of the relationship between environmental changes and CO_2 absorption. Therefore, it is necessary to quantitatively assess the factors driving the changes in polar sea surface pCO_2.

Factors contributing to the variability of sea surface pCO_2

Several factors affect sea surface pCO_2, including water temperature, freshwater inflow, and biological activity (e.g., Bates et al., 2006). A decrease of CO_2 solubility due to warming causes pCO_2 to increase. Changes in pCO_2 are also caused by dilution of carbonate components and increase of solubility due to glacial melting and river water inflows. In addition, sea surface pCO_2 decreases when organisms take up CO_2. There have been some previous studies on the drivers of pCO_2 variation in the polar oceans; however, the majority of these studies qualitatively evaluated pCO_2 changes (e.g., Burgers et al., 2017) or quantitatively assessed changes in dissolved inorganic carbon (DIC) or total alkalinity (TA) (e.g., Jones et al., 2020). Therefore, there have been fewer studies of quantitative assessments of the factors driving pCO_2 changes. Future predictions of CO_2 uptake require quantitative evaluation of the relationship between changes of pCO_2 and environmental changes, including temperature variations, freshwater inflow, and biological activity. It is also critical to understand the surrounding ocean and sea ice environment because they affect the factors driving pCO_2 changes. For example, the impact of freshwater inflow depends on the carbonic acid component in sea ice and the impact of variations of biological activity with nutrients. The environmental changes described above will also alter the type of sea ice and the distribution of nutrients. Therefore, we also need to understand surrounding biogeochemical environments.

In this paper, we focus on seasonal changes of pCO_2 in the seasonal sea ice zone of the polar oceans

and suggest a new approach to quantitatively assess the drivers of seasonal change. Chapter 2 suggests a new assessment approach by using observation data from the Southern Ocean's East Indian Ocean sector in 2018/2019. In Chapter 3, we show the relationship between the nutrients contributing to biological activity and the frontal structure, which has changed on a decadal scale, based on the same observation data. Chapter 4 presents a study that improves the assessment approach suggested in Chapter 2 by using data from observations in the Pacific sector of the Arctic Ocean in 2021. We also use data from sea ice observations to describe the carbonate components of sea ice and the impacts of melting.

References

Bakker, D. C. E., Pfeil, B., Landa, C., Metzl, N., O'Brien, K., Olsen, A., et al. (2016). A multi-decade record of high-quality *f*CO_2 data in version 3 of the Surface Ocean CO_2 Atlas (SOCAT), *Earth System Science Data*, 8(2), 383–413. https://doi.org/10.5194/essd-8-383-2016

Bates, N. R., Moran, S. B., Hansell, D. A., Mathis, J. T. (2006). An increasing CO_2 sink in the Arctic Ocean due to sea-ice loss, *Geophysical Research Letters*, 33, L23609. https://doi.org/10.1029/2006GL027028

Burgers, T. M., Miller, L. A., Thomas, H., Else, B. G. T., Gosselin, M., Papakyriakou, T. (2017). Surface water *p*CO_2 variations and sea−air CO_2 fluxes during summer in the Eastern Canadian Arctic, *Journal of Geophysical Research: Oceans*, 122, 9663− 9678. https://doi.org/10.1002/2017JC013250

Friedlingstein, P., O'Sullivan, M., Jones, M. W., Andrew, R. M., Bakker, D. C. E., et al. (2023). Global Carbon Budget 2023, *Earth System Science Data*, 15, 5301–5369, https://doi.org/10.5194/essd-15-5301-2023

Gulev, S.K., P.W. Thorne, J. Ahn, F.J. Dentener, C.M. Domingues., et al. (2021). Changing State of the Climate System. In *Climate Change 2021: The Physical Science Basis. Contribution of Working Group I to the Sixth Assessment Report of the Intergovernmental Panel on Climate Change* [Masson-Delmotte, V., P. Zhai, A. Pirani, S.L. Connors, C. Péan, S. Berger, N. Caud, Y. Chen, L. Goldfarb, M.I. Gomis, M. Huang, K. Leitzell, E. Lonnoy, J.B.R. Matthews, T.K. Maycock, T.

Waterfield, O. Yelekçi, R. Yu, and B. Zhou (eds.)]. Cambridge University Press, Cambridge, United Kingdom and New York, NY, USA, pp. 287–422, doi:10.1017/9781009157896.004

IPCC, 2023: *Climate Change 2023: Synthesis Report.* Contribution of Working Groups I, II and III to the Sixth Assessment Report of the Intergovernmental Panel on Climate Change [Core Writing Team, H. Lee and J. Romero (eds.)]. IPCC, Geneva, Switzerland, pp. 35–115, doi: 10.59327/IPCC/AR6-9789291691647

Jones, E. M., Renner, A. H. H., Chierici, M., Wiedmann, I., Lødemel, H. H., Biuw, M. (2020). Seasonal dynamics of carbon-ate chemistry, nutrients and CO_2uptake in a sub-Arctic fjord, *Elementa: Science of the Anthropocene* 8: 41. https://doi.org/10.1525/elementa.438

Lan, X., Tans, P., K.W. Thoning: Trends in globally-averaged CO_2 determined from NOAA Global Monitoring Laboratory measurements. Version Thursday, 05-Dec-2024 13:43:51 MST https://doi.org/10.15138/9N0H-ZH07

Lan, X., Tans, P., K.W. Thoning: Trends in globally-averaged CO_2 determined from NOAA Global Monitoring Laboratory measurements. Version 2024-11 https://doi.org/10.15138/9N0H-ZH07

Parkinson, C. L. and Comiso, J. C. (2013). On the 2012 record low Arctic sea ice cover: Combined impact of preconditioning and an August storm, *Geophysical. Research Letters*, 40, 1356−1361, doi:10.1002/grl.50349

Rantanen, M., Karpechko, A.Y., Lipponen, A., et al. (2022). The Arctic has warmed nearly four times faster than the globe since 1979. *Communications Earth & Environment* 3, 168. https://doi.org/10.1038/s43247-022-00498-3

Smith, B. H. A., Fricker, A. S., Gardner, B., Medley, J., Nilsson, F. S., et al. (2020). Pervasive ice sheet mass loss reflects competing ocean and atmosphere processes, *Science*, 368(6496),1239-1242

Takahashi, T. (1961). Carbon dioxide in the atmosphere and in Atlantic Ocean water, *Journal of Geophysical Research*, 66 (2), 477–494, doi:10.1029/JZ066i002p00477

2. Seasonal variations and drivers of surface ocean pCO_2 in the Seasonal Ice Zone of the Eastern Indian Sector, Southern Ocean

Abstract

To quantitatively assess the inorganic carbon cycle in the eastern Indian sector of the Southern Ocean (80–150˚E, south of 60˚S), we measured ocean surface temperature, salinity, alkalinity (TA), the partial pressure of carbon dioxide (pCO_2), and concentrations of chlorophyll-*a* (chl.*a*), dissolved inorganic carbon (DIC), and nutrients during the KY18 survey (December 2018–January 2019). The sea–air CO_2 flux in this region was –8.3 ± 12.7 mmol m^{-2} day^{-1} (–92.1 to +10.6 mmol m^{-2} day^{-1}). The ocean was therefore a weak CO_2 sink. Based on the DIC and TA in the temperature minimum layer, we estimated the change of pCO_2 from winter to summer (δpCO_2) due to changes in water temperature, salinity, and biological activity. We assumed that the temperature and salinity of seawater in the temperature minimum layer were –1.8˚C and 34.25, respectively. The spatial distribution of pCO_2 in the western part (80–110˚E) of the study area was mainly driven by biological activity, which decreased pCO_2 from December to early January, and in the eastern part (110–150˚E) by temperature, which increased pCO_2 from January to February. We also examined the changes in the CO_2 concentrations (xCO_2) over time by comparing data from 1996 with our data (2018–2019). The oceanic and atmospheric xCO_2 increased by 23 ppm and 45 ppm in 23 years, respectively. These changes of ocean xCO_2 was mainly driven by an increase of CO_2 uptake from the atmosphere as a result of the rise in atmospheric xCO_2 and increase in biological activity associated with the change in the water-mass distribution.

2.1. Introduction

The ocean has absorbed about 25% of the CO_2 emitted to the atmosphere as results of human activities, primarily fossil fuel burning and deforestation, via gas exchange with the atmosphere at the ocean surface (Friedlingstein et al., 2021). The Southern Ocean south of 30˚S, in particular, is responsible for nearly half of the total oceanic CO_2 absorption and plays a fundamental role in the global carbon cycle (Sabine et al., 2004; Takahashi et al., 2012). In the seasonal ice zone of the Southern Ocean (south of 60˚S), atmosphere−ocean CO_2 exchange varies seasonally and is known to act as a weak sink throughout the year (Takahashi et al., 2012). The formation and melting of sea ice cause significant seasonal changes in the characteristics of the physical environment, including

light, temperature, and salinity (Williams et al., 2010). Seasonal changes associated with sea ice are expected to further affect the carbon cycle. Assessment of the seasonal carbon budget facilitates evaluation of the effect of climate change on the CO_2 uptake ability of the Southern Ocean (Sallée, 2018).

The partial pressure of CO_2 (pCO_2) is one of the factors that control sea−air CO_2 exchange. Surface CO_2 flux is proportional to the downgradient of pCO_2 in the atmosphere and ocean (Wanninkhof, 2014). The surface ocean pCO_2 is affected by CO_2 production/consumption due to biological activities, dilution by sea ice/glacial meltwaters, temperature changes, and mixing with ambient water masses (Legge et al., 2017; Shadwick et al., 2017; Arroyo et al., 2019). The decrease of the solubility of CO_2 with increasing water temperature and salinity in turn increases pCO_2 in the ocean. In the Southern Ocean, as sea surface temperature increases from winter to summer, primary production increases and salinity decreases because of the inflow of freshwater from melting sea ice and glacial ice. Several previous studies have pointed out these seasonal effects (Nakaoka et al., 2009; Nomura, 2014; Legge, 2017; Shadwick et al., 2017; Arroyo et al., 2019; Kiuchi et al., 2021). For example, Nakaoka et al. (2009) indicated that water column stratification and biology influence oceanic pCO_2. However, quantitative understanding of the seasonal cycle of pCO_2 is lacking because the effects of each controlling factor have not been quantified.

The discovery by Nomura et al. (2014) that pCO_2 is highly correlated with sea surface temperature in the Indian Ocean sector of the seasonal ice zone (64−67˚S, 32−58˚E) indicates that the main driver of pCO_2 variability from winter to summer is surface warming. However, Shim et al. (2006) have shown that the decrease of pCO_2 due to biological uptake exceeded the increase of pCO_2 due to increases of temperature from 54˚S to 60˚S along 52˚W in 2001. Close to the continental margin, the decrease of dissolved inorganic carbon (DIC) of seawater by meltwater from sea ice and glacial ice leads to a reduction of pCO_2 and enhancement of atmospheric CO_2 uptake (Bates et al., 2014; Kiuchi et al, 2021). The results of Bates et al. (2014) and Kiuchi et al. (2021) likely contain a spatiotemporal measurement bias associated with the icescape because the icescape is expected to precondition the surface environment (Deppelar and Davidson, 2017). Understanding the carbon cycle in the Antarctic seasonal ice zone requires eliminating the regional specificity of the data and obtaining highly accurate and diverse data for carbonate chemistry.

The BROKE (Baseline Research on Oceanography, Krill and the Environment) experiment (Bindoff et al., 2000; Nicol et al., 2000) and the BROKE−West experiment (Williams et al., 2010;

Nicol et al., 2010) were the synoptic-scale multidisciplinary hydrographic studies in the Indian sector of the Antarctic margin. Although oceanographic data from 80˚E to 150˚E were also obtained during the BROKE study in 1996, data on the carbon cycle during the survey have not been reported. BROKE−West was conducted in 2006 and spanned longitudes of 30–80˚E. Roden et al. (2016) have studied the seasonal changes of pCO_2 within a wide area of the seasonal ice zone. Their study estimated drivers of the changes of carbonate composition by using the pCO_2/oxygen saturation ratio of the ocean to the atmosphere. The ocean pCO_2 was supersaturated with respect to the atmosphere during the winter, and the reduction of the release of CO_2 to the atmosphere from winter to summer by a combination of sea ice melt and biological production indicated that the distribution of sea ice was an important determinant of air-sea CO_2 exchange. Significant changes have taken place in the marine environment of the Indian sector during the two decades since the BROKE study (Auger et al. 2021). For example, Yamazaki et al. (2021) have shown that the Southern Boundary (SB) of Antarctic Circumpolar Current (ACC) moved southward from 1996 to 2019. This caused changes in the distribution of nutrients and might influence on the seasonal variability of pCO_2. In this work we evaluate the decadal changes in the regional carbon cycle.
In this study, the carbonate system within the BROKE region was investigated using data from the multidisciplinary ecosystem survey of the eastern Indian sector (80−150˚E) under the auspices of the Commission for the Conservation of Antarctic Marine Living Resources. The study, which was focused on Antarctic krill, included the collection of water samples from the R/V *Kaiyo–Maru* during 2018/19. The spatial distribution of ocean surface pCO_2 obtained from continuous surface observations was used to quantitatively assess the seasonal variations of pCO_2 and the drivers of those variations in the study region. Revisitation of the stations sampled during the BROKE survey facilitated investigation of variations between 1996 and 2019 of the CO_2 concentrations.

2.2. Materials and Methods

2.2.1. Sampling

We sampled from the R/V *Kaiyo−Maru* (2942 gross metric tons; Fisheries Agency of Japan) in the eastern Indian sector of the Southern Ocean from 12 December 2018 to 8 January 2019 (Leg 1) (60−66˚S, 80−120˚E) and 25 January to 24 February 2019 (Leg 2) (60−65˚S, 113−150˚E) (Figure 2.1). These areas include the full longitudinal range of CCAMLR (The Commission for the Conservation of Antarctic Marine Living Resources) Division 58.4.1 and some parts of Division

58.4.3.b. We henceforth refer to this survey as KY18.

During the cruise, seawater was taken continuously from a depth of about 6 m and introduced into a tandem-type equilibrator, and the CO_2 concentration in the surface water (mole fraction of CO_2 in dry air; $xCO_{2\ sea}$) was measured continuously in the air equilibrated with seawater using an automated CO_2-measuring system (model: MOG−701, Kimoto Electric Co., Ltd., Japan; Fransson et al., 2006). A nondispersive infrared gas analyzer (NDIR; Model 6262, LI−COR, Inc., Lincoln, NE, USA) was used as the detector for measurements of CO_2 concentrations. The analyzer was calibrated every 12 h with four CO_2 standards (275.38, 337.78, 399.22, and 459.88 ppm) traceable to the World Meteorological Organization mole fraction scale. The precision of the pCO_2 measurements with the NDIR analyzer was less than 1 μatm (González-Dávila et al., 2010). The rise of seawater temperature between the intake and the measurement was typically 0.9 ± 0.3˚C. The water temperature was measured using a thermal resistance bulb (model PTR−FD, Meiyo Electric Co., Ltd., Tokyo, Japan) attached to the water intake (about 6-m depth), and temperature corrections were made based on comparisons with the temperatures recorded with the CTD and SBE sensors. The effect of the temperature rise on the measured value of pCO_2 was corrected using the isochemical temperature dependence of pCO_2 given by Copin-Montegut (1988).

Sea surface temperature (SST), salinity (SSS), and fluorescence were measured continuously with an electronic plankton counting and sizing system (EPCS, Nippon Kaiyo Co., Ltd., Tokyo, Japan). The precisions of the temperature and salinity measured with the SBE 3 plus and SBE-4C (Sea-Bird Scientific, Bellevue, WA, USA) were ±0.005˚C and ±0.001, respectively. These temperatures were slightly biased by the temperature rise of the seawater while it was being collected. The precision of the fluorometer (Model−10AU, Turner Designs, Inc., Sunnyvale, CA, USA) was 0.03 μg L^{-1} based on duplicate samples. The fluorescence was converted to a chl *a* concentration based on the relationships between fluorescence and chl *a* concentrations determined on the basis of sampling with another fluorometer (Model−10AU, Turner Designs, Inc., Sunnyvale, CA, USA) of the same water sample. The detection limit of the other fluorometer was 0.025 μg L^{-1}. Samples for total alkalinity (TA) and concentrations of DIC, nutrients, and chl *a* were taken from the underway water sampling system.

Vertical profiles of temperature and salinity were measured with a conductivity-temperature-depth (CTD) probe (SBE 9 plus, Sea-Bird Scientific, Bellevue, WA, USA) that was calibrated by the manufacturer before and after the cruise. The precisions of the temperature and salinity measured

with the SBE 9 plus were ±0.001˚C and ±0.002, respectively. In addition, seawater samples were taken to calibrate the salinity sensor. Seawater samples were collected vertically in rosette-mounted, 10-L Niskin bottles (Ocean Test Equipment, Inc., Lauderdale, FL, USA) for TA, concentrations of DIC, nutrients, and chl *a*.

Seawater was subsampled into (1) a 200-mL glass vial (Maruemu Co., Ltd., Osaka, Japan) for measurement of DIC and TA, (2) a 10-mL polyethylene screw-cap vial (Eiken Chemical Co., Ltd, Tokyo, Japan) for measurement of inorganic nutrient concentration (NO_3^-), and (3) a 500-mL Nalgene polycarbonate bottle (Thermo Fisher Scientific, Inc., Waltham, MA, USA) for measurement of the chl *a* concentration. Teflon tubing was used to transfer DIC and TA samples from the Niskin bottle to a 200-mL bottle. To avoid bubble formation during transfer, seawater was filled smoothly from the bottom of the bottle using Teflon tubing and overflowed by 200 mL (Dickson et al., 2007).

Immediately after subsampling for DIC and TA, a 6.0% (wt.) mercuric chloride ($HgCl_2$) solution (200 µL) was added to the samples for DIC and TA in a 200-mL glass vial to stop biological activity. Samples for DIC and TA were stored at room temperature (+20˚C). Samples for nutrient analyses were stored in a freezer (–30˚C). Samples for chl *a* measurements were immediately filtered through 25-mm-diameter Whatman GF/F filters. Chlorophyll pigments on the filters were then extracted with dimethylformamide (Suzuki and Ishimaru, 1990) for 24 h.

2.2.2. Sample analysis

The DIC of seawater was determined by coulometry (Johnson et al., 1985 and 1992) using a hand-made CO_2 extraction system (Ono et al., 1998) and a coulometer (CM5012, UIC, Inc., Binghamton, NY, USA). The TA of seawater was determined by titration (Dickson et al., 2007) using a TA analyzer (ATT-05, Kimoto Electric Co., Ltd., Japan). Both DIC and TA measurements were calibrated with reference seawater materials (Batch AR; KANSO Technos Co., Ltd., Osaka, Japan) traceable to the Certified Reference Material distributed by Prof. A. G. Dickson (Scripps Institution of Oceanography, La Jolla, CA, USA). The standard deviations of the DIC and TA measurements, calculated from 10 subsamples taken from reference water with a DIC value of 2049.9 µmol kg^{-1} and a TA value of 2301.3 µmol kg^{-1}, were less than 2.0 µmol kg^{-1} and 2.0 µmol kg^{-1}, respectively.

The concentrations of NO_3^- in the seawater were determined in accord with the Joint Global Ocean Flux Study (JGOFS) spectrophotometric method (JGOFS, 1994) using auto-analyzer systems: a QuAAtro 2-HR system (BL-tec, Osaka, Japan) and a Seal Analytical system (Norderstadt, Germany). The analyzers were calibrated with reference materials for nutrient analysis (Lots BZ, CB, and CC; KANSO Technos Co., Ltd.). The standard deviations of the nutrient concentrations, calculated from 20 subsamples taken from reference water samples (KANSO Technos Co., Ltd.) with NO_3^- concentrations of 9.8 μmol L^{-1} were 0.3 μmol L^{-1}.

The concentrations of chl *a* determined with a fluorometer (Model-10AU, Turner Designs, Inc., Sunnyvale, CA, USA) were measured in accord with the method described by Parsons et al. (1984). Standards (0.28–282.30 μg L^{-1} chl *a*) prepared from a liquid chl *a* standard (Wako Pure Chemical Industries, Ltd., Osaka, Japan) by stepwise dilution with N,N-dimethylformamide were used to calibrate the fluorometer before chl *a* measurements.

2.2.3. Sea–air CO_2 Flux Calculations

The sea–air CO_2 flux was calculated with the following equation:

$$F_{sea–air} = k\,\alpha\Delta pCO_2, \qquad (1)$$

where k is the gas transfer velocity (Wanninkhof et al., 2013), α is the CO_2 solubility (Weiss, 1974), and ΔpCO_2 is the difference in pCO_2 between the sea surface and the atmosphere. A negative flux indicates absorption of atmospheric CO_2 by the ocean. The gas transfer velocity was computed using measured wind speeds. We used the wind speed measured by the ship-board anemometer and the monthly mean atmospheric CO_2 concentration measured at Syowa station (https://www.esrl.noaa.gov/gmd/dv/iadv/). The pCO_2 air/sea was then calculated from the air/sea CO_2 concentration, the barometric pressure, and the saturated water vapor pressure (Weiss and Price, 1980).

2.2.4. Determination of seasonal changes in $pCO_{2\,sea}$ and their drivers

To correct for the effect of dilution on DIC and TA due to the melting of sea ice from winter to

summer, DIC and TA data were normalized (nDIC and nTA) to a salinity of 34.25, the mean value of the temperature minimum layer (TML). Tomczak and Liefrink (2005) have proposed that the water mass beneath the summer surface water with a temperature between −1.9 and −1.5˚C and a salinity between 34.2 and 34.5 constitutes the TML. The TML is thought to retain the temperature and salinity from the previous winter. We therefore used a salinity of 34.25 for the normalization of DIC and TA data as an initial condition before the DIC and TA were changed by the input of ice meltwater.

In winter, the properties of water near the surface became vertically uniform because of intensive surface mixing, and winter mixing reset the biogeochemical changes that had occurred during the previous summer. If the subsurface diffusion of winter water is not vigorous, the TML found in summer likely represents surface conditions during the preceding winter (Pondaven et al., 2000; Tomczak and Liefrink, 2005). We then estimated the distribution and seasonal changes of the carbonate system parameters (DIC and TA) at the surface in winter using data from the TML, which we defined by $-1.9^{\circ}C < T < -1.5^{\circ}C$, $34.2 < S < 34.5$ in accord with Tomczak and Liefrink (2005). By assuming that the SST was −1.8˚C and the SSS was 34.25 under the sea ice in winter, we could calculate the $pCO_{2\ sea}$ from the DIC and TA in the TML (sention 2.2) using CO2SYS ver. 02.05 (Orr et al., 2018). We used the carbonic acid dissociation constants (K1 and K2) of Mehrbach et al. (1973) as revised by Dickson and Millero (1987). The $KHSO_4$ was determined in accord with Dickson (1990).

To estimate the effects of biological activity and changes in temperature and salinity on $pCO_{2\ sea}$ through the year, the following procedure was followed. Seasonal changes of DIC resulting from biological activity could be derived from information on nutrient consumption. We normalized the NO_3^- to a salinity of 34.25 (nN) and calculated the difference, Δ(nN), between the surface and the TML. The Δ(nN) was converted to a normalized change of DIC by multiplying by 7.5 moles DIC per mol NO_3^-, based on the DIC/DIN ratios in the Ross Sea (De Jong and Dunbar, 2017), in which the dominant species were diatoms, as was the case in KY18. We calculated the normalized change of TA, Δ(nTA), in the same way as Δ(nN). By substituting the calculated nDIC, nTA, SST (−1.8˚C), and SSS (34.25) into CO2SYS, we derived the pCO_2 change due purely to biological effects. The temperature-driven change was calculated by substituting the observed SST into the software, and the salinity-driven change was calculated by substituting the diluted DIC and TA derived from the observed SSS. We denoted the differences between the surface (summer) pCO_2 and the temperature minimum (winter) pCO_2 due to each effect as $\delta pCO_{2\ sea\_bio}$, $\delta pCO_{2\ sea\_temp}$, and $\delta pCO_{2\ sea\_sal}$,

respectively. We defined the residual of the observed $pCO_{2\ sea}$ from the sum of $\delta pCO_{2\ sea\_bio}$, $\delta pCO_{2\ sea\_temp}$, and $\delta pCO_{2\ sea\_sal}$ as $\delta pCO_{2\ sea\_others}$. It is likely that the $\delta pCO_{2\ sea\_others}$ was associated with measurement errors and other processes such as atmospheric CO_2 uptake and diffusion of water masses. In addition, $\delta pCO_{2\ sea\_winter\text{-}summer}$ are defined as the difference between the estimated pCO_2 and the observed pCO_2 in winter estimated from the value in TML.

2.2.5. Satellite Images

Satellite images of sea ice concentrations near sampling stations were derived from passive microwave imagery from the Advanced Microwave Scanning Radiometer 2 onboard the GCOM-W satellite provided by the Arctic Data archive System, National Institute of Polar Research (NIPR), Japan (https://ads.nipr.ac.jp/dataset/A20170123-003). The spatial resolution was a 10 km×10 km grid, and the temporal resolution was 1 day. The sea ice concentrations were monthly averages.

Satellite images of the chl *a* concentrations within the research area were derived from the Moderate Resolution Imaging Spectroradiometer (MODIS)-Aqua (originally known as EOS PM-1) data from NASA (https://oceandata.sci.gsfc.nasa.gov/MODIS-Aqua/), specifically the standard Level-3 mapped image products of monthly composite MODIS-aqua chl *a* concentration data. The spatial resolution was a 9 km×9 km grid, and the temporal resolution was monthly; we used monthly composite data in this study.

2.3. Results

2.3.1. Temporal Variations of Surface Environment and CO_2 Fluxes

The SST varied from −1.9 to +4.1˚C, with a mean of 0.0 ± 0.9˚C (mean ± standard deviation, henceforth) (range −1.9 to +2.7˚C) on Leg 1 (December to early January) and +1.8 ± 1.3˚C (range −1.8 to +4.1˚C) on Leg 2 (end of January to February) (Figure 2.2a, b). The SSS varied between 33.0 and 34.5, with a mean of 33.7 ± 0.2 (range 33.0 to 34.3) during Leg 1 and a mean of 33.9 ± 0.2 (range 33.2 to 34.5) during Leg 2 (Figure 2.2c, d). The chl *a* concentrations varied from 0.3 to 2.2 μg L^{-1}, with a mean of 0.7 ± 0.2 μg L^{-1} (range 0.5 to 1.5 μg L^{-1}) during Leg 1 and a mean of 1.0 ± 0.4 μg L^{-1} (range 0.3 to 2.2 μg L^{-1}) during Leg 2 (Figure 2.2e, f). SST and chl *a* distributions were

generally consistent with the typical summer environment in the marginal ice zone associated with sea ice melt and solar heating, whereas the SSS increase was likely related to the large-scale variation of the SSS of the ambient seawater (Yamazaki et al., 2020).

The $pCO_{2\ sea}$ was 358 ± 22 µatm (range 293–413 µatm) during Leg 1 and 348 ± 23 µatm (range 233–485 µatm) during Leg 2 (Figure 2.2g, h). The $pCO_{2\ air}$ was 389 ± 4 µatm. The range of the $\Delta pCO_{2\ sea-air}$ during both legs, −115 to +50 µatm, indicated that the seawater was sometimes supersaturated and at other times undersaturated with CO_2 relative to the atmosphere. The average $\Delta pCO_{2\ sea-air}$ was −31 ± 22 µatm (range −96 to +24 µatm) for Leg 1 and −41 ± 23 µatm (range −115 to +50 µatm) for Leg 2. On average, the seawater was thus undersaturated with respect to CO_2 during the period. The wind speeds were 7.1 ± 3.6 m s^{-1} (range: 0–18.7 m s^{-1}) during Leg 1 and 9.6 ± 4.4 m s^{-1} (range: 0–23.4 m s^{-1}) during Leg 2 (Figure 2.2i, j). Based on these $\Delta pCO_{2\ sea-air}$ and wind speeds, we estimated the sea–air CO_2 flux to be −4.3 ± 5.4 mmol m^{-2} day^{-1} (−35.9 to +4.7 mmol m^{-2} day^{-1}) during Leg 1, −11.9 ± 15.9 mmol m^{-2} day^{-1} (−92.1 to +10.6 mmol m^{-2} day^{-1}) during Leg 2, and −8.3 ± 12.7 mmol m^{-2} day^{-1} for the whole period (Figure 2.2k, l). The seawater was thus a weak sink for atmospheric CO_2 during this study.

Of the 54 sites where there was sampling of the water column, 19 sites had water temperature minima that met the definition given by Tomczak and Liefrink (2005) (−1.9˚C < T < −1.5˚C, 34.2 < S < 34.5) for the TML, which corresponded to seawater that had experienced intensive sea ice formation during the previous winter. The average DIC of 2226 ± 7 µmol kg^{-1} and average TA of 2340 ± 5 µmol kg^{-1} indicated that the properties of this TML water were uniform (Figure 2.2m, n).

2.3.2. Spatial Variations of Surface Environment and CO_2 Fluxes

Figure 2.3 shows the spatial variations of water properties and carbon fluxes. The SST was low (about −0.7˚C) in the western part of KY18, which was sampled during Leg 1, and south of 65˚S (Figure 2.3a). The SST increased towards the northeast. The surface isotherms were generally aligned with the streamlines of the offshore circumpolar current. In contrast, the spatial pattern of SSS was not as systematic as that of SST (Figure 2.3b). In the continental margin at longitudes of 110−130˚E, the scrambled distribution of sites of low and high salinity (33.2–34.3) likely corresponded to localized upwelling of Circumpolar Deep Water (Yamazaki et al., 2020). chl *a* concentrations were generally not high (<1.0 µg L^{-1}), with some exceptions at 120−125˚E (>2.0 µg

L^{-1}) (Figure 2.3c).

The $pCO_{2\ sea}$ was irregularly distributed in space but was generally lower in the eastern part of KY18 (especially at the southern end of 150˚E, where it dropped to 233 μatm) (Figure 2.3d). The spatial distribution of the sea–air CO_2 fluxes was also spatially irregular and reflected the irregular spatial distribution of $pCO_{2\ sea}$ (Figure 2.3e).

2.3.3 Satellite Data

Satellite data on the distribution of sea ice and chl *a* are presented here to give an idea of conditions in KY18 before and during the observation period. Figure 2.4 shows the monthly satellite data of sea ice concentrations from the end of Autumn (1 November) to the end of the observation period (30 April). During Leg 1 (December–January), sea ice was present up to 62˚S west of 100˚E and up to 64˚S east of 100˚E. A comparison with the distribution of sea ice before Leg 1 (Figure 2.4a) revealed that the melting of sea ice to the west of 90˚E was more pronounced in the spring preceding Leg 1(Figure 2.4b, c). By Leg 2 (Figure 2.4c, d), the sea ice had generally retreated to around 65˚S as melting progressed, and the percent cover by sea ice was less than 50% over a wide area.

Figure 2.5 shows monthly satellite estimates of chl *a* concentrations from spring to the end of the observation period. A local bloom south of 66˚S started in December. Subsequently, a summer bloom occurred at 60–66˚S in January and February. Except for the chl *a* concentrations at longitudes of 90–100˚E, the chl *a* concentrations during the summer bloom were not much higher than the high local chl *a* concentrations observed south of 66˚S.

2.4. Discussion

2.4.1 Sea–air CO_2 Flux

The mean sea–air CO_2 flux in the study region of −8.3 ± 12.7 mmol m^{-2} day^{-1} suggested that CO_2 was being absorbed from the atmosphere in KY18. The mean sea–air CO_2 flux reported by Roden et al. (2016), whose observations were made during the same season at 30−80˚E, was −8 ± 21 mmol

m^{-2} day^{-1}, very close to the present results. The maximum uptake was −92.1 mmol m^{-2} day^{-1} and was associated with a maximum wind speed of 23.4 m s^{-1}, in agreement with the mean value of −72.0 mmol m^{-2} day^{-1} reported by De Jong and Dunbar (2017) at Terra Nova Bay when the mean wind speed was high (14 m s^{-1}; range 4−25 m s^{-1}). The absolute value of the sea−air CO_2 flux is strongly affected by wind speed as well as the absolute value of the $\Delta pCO_{2\ sea-air}$. In this study, when the flux was −92.1 mmol C m^{-2} day^{-1}, the $\Delta pCO_{2\ sea-air}$ was not very different from its value during other periods. However, very high wind speeds (20 m s^{-1}) resulted in strong absorption in our study as well as during the study of De Jong and Dunbar (2017).

2.4.2. Seasonal Variations of $pCO_{2\ sea}$

The observations revealed no significant correlations between $pCO_{2\ sea}$ and other physical and biogeochemical components (SST, SSS, and chl *a*) (Figure 2.6). This result may reflect the short length of the sample records and interactions between multiple factors such as biological activity, temperature rise, and melting of sea ice. We then decomposed the changes of $pCO_{2\ sea}$ from winter to summer into changes attributable to biological effects, temperature, and salinity by analysis of vertical profiles of the relevant variables, which allowed us to quantify contributions from each of the factors controlling the $pCO_{2\ sea}$ by the methods in Section 2.2.4.

We estimate $pCO_{2\ sea}$ in winter by the methods of Section 2.2.4. The estimated $pCO_{2\ sea}$ in the TML of 372 ± 18 μatm indicated that the $pCO_{2\ sea}$ during the preceding winter was slightly lower than the $pCO_{2\ air}$ (389 ± 4 μatm). Figure 2.7 shows the $\delta pCO_{2\ sea}$ distributions for each effect. The negative values of the $\delta pCO_{2\ sea\_bio}$ (−92 ± 28 μatm) and $\delta pCO_{2\ sea\_sal}$ (−8 ± 4 μatm) indicated that $pCO_{2\ sea}$ was reduced by biological activity and meltwater inflow from the previous winter. The positive value of $\delta pCO_{2\ sea\_temp}$ (+38 ± 21 μatm) indicated that solar heating increased the $pCO_{2\ sea}$ during the summer. The fact that the absolute values of $\delta pCO_{2\ sea\_bio}$ and $\delta pCO_{2\ sea\_temp}$ were larger than that of $\delta pCO_{2\ sea\_sal}$ at most stations suggested that biological and temperature effects exceeded the effect of salinity on the change of $pCO_{2\ sea}$ prior to the summer. The large values of $\delta pCO_{2\ sea\_others}$ (~101 μatm) at some stations (Figure 2.7d) indicated the potential importance of other process (e.g., advection/diffusion of water masses).

We then evaluated the change of pCO_2 due to CO_2 absorption from the atmosphere. The CO_2 flux was determined from the pCO_2, but changes of pCO_2 also occurred because of CO_2 exchange

between the ocean and atmosphere. CO_2 exchange between the ocean and the atmosphere occurs until the oceanic CO_2 equilibrates with the atmospheric CO_2. The net CO_2 flux is zero when the winter $pCO_{2\ sea}$ rises from 372 μatm to the atmospheric pCO_2 of 388 μatm. In reality, there may be periods when the pCO_2 decreases below 372 μatm by biological activity. However, when the two points in winter and at the time of observation are compared, the maximum increase of pCO_2 was 16 μatm. Because this value is smaller than the absolute value of the amount of change of pCO_2 due to biological and water temperature effects, the effect of CO_2 absorption from the atmosphere is smaller than the effects of biological activity and changes of temperature.

2.4.3 Temporal Changes of $\delta pCO_{2\ sea}$

Figure 2.8 shows time series of each $\delta pCO_{2\ sea}$. During Leg 1 (December to early January), the high variability of $\delta pCO_{2\ sea\_bio}$ (−22 to −144 μatm) corresponded to the high spatial variability in the western part of KY18 (Figure 2.7). The similarity of the variation of $\delta pCO_{2\ sea\_winter-summer}$ (based on the TML) to that of $\delta pCO_{2\ sea\_bio}$ suggested that seasonal changes of pCO_2 in the western part of KY18 were strongly influenced by biological activity. However, in the eastern part of KY18 that was surveyed during Leg 2 (end of January to February), the large fluctuations of $\delta pCO_{2\ sea\_temp}$ and their similarity to $\delta pCO_{2\ winter-summer}$ suggested that there was a strong influence from the increase of SST in the eastern part of KY18. To investigate the relationship between each effect and $\delta pCO_{2\ winter-summer}$, we examined the correlations between $\delta pCO_{2\ winter-summer}$ and the controlling factors ($\delta pCO_{2\ sea\_bio}$, $\delta pCO_{2\ sea\_temp}$, $\delta pCO_{2\ sea\_sal}$, and $\delta pCO_{2\ sea\_others}$) during each leg (Figure 2.9). The results showed that $\delta pCO_{2\ winter-summer}$ was significantly correlated with $\delta pCO_{2\ sea\_bio}$ in the western part of KY18 (Leg 1; $r^2 = 0.54$, $P < 0.01$) and with $\delta pCO_{2\ sea\_temp}$ in the eastern part of KY18 (Leg 2; $r^2 = 0.37$, $P < 0.01$). The correlation with $pCO_{2\ sea\_sal}$ was also found to be statistically significant, but the correlation coefficients were relatively low (Leg 1: $r^2 = 0.22$, $P < 0.01$, Leg 2: $r^2 = 0.39$, $P < 0.01$). Therefore, the temporal change of $\delta pCO_{2\ sea\_winter-summer}$ was similar to $\delta pCO_{2\ sea\_bio}$ and $\delta pCO_{2\ sea\_temp}$ (Figure 2.8). Overall, biological activity in the western part of KY18 (Leg 1) and the increase of water temperature in the eastern part of KY18 (Leg 2) were the dominant factors controlling the $pCO_{2\ sea}$ during the seasons preceding the observations. Shim et al. (2006) showed a decrease of pCO_2 due to biological uptake in December. In addition, Nomura et al. (2014) insisted that pCO_2 is highly correlated with sea surface temperature in January. Our results agreed with these studies.

The spatiotemporal variability of $\delta pCO_{2\ sea\_bio}$ was expected to depend on the timing of the phytoplankton bloom. The bloom at 66˚S occurred between December and January (Figure 2.5b, c), whereas the bloom at 64˚S occurred between January and February (Figure 2.5c, d). This difference in timing indicated that in the western part of KY18 (Leg 1), where the bloom was observed in December and early January, biological activity was not yet active in some locations near the ice edge, and this gradient of biological activity led to the meridional difference of biological effects. However, in the eastern part of KY18 (Leg 2), where the bloom was observed from the end of January to February, the bloom was underway or already finished over the entire region during our survey of a relatively small area. Most of the differences of $\delta pCO_{2\ sea\_bio}$ were thus attributable to seasonality rather than spatial differences. The variations of $\delta pCO_{2\ sea\_temp}$ were directly influenced by SST (Figure 2.2a). The eastern part of Leg 2 ranged widely in the meridional direction, and the temperature increase toward the north very much reflected the presence of sea ice in the south (Figures 2.3a, 2.4). We therefore attribute the variability of $\delta pCO_{2\ sea\_temp}$ to the influences of both regional (sea ice distribution and ocean circulation) and seasonal (e.g., solar heating) effects.

2.4.4 Evaluation of the Validity of the $\delta pCO_{2\ sea}$ Estimates

Figures 2.7 and 2.8 indicate that there are several sites where $\delta pCO_{2\ sea\_others}$ was relatively large (>80 µatm). These large values could not be explained solely by gas exchange with the atmosphere, as discussed in Section 2.4.2; they may also be due to advection/diffusion of water masses and measurement errors. In the results shown in Figures 2.7 and 2.8, the $pCO_{2\ sea}$ values were averaged over all the values extracted in the TML because of the paucity of $pCO_{2\ sea}$ values in the water column. We then recalculated each $\delta pCO_{2\ sea}$ using the TML data from the nearest station where there was a vertical profile of $pCO_{2\ sea}$ values (recal_$\delta pCO_{2\ sea}$; Figure 2.10). The results show that recal_$\delta pCO_{2\ sea_bio}$ (which reflected the spatial distribution of nutrient concentrations) and recal_$\delta pCO_{2\ sea_others}$ changed markedly from the original $\delta pCO_{2\ sea}$ by −18 ± 20 µatm and +7 ± 23 µatm, respectively (recal_$\delta pCO_{2\ sea_bio}$: −109 ± 30 µatm, recal_$\delta pCO_{2\ sea_others}$: +27 ± 28 µatm). It was because $\delta pCO_{2\ sea\_bio}$ was calculated by using the nitrate concentration in TML, and $\delta pCO_{2\ sea\_others}$ were the residual of other three $\delta pCO_{2\ sea}$. In contrast, there was no significant change in the relative spatial distribution of $pCO_{2\ sea}$ values.

2.4.5 Decadal Trend

The same oceanographic observations were made in KY18 during BROKE (30 January−26 March 1996) by the R/V Aurora-Australis. We collected CO_2 concentrations in the sea ($xCO_{2\ sea}$) during BROKE from the Surface Ocean CO_2 Atlas (SOCAT) (Bakker et al, 2016; accessible at https://www.socat.info/) to compare with our 2018/2019 measurements. Because the equilibrium atmospheric pressures used to calculate pCO_2 in BROKE and in this study differed, $xCO_{2\ sea}$ was used instead of pCO_2 in the following calculations. For seasonal and spatial consistency, the comparison was limited to east of 120˚E and south of 63˚S (Figure 2.11).

In 1996, the mean $xCO_{2\ sea}$ was 334 ± 23 ppm, and the mean $xCO_{2\ air}$ was 359 ± 0 ppm. In contrast, the mean $xCO_{2\ sea}$ during 2019 was 357 ± 25 ppm, and the mean $xCO_{2\ air}$ was 404 ± 0 ppm; thus, there had been an increase of xCO_2 over the past 23 years for both $xCO_{2\ sea}$ and $xCO_{2\ air}$ ($xCO_{2\ sea}$ is shown in Figure 2.12). The increase of the $xCO_{2\ sea}$ was especially pronounced in coastal areas (Figure 2.11). This pattern may have been a consequence of the simultaneous occurrence of seasonal events in the coastal area, such as the dominance of increasing SST over the effect of freshwater inflows and primary production (e.g., Nomura et al., 2014). In contrast, the $xCO_{2\ sea}$ was significantly reduced at the southern end of 150˚E (Figure 2.12). This reduction may have been due to the influence of iceberg B09B, which caused the collapse of the Merz Glacier Tongue in 2012 (Shadwick et al., 2013). The movement of B09B may have increased irradiance and thus biological activity.

Figure 2.13 shows the vertical distribution of nitrate to a depth of 400 m along several meridians. Nitrate data during BROKE were obtained from GLODAP v2. 2020 (Olsen et al., 2020; accessible at https://www.glodap.info/). During the summer, biological activity in the surface layer typically results in low nutrient concentrations and a marked difference in nutrient concentrations between the TML and the surface layer (Figure 2.13). However, along the 150˚E meridian in 1996 (Figure 2.13e), the nitrate concentrations in the surface layer south of 65.5˚S were uniform; there was no difference between the concentrations in the TML and the surface layer. This uniformity suggests that there was little biological activity in 1996. This low level of biological production may have been due to the poor light environment caused by the stranding of iceberg B09B. However, the differences in nutrient concentrations between the TML and the surface layer in 2019, even south of 65.5˚S (Figure 2.13f), suggested that biological activity was high. This difference in biological production may have resulted in the lower xCO_2 in this region during 2019 than during 1996. Over

the past 23 years, the mean $xCO_{2\ sea}$ and $xCO_{2\ air}$ have increased by 23 ppm and 45 ppm, respectively. This pattern indicates that the increase of the atmospheric CO_2 concentration has exceeded the increase of the CO_2 concentration at the ocean surface. This pattern suggests that the effect of preventing $xCO_{2\ sea}$ from equilibrating with the elevated $xCO_{2\ air}$ associated with changes, for example, in water-mass distribution may have affected the $xCO_{2\ sea}$.

One of the factors that may cause variations of $xCO_{2\ sea}$ is the spatial distribution of front positions. The discovery by Yamazaki et al. (2021) that the Southern Boundary (SB) of Antarctic Circumpolar Current (ACC) moved southward during the period between BROKE and this study indicates that the upwelling region of Circumpolar Deep Water (CDW) moved southward. As a result, the maximum concentration of nitrate near the TML increased, and the difference of nitrate concentrations between the ocean surface and the TML increased (Figure 2.13). In other words, ocean surface nitrate concentrations during the winter were higher at KY18 than at BROKE, and more nitrate was consumed by biological production during the summer. More active biological production during the spring may have accelerated the decrease of $xCO_{2\ sea}$. To elucidate the relationship between the distribution of $xCO_{2\ sea}$ and the front, we plotted the relationship between the distributions of $xCO_{2\ sea}$ and the front during BROKE and the present study in Figure 2.14, where the Southern Antarctic Circumpolar Current Front (SACCF) = 1, SB = 0, and the Antarctic Slope Front (ASF) = −1 on the ordinate, and the spatial relationship between plots and the fronts was quantified based on these approximations (normalized latitude). The xCO_2 increase was calculated by adding the estimated increase in atmospheric xCO_2 and the effect of the increase of water temperature to the $xCO_{2\ sea}$ at the time of BROKE. The following changes were then made to Figure 2.14: atmospheric $xCO_{2\ sea}$ increase = 45 ppm and $xCO_{2\ sea}$ increase due to water temperature increase (about 1.5˚C) = +6% (4% $^{\circ}C^{-1}$). In the area between the SACCF and SB, the observed changes tended to be lower than the estimated increase of $xCO_{2\ sea}$. In the coastal areas south of the ASF, the trend was different at each longitude. This pattern suggests that the influence of biological activity on the $xCO_{2\ sea}$ in the region between the SACCF and SB was significant and that the regional characteristics of sea ice and biological production in coastal areas south of the ASF further modified the $xCO_{2\ sea}$.

The vertical distributions of nitrate shown earlier (Figure 2.13) indicated that ΔNO_3^- was about 7 μmol kg^{-1} at BROKE and about 10 μmol kg^{-1} at the time of this study. This difference was converted to a change in DIC/TA by the method described in Section 2.4.2 and added to the winter nitrate value. For BROKE, there were no DIC/TA data available. We assumed that anthropogenic

effects caused no secular trend in TA, we used the TA of the TML in this study (2340 μmol kg^{-1}) as the TA in 1996. However, the DIC may certainly have increased by the influx of anthropogenic CO_2. We therefore used the increase in anthropogenic carbon dioxide between 1995 and 2012 calculated by Murata et al. (2019) to reproduce the DIC in 1996. According to Murata et al. (2019), anthropogenic carbon dioxide in the mixed layer at 130−160˚E changed by +8.4 ± 1.4 μmol kg^{-1}. Subtraction of this increase from the mean DIC of the TML in this study resulted in a calculated DIC of about 2218 μmol kg^{-1} in 1996. This DIC was used to calculate the $xCO_{2\ sea}$ in the ocean surface layer in winter, and the change of $xCO_{2\ sea}$ due to biological activity was calculated from changes of nutrient concentrations. This calculation made use of atmospheric pressure and temperature data recorded at Syowa Station of the Japan Meteorological Agency (https://www.jma.go.jp/jma/index.html). The results indicated that the decrease of $xCO_{2\ sea}$ by biological production from winter to summer was 115 ppm in 1996 and 163 ppm in 2019. The implication is that 48 ppm of the difference in $xCO_{2\ sea}$ between 1996 and 2019 was due to differences in biological production caused by changes in the water-mass distribution. This estimate is close to the difference between the $xCO_{2\ sea}$ increase and $xCO_{2\ sea}$ north of the SB at the time of this study (Figure 2.14). This result indicates that the secular change in $xCO_{2\ sea}$ was influenced not only by the absorption of CO_2 from the atmosphere, but also by the increase in biological activity associated with the change in the water-mass distribution related to the change in the front positions.

2.5. Conclusion

This study was an assessment of the carbon cycle in the East Indian Ocean sector of the Southern Ocean. During the observation period (December 2018–February 2019), the sea−air CO_2 flux in KY18 was −8.2 ± 12.5 mmol C m^{-2} day^{-1}, and KY18 was thus a weak carbon sink. A quantitative assessment of the drivers of $pCO_{2\ sea}$ variability, based on estimates of winter–summer seasonal changes of $pCO_{2\ sea}$, revealed that biological activity in the western part of KY18 from December to early January and changes of water temperature in the eastern part of KY18 from the end of January to February influenced the spatial distribution of $pCO_{2\ sea}$.

The $\delta pCO_{2\ sea}$ estimation based on the analysis conducted in this study therefore helped to explain the spatial distribution of the sources of variability. More detailed measurements of the components of the carbonate system at each point would enable more accurate estimates. Furthermore, the

$\delta pCO_{2\ sea\_others}$ likely included errors in the calculations and estimates. In the present calculations, when the salinity was normalized to 34.25, it was assumed that sea ice meltwater and ice sheet meltwater contained no carbonate system components. In reality, however, they do contain carbonate system components, although the concentrations are very low compared to seawater (Meire et al., 2015). Our assumption may have led to an underestimation of nDIC and nTA and therefore have led to errors in the $\delta pCO_{2\ sea}$ estimates. For a more accurate assessment, multiple sea ice and iceberg samples should therefore be collected at the observation times, and the endmembers should be changed for each region and period.

In addition, the mean $xCO_{2\ sea}$ and $xCO_{2\ air}$ increased by 23 ppm and 45 ppm, respectively, compared to the values during the 1996 BROKE survey. These results suggest that in addition to equilibrium with elevated atmospheric CO_2 concentrations, changes in the distribution of nutrient concentrations due to changes in water mass distribution, such as the southward movement of the SB, may have influenced changes over time.

Acknowledgments

We sincerely thank the crews and scientists onboard the R/V *Kaiyo-Maru* for their dedication to the fieldwork. The survey was supported by the Institute of Cetacean Research, Japan Fisheries Research and Education Agency, Fisheries Agency of Japan and the Joint Research Program of the Institute of Low Temperature Science, Hokkaido University. We also thank Prof. Atsushi Ooki for his useful advice and comments on this paper. This work was supported by grants from the Japan Society for the Promotion of Science (18H04131, 17H04715, 15H05116).

Data Availability Statement

This chapter is a modified version of Tozawa et al. (2022). Data used in the study and supporting information are available from Tozawa et al. (2022). These data and pCO_2 data were archived in the data repository of the National Institute of Polar Research, Tokyo, Japan (https://doi.org/10.17592/001.2021120701, https://doi.org/10.17592/001.2021120702).

References

Arroyo, M. C., Shadwick, E. H., Tilbrook, B. (2019). Summer carbonate chemistry in the Dalton Polynya, East Antarctica, *Journal of Geophysical Research: Oceans*, 124, 5634–5653. https://doi.org/10.1029/2018JC014882

Auger, M., Morrow, R., Kestenare, E., Sallée, J., Cowley, R. (2021). Southern Ocean in-situ temperature trends over 25 years emerge from interannual variability, *Nature Communications*, 12, 514. https://doi.org/10.1038/s41467-020-20781-1

Bakker, D. C. E., Pfeil, B., Landa, C., Metzl, N., O'Brien, K., Olsen, A., et al. (2016). A multi-decade record of high-quality *f*CO_2 data in version 3 of the Surface Ocean CO_2 Atlas (SOCAT), *Earth System Science Data*, 8(2), 383–413. https://doi.org/10.5194/essd-8-383-2016

Bates, N. R., Garley, R., Frey, K. E., Shake, K. L., Mathis, J. T. (2014). Sea-ice melt CO_2–carbonate chemistry in the western Arctic Ocean: meltwater contributions to air–sea CO_2 gas exchange, mixed-layer properties and rates of net community production under sea ice, *Biogeosciences,* 11(23), 6769–6789. https://doi.org/10.5194/bg-11-6769-2014

Bindoff, N., Rosenberg, M., Warner, M. (2000). On the circulation and water masses over the Antarctic continental slope and rise between 80 and 150˚E, *Deep-Sea Research II,* 47 (12–13), 2299-2326. DOI:10.1016/S0967-0645(00)00038-2

Deppeler, S. L. and Davidson, A. T. (2017). Southern Ocean Phytoplankton in a Changing Climate, *Frontiers in Marine Science*. https://doi.org/10.3389/fmars.2017.00040

DeJong, H. B., and Dunbar, R. B. (2017). Air–sea CO_2 exchange in the Ross Sea, Antarctica, *Journal of Geophysical Research: Oceans,* 122, 8167–8181. https://doi.org/10.1002/2017JC012853

Dickson, A. G. and Millero, F. J. (1987). A comparison of the equilibrium constants for the dissociation of carbonic acid in seawater media, *Deep−Sea Research*, 34, 1733–1743

Dickson, A. G., Sabine, C. L., Christian, J. R. (2007). Guide to best practices for ocean CO_2 measurement*, PICES Special Publication 3*, 191

Dickson, A. G. (1990). Thermodynamics of the dissociation of boric acid in synthetic seawater from 273.15 to 318.15 K, *Deep−Sea Research Part A, Oceanographic Research Papers*, 37, 755–766

Fransson, A., Chierici, M., Nojiri, Y. (2006). Increased net CO_2 outgassing in the upwelling region of the southern Bering Sea in a period of variable marine climate between 1995 and 2001, *Journal of Geophysical Research Ocean*, 111, C08008. https://doi.org/doi:10.1029/2004JC002759

Friedlingstein, P., Jones, M. W., O'Sullivan, M., Andrew,R. M., Bakker, D. C. E., Hauck, J., et al. (2021). Global Carbon Budget 2021, *Earth System Science Data*, 14, 1917–2005. https://doi.org/10.5194/essd-2021-386, in review.

González-Dávila, M., Santana-Casiano, J. M., Rueda, M. J., Llinás, O. (2010) The water column distribution of carbonate system variables at the ESTOC site from 1995 to 2004, Biogeosciences, 7, 3067–3081, https://doi.org/10.5194/bg-7-3067-2010

JGOFS (1994). *Protocols for the Joint Global Ocean Flux Study core measurements*. *International JGOFS Report Series,* vol19, Bergen, Norway: JGOFS International Project Office.

Knap, A., A. Michaels, A. Close, H. Ducklow., A. Dickson. (1996). Protocols for the Joint Global Ocean Flux Study (JGOFS) Core Measurements,*JGOFS Report Nr. 19, vi+170 pp. Reprint of the IOC Manuals and Guides No. 29, UNESCO 1994.*

Johnson, K. M., King, A. E., Sieburth, J. M. (1985). Coulometric TCO_2 analyses for marine studies: An introduction, *Marine Chemistry*, 16, 61–82.

Johnson, K.M. (1992). Operator's Manual: Single−Operator Multiparameter Metabolic Analyzer (SOMMA) for Total Carbon Dioxide (CT) with Coulometric Detection, *Brookhaven National Laboratory*.

Kiuchi, M., Nomura, D., Hirano, D., Tamura, T., Hashida, G., Ushio, S., et al. (2021). The effect of basal melting of the Shirase Glacier Tongue on the CO_2 system in Lützow−Holm Bay, East Antarctica. *Journal of Geophysical Research: Biogeosciences*, 126,

e2020JG005762. https://doi.org/10.1029/2020JG005762

Legge, O. J., Bakker, D. C., Meredith, M. P., Venables, H. J., Brown, P. J., Jones, E. M., Johnson, M. T. (2017). The seasonal cycle of carbonate system processes in Ryder Bay, West Antarctic Peninsula. *Deep Sea Research Part II: Topical Studies in Oceanography*, 139, 167–180. https://doi.org/10.1016/j.dsr2.2016.11.006

Mehrbach, C., Culberson, C.H., Hawley, J. E., Pytkowicz, R. M. (1973). Measurement of the apparent dissociation constants of carbonic acid in seawater at atmospheric pressure, *Limnology and Oceanography*, 18, 897–907. https://doi.org/10.4319/lo.1973.18.6.0897

Meire, L., Søgaard, D. H., Mortensen, J., Meysman, F. J. R., Soetaert, K., Arendt, K. E., et al. (2015). Glacial meltwater and primary production are drivers of strong CO_2 uptake in fjord and coastal waters adjacent to the Greenland Ice Sheet, *Biogeosciences*, 12, 2347–2363. https://doi.org/10.5194/bg−12−2347−2015

Murata, A., Kumamoto, Y., Sasaki, K. (2019). Decadal-Scale Increases of Anthropogenic CO_2 in Antarctic Bottom Water in the Indian and Western Pacific Sectors of the Southern Ocean, *Geophysical Research Letters,* 46, 833–841. https://doi.org/10.1029/2018GL080604

Nakaoka, S., Nakazawa, T., Yoshikawa−Inoue, H., Aoki, S., Hashida, G., et al. (2009). Variations of oceanic pCO_2 and air−sea CO_2 flux in the eastern Indian sector of the Southern Ocean for the austral summer of 2001–2002, *Geophysical Research Letters*, 36, L14610. doi:10.1029/2009GL038467

Nicol, S., T. Pauly, N. L. Bindoff, P. G. Strutton (2000). “BROKE” a biological/oceanographic survey off the coast of East Antarctica (80–150˚E) carried out in January–March 1996, *Deep Sea Research II*, 47(12–13), 2281-2297. http://dx.doi.org/10.1016/S0967-0645(00)00026-6

Nicol, S., K. Meiners, & B. Raymond (2010). BROKE-West, a large ecosystem survey of the South West Indian Ocean sector of the Southern Ocean, 30˚E-80˚E (CCAMLR Division 58.4.2), *Deep Sea Research II*, 57(9-10), 693-700.

Nomura, D., Yoshikawa−Inoue, H., Kobayashi, S., Nakaoka, S., Nakata, K., Hashida, G. (2014).

Winter−to−summer evolution of pCO_2 in surface water and air–sea CO_2 flux in the seasonal ice zone of the Southern Ocean, *Biogeosciences*, 11, 5749– 5761. https://doi.org/10.5194/bg−11−5749−2014

Olsen, A., Lange, N., Key, R., Tanhua, T., Bittig, H., Kozyr, A., et al. (2020). An updated version of the global interior ocean biogeochemical data product, GLODAPv2.2020, *Earth System Science Data*, 12, 3653–3678. https://doi.org/10.5194/essd-12-3653-2020

Ono, T., Watanabe, S., Okuda, K., Fukasawa, M. (1998). Distribution of total carbonate and related properties in the North Pacific along 30˚N, *Journal of Geophysical. Research: Ocean*, 103(C13), 30873– 30883. doi:10.1029/1998JC900018

Orr, J. C., Epitalon, J. M., Dickson, A. G., Gattuso, J. P. (2018). Routine uncertainty propagation for the marine carbon dioxide system. *Marine Chemistry, 207*, 84–107.

Parsons, T. R., Takahashi, M., Hargrave. B. (1984). Biological Oceanographic Processes 3rd Edition, *Pergamon*.

Pierrot, D. E., Lewis, E., D. W. R. Wallace. (2006). MS Excel Program Developed for CO_2 System Calculations. ORNL/CDIAC−105a. Carbon Dioxide Information Analysis Center, Oak Ridge National Laboratory, U.S. Department of Energy, Oak Ridge, Tennessee. doi: 10.3334/CDIAC/otg.CO2SYS_XLS_CDIAC105a

Pondaven, P., Ragueneau, O., Tréguer, P., Hauvespre, A., Dezileau, L., Reyss, J. L. (2000). Resolving the “opal paradox” in the Southern Ocean, *Nature*, 405, 168–172.

Roden, N. P., Tilbrook, B., Trull, T. W., Virtue, P., Williams, G. D. (2016). Carbon cycling dynamics in the seasonal sea−ice zone of East Antarctica. *Journal of Geophysical Research: Oceans*, 121, 8749–8769.

Sabine, C. L., Feely, R. A., Gruber, N., Key, R. M., Lee, K., Bullister, J. L., et al. (2004). The oceanic sink for anthropogenic CO_2. *Science,* 305, 367–371. https://doi.org/10.1126/science.1097403

Sallée, J.B. (2018). Southern Ocean warming. *Oceanography*, 31(2):52–62. https://doi.org/10.5670/oceanog.2018.215

Schlitzer, R. (2020). Ocean Data View. http://odv.awi.de

Shadwick, E. H., S. R. Rintoul, B. Tilbrook, G. D. Williams, N. Young, A. D. Fraser, H., et al. (2013 a), Glacier tongue calving reduced dense water formation and enhanced carbon uptake, *Geophysical Research Letters*, 40, 904–909. doi:10.1002/grl.50178

Shadwick, E. H., Tilbrook, B., Currie, K. I. (2017). Late−summer biogeochemistry in the Mertz Polynya: East Antarctica, *Journal of Geophysical Research: Oceans,* 122, 7380–7394. https://doi.org/10.1002/2017JC013015

Shadwick, E. H., Tilbrook, B., Currie, K. I. (2017). Late−summer biogeochemistry in the Mertz Polynya: East Antarctica, *Journal of Geophysical Research: Oceans,* 122, 7380–7394. https://doi.org/10.1002/2017JC013015

Shim, J, Kang, Y. C., Kim, D., Choi, S. (2006). Distribution of net community production and surface pCO_2 in the Scotia Sea, Antarctica, during austral spring 2001, *Marine Scicenes, Chemistry; Oceanography*, 101, 68–84. http://dx.doi.org/10.1016/j.marchem.2005.12.007

Suzuki, R. and Ishimaru, T. (1990). An improved method for the determination of phytoplankton chlorophyll using N, N− dimethylformamide, *Journal of the Oceanographical Society of Japan*., 46, 190–194. doi:10.1007/BF02125580

Takahashi, T., Sweeney, C., Hales, B., Chipman, D. W., Newberger, T., Goddard, J. G., et al. (2012). The changing carbon cycle in the Southern Ocean, *Oceanography*, 25, 26–37. https://doi.org/10.5670/oceanog.2012.71

Tomczak, M. and Liefrink, S. (2005). Interannual variations of water mass volumes in the Southern Ocean, *Journal of Atmospheric and Ocean Science*, 10, 31–42. DOI:10.1080/17417530500062838

Tozawa, M., Nomura, D., Nakaoka, S., Kiuchi, M., Yamazaki, K., Hirano, D., Aoki, S., Sasaki, H., Murase, H. (2022). Seasonal variations and drivers of surface ocean pCO_2 in the seasonal ice zone

of the eastern Indian sector, Southern Ocean. *Journal of Geophysical Research: Oceans*, 127, e2021JC017953. https://doi.org/10.1029/2021JC017953

Wanninkhof, R. H., Park, G. -H., Takahashi, T., Sweeney, W., Feely, R., Nojiri, Y., et al. (2013). Global ocean carbon uptake: Magnitude, variability and trends, *Biogeosciences*, 10(3), 1983–2000. doi: 10.5194/bg−10−1983−2013

Wanninkhof R. (2014). Relationship between wind speed and gas exchange over the ocean revisited, *Limnology and Oceanography: Methods*, 12 (6), pp. 351−362. https://doi.org/10.4319/lom.2014.12.351

Weiss, R. F. (1974). Carbon dioxide in water and seawater: the solubility of a non−ideal gas, *Marine Chemistry*, 2, 203–205.

Weiss, R.F. and Price, B.A. (1980). Nitrous oxide solubility in water and seawater. *Marine Chemistry*, 8(4), 347–359. https://doi.org/10.1016/0304-4203(80)90024-9

Williams, G., Nicol, S., Aoki, S., Meijers, A., Bindoff, N., Iijima, Y., et al. (2010). Surface oceanography of BROKE−West, along the Antarctic margin of the south−west Indian Ocean (30–80˚E), *Deep−Sea Research part II Topical Studies in Oceanography*, 57 (9–10), 738–757. DOI:10.1016/j.dsr2.2009.04.020

Yamazaki, K., Aoki, S., Shimada, K., Kobayashi, T., Kitade, Y. (2020). Structure of the subpolar gyre in the Australian-Antarctic Basin derived from Argo floats, *Journal of Geophysical Research: Oceans,* 125, e2019JC015406. https://doi.org/10.1029/2019JC015406

Yamazaki, K., Aoki, S., Katsumata, K., Hirano, D., Nakayama, Y. (2021). Multidecadal poleward shift of the southern boundary of the Antarctic Circumpolar Current off East Antarctica, *American Association for the Advancement of Science*, 2375-2548. https://doi.org/10.1126/sciadv.abf8755

Figures and Tables

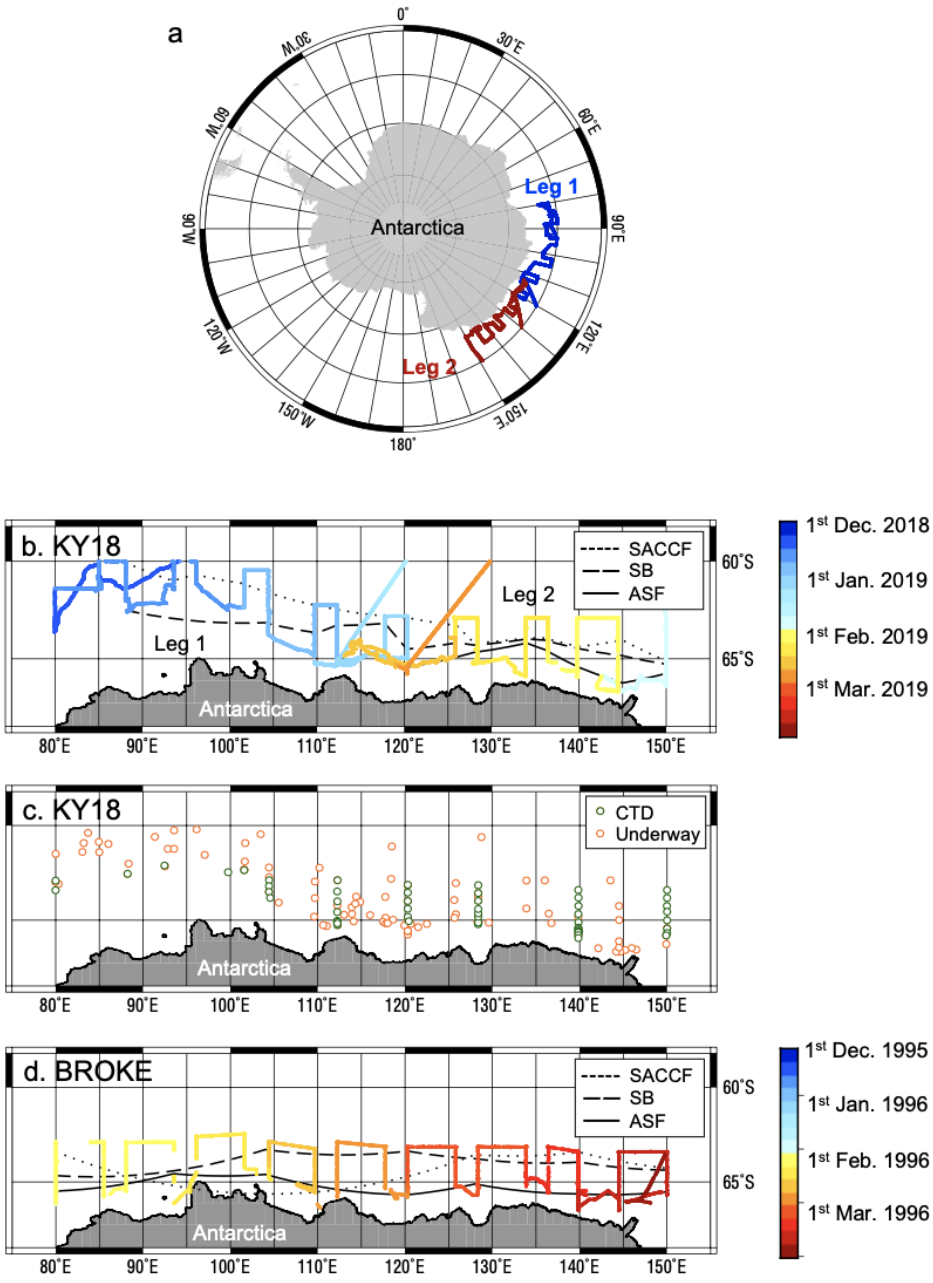

Figure 2.1. (a) Study region with cruise tracks of KY18 (Leg 1 in blue, Leg 2 in red), (b) Zoom of the study region with cruise tracks colored based on time, (c) conductivity-temperature-depth (CTD) observations and water-sampling sites (Green: CTD + vertical profiles, Orange: ocean surface water sampling), and (d) cruise track of BROKE colored based on time. SACCF: Southern Antarctic Circumpolar Current Front indicated by the dotted line. SB: Southern Boundary of ACC indicated by the dashed line. ASF: Antarctic Slope Front indicated by the solid line.

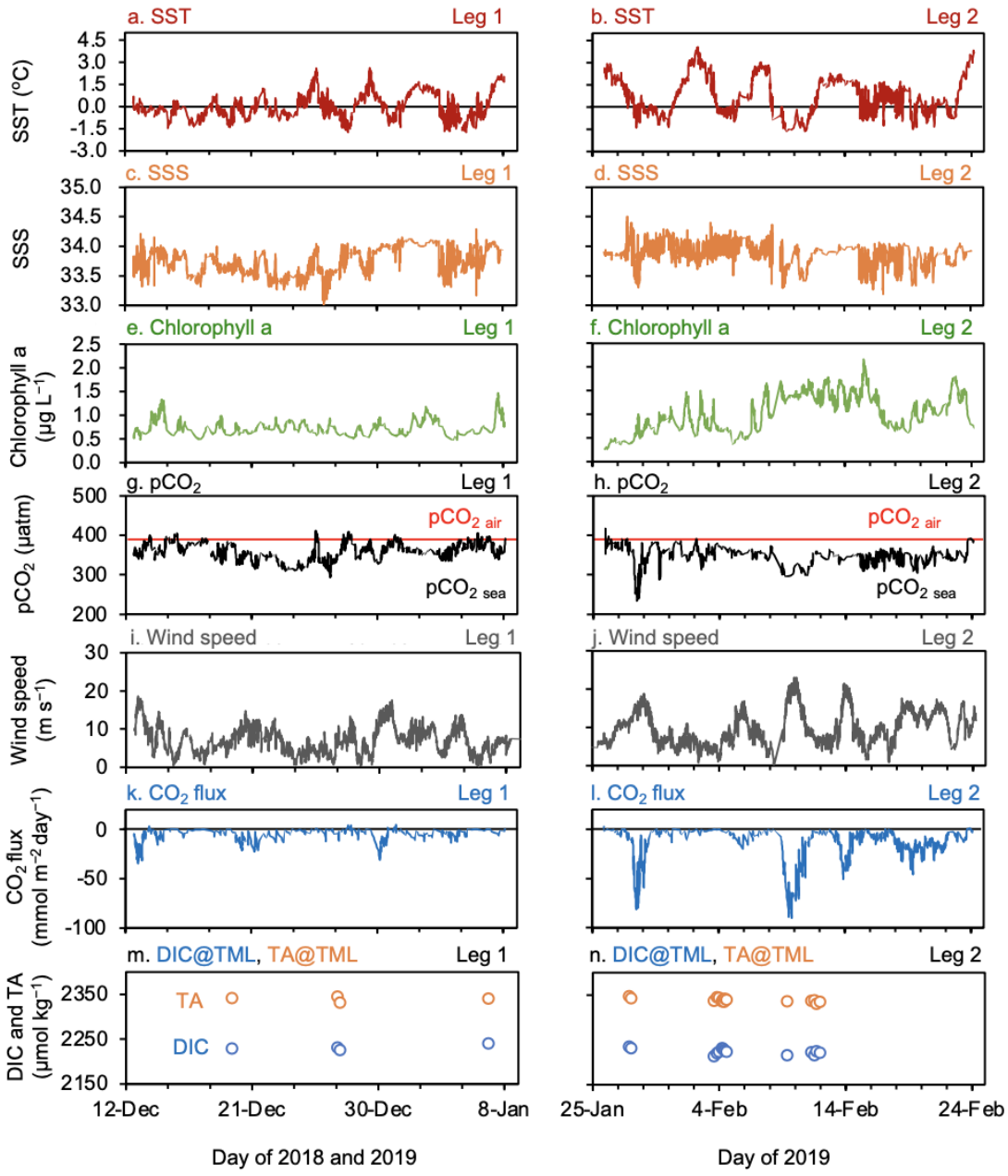

Figure 2.2. Time series of ocean surface variables for leg 1 (left column) and leg 2 (right column) of KY18: (a), (b) sea surface temperature; (c), (d) sea surface salinity; (e), (f) chl *a* concentration; (g), (h) $pCO_{2\ sea}$ and $pCO_{2\ air}$; (i), (j) wind speed; (k), (l) CO_2 flux; and (m), (n) dissolved inorganic carbon (DIC) and total alkalinity (TA) in the temperature minimum layer (TML).

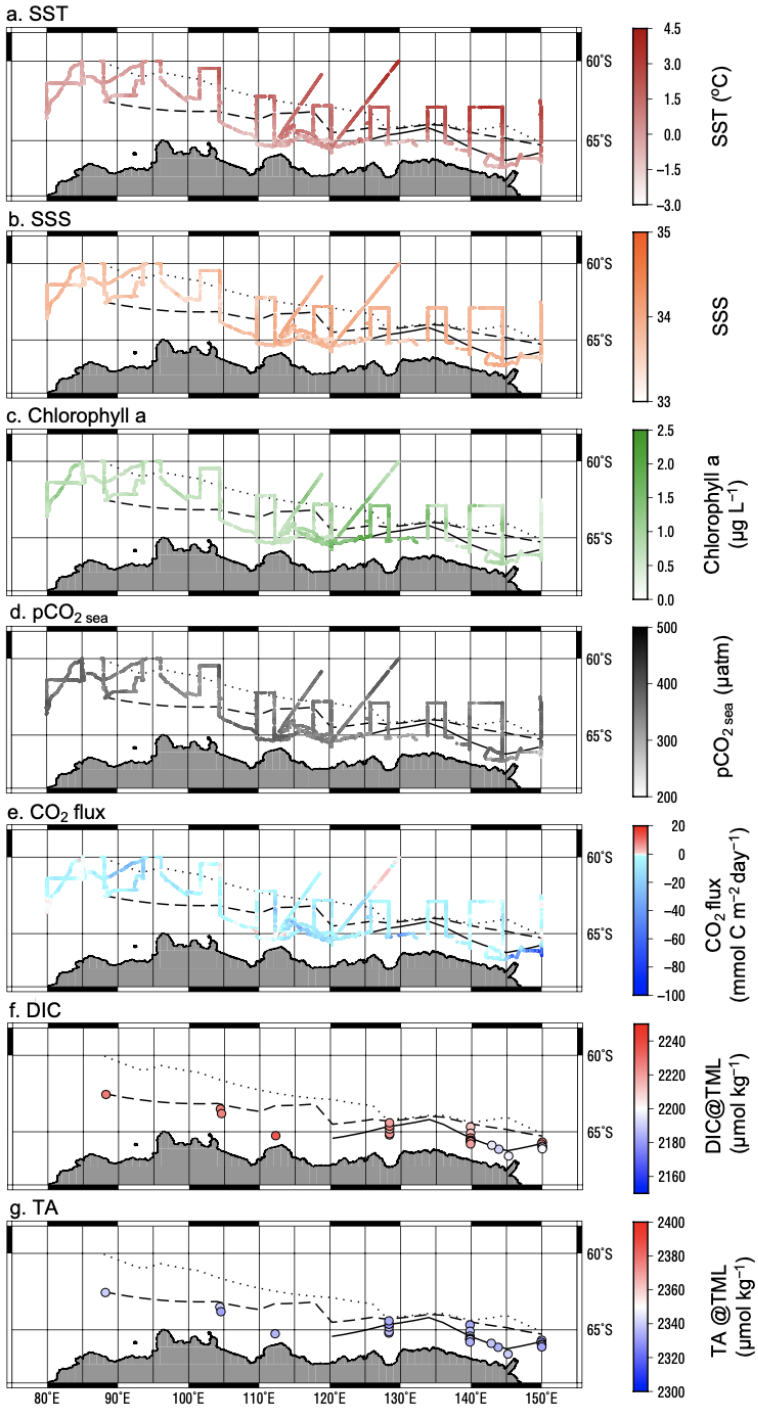

Figure 2.3. Spatial distribution of ocean surface data: (a) water temperature, (b) salinity, (c) chl *a* concentration, (d) $pCO_{2\ sea}$, (e) CO_2 flux, (f) dissolved inorganic carbon (DIC) in the TML, and (g) total alkalinity (TA) in the TML. SACCF: Southern Antarctic Circumpolar Current Front indicated by the dotted line. SB: Southern Boundary of ACC indicated by the dashed line. ASF: Antarctic Slope Front indicated by the solid line.

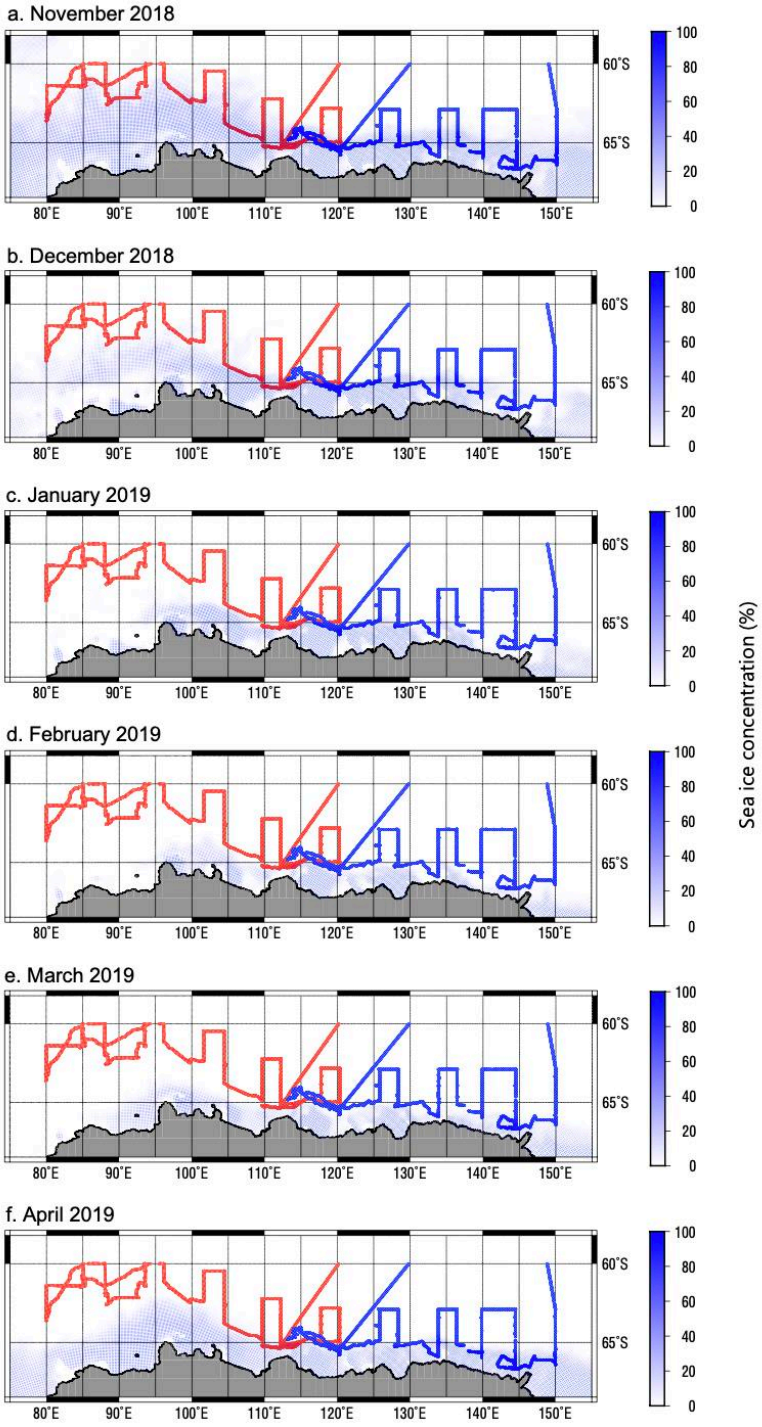

Figure 2.4. Satellite image for monthly percent cover by sea ice from the Advanced Microwave Scanning Radiometer 2: (a) November 2018, (b) December, (c) January 2019, (d) February, (e) March, and (f) April. Solid lines show cruise tracks during Leg 1 (red) and Leg 2 (blue).

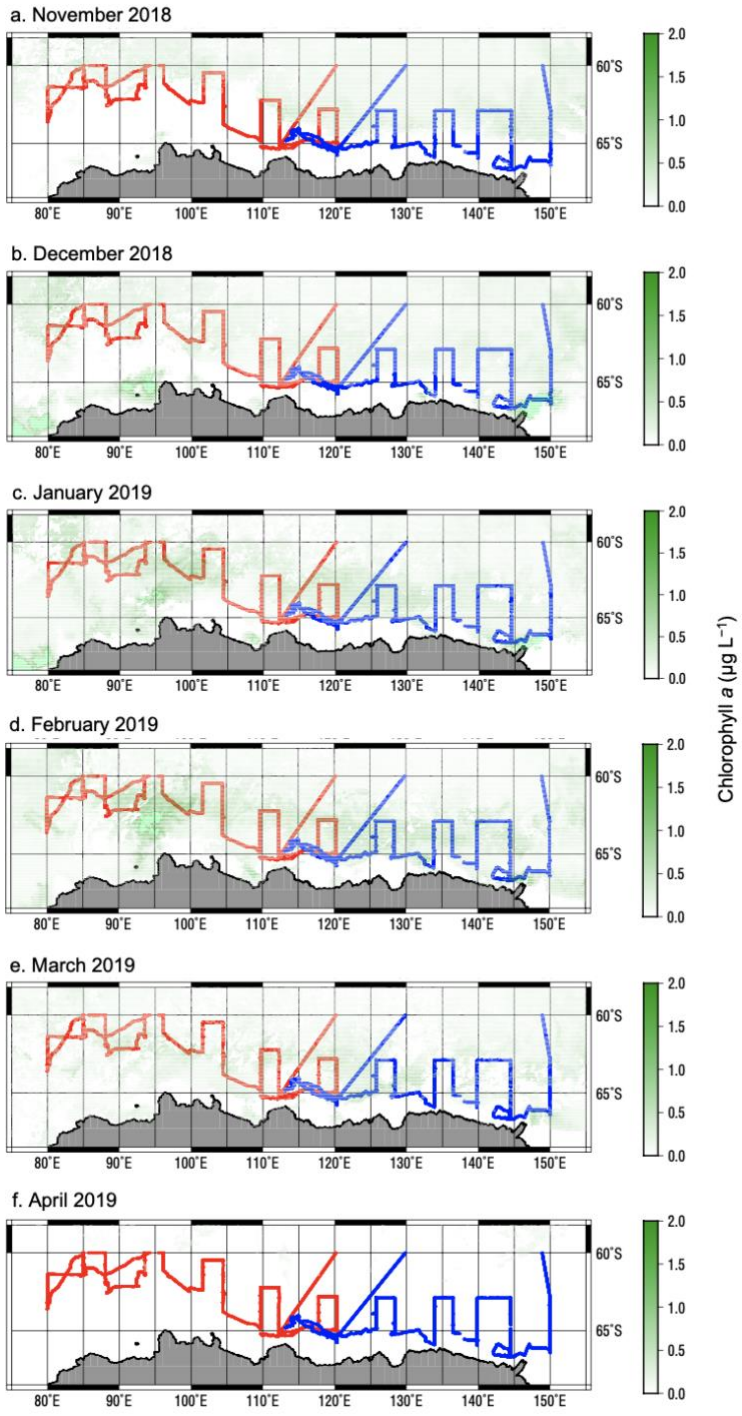

Figure 2.5. Monthly average chlorophyll *a* concentration from SeaWiFS imagery: (a) November 2018, (b) December, (c) January 2019, (d) February, (e) March, and (f) April. Solid lines show cruise tracks during Leg 1 (red) and Leg 2 (blue).

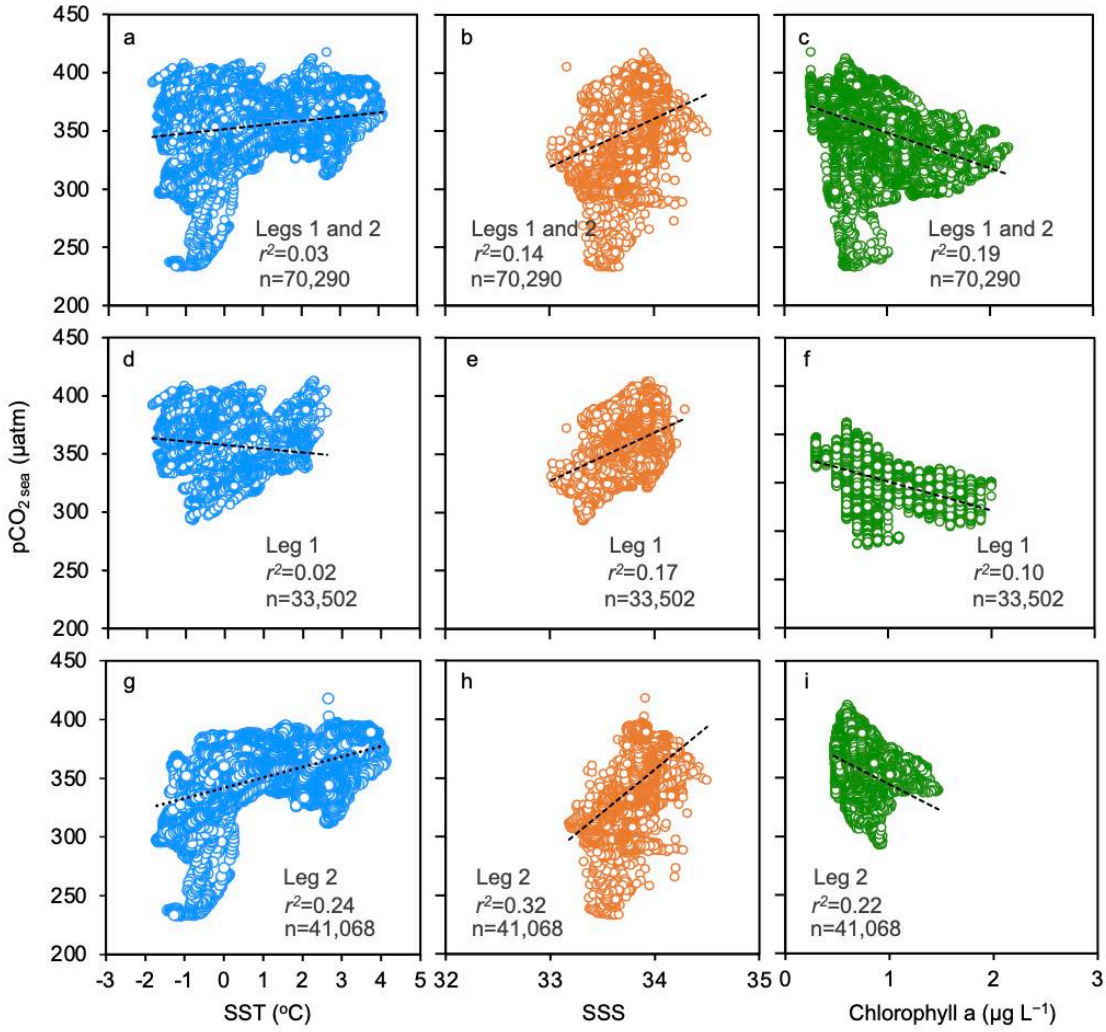

Figure 2.6. Relationship between ocean surface data and $pCO_{2\ sea}$: (a)−(c) Legs 1 and 2 ($pCO_{2\ sea}$ vs water temperature, $pCO_{2\ sea}$ vs salinity, $pCO_{2\ sea}$ vs chl *a* concentration), (d)−(f) Leg 1 ($pCO_{2\ sea}$ vs water temperature, $pCO_{2\ sea}$ vs salinity, $pCO_{2\ sea}$ vs chl *a* concentration), and (g)−(i) Leg 2 ($pCO_{2\ sea}$ vs water temperature, $pCO_{2\ sea}$ vs salinity, $pCO_{2\ sea}$ vs chl *a* concentration). The dash lines are regression lines.

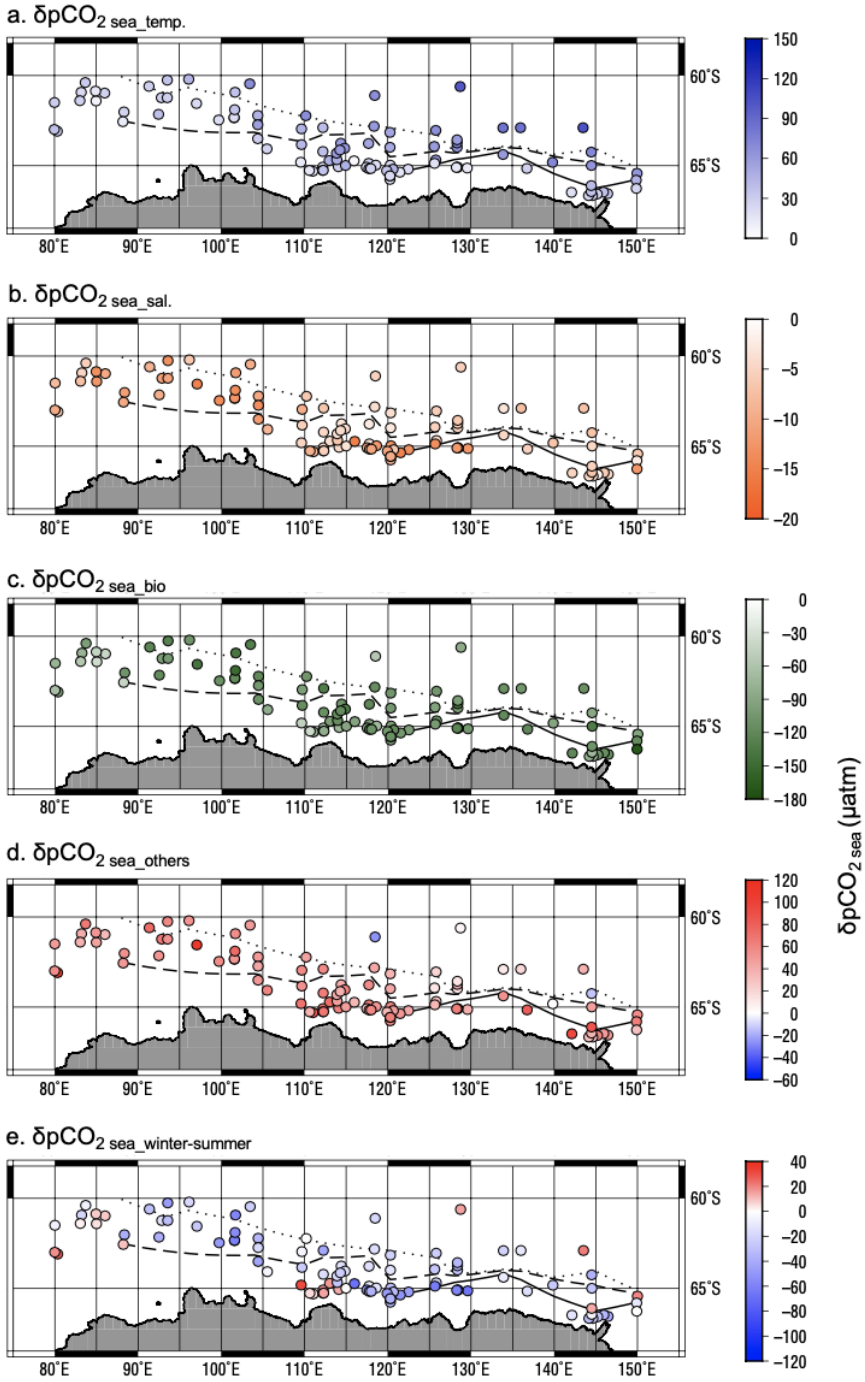

Figure 2.7. Spatial distribution for $\delta pCO_{2\ sea}$ due to (a) temperature ($\delta pCO_{2\ sea\_temp}$), (b) salinity ($\delta pCO_{2\ sea\_sal}$), (c) biological activity ($\delta pCO_{2\ sea\_bio}$), (d) other factors ($\delta pCO_{2\ sea\_others}$), and (e) measured $\delta pCO_{2\ sea}$ ($\delta pCO_{2\ sea\_winter-summer}$). SACCF: Southern Antarctic Circumpolar Current Front indicated by the dotted line. SB: Southern Boundary of ACC indicated by the dashed line. ASF: Antarctic Slope Front indicated by the solid line.

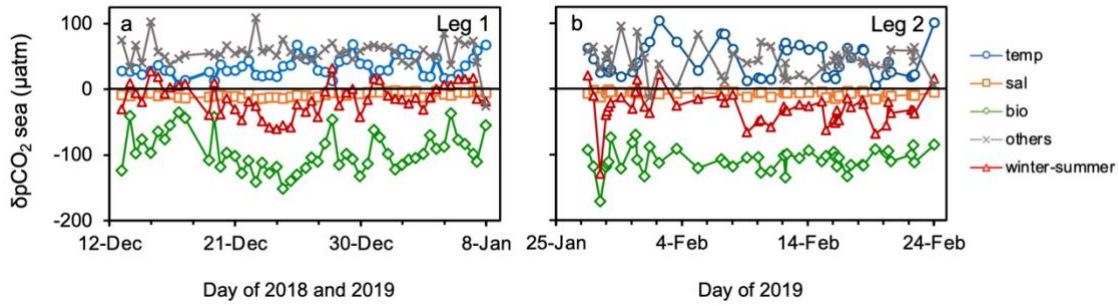

Figure 2.8. Temporal variations of $\delta pCO_{2\ sea\_winter\text{-}summer}$ (red triangles) during Leg 1 (a) and Leg 2 (b) due to temperature (blue circles), salinity (orange squares), biological activity (green diamonds), and other factors (grey crosses).

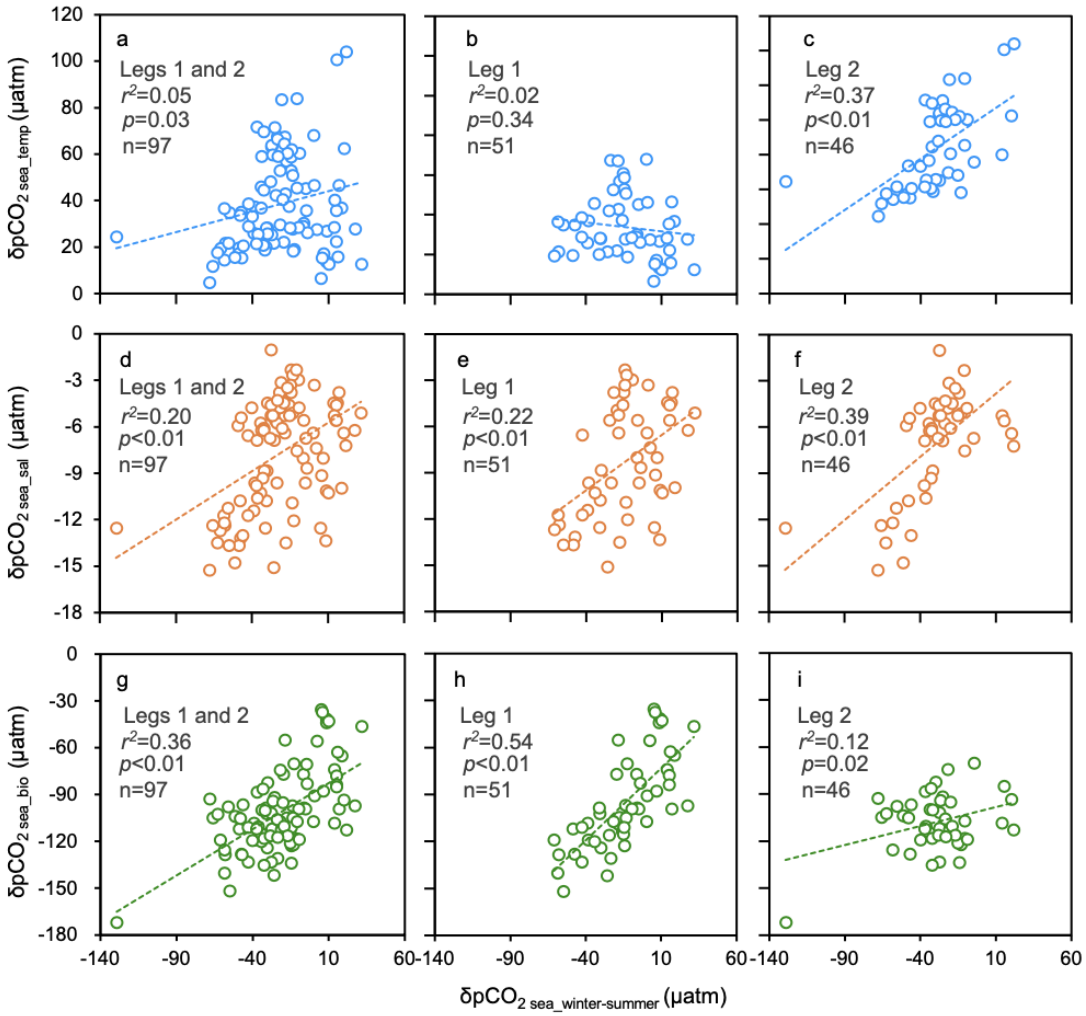

Figure 2.9. Relationship between the measured $\delta pCO_{2\ sea}$ ($\delta pCO_{2\ sea\_winter\text{-}summer}$) and (a)−(c) $\delta pCO_{2\ sea\_temp}$, (d)−(f) $\delta pCO_{2\ sea\_sal}$, and (g)−(i) $\delta pCO_{2\ sea\_bio}$ for Legs 1, 2, and both legs. Legs 1 and 2, (left column), Leg 1 (central column), and Leg 2 (right column). Subscripts have same meanings as in Figure 2.7. The dash lines are regression line.

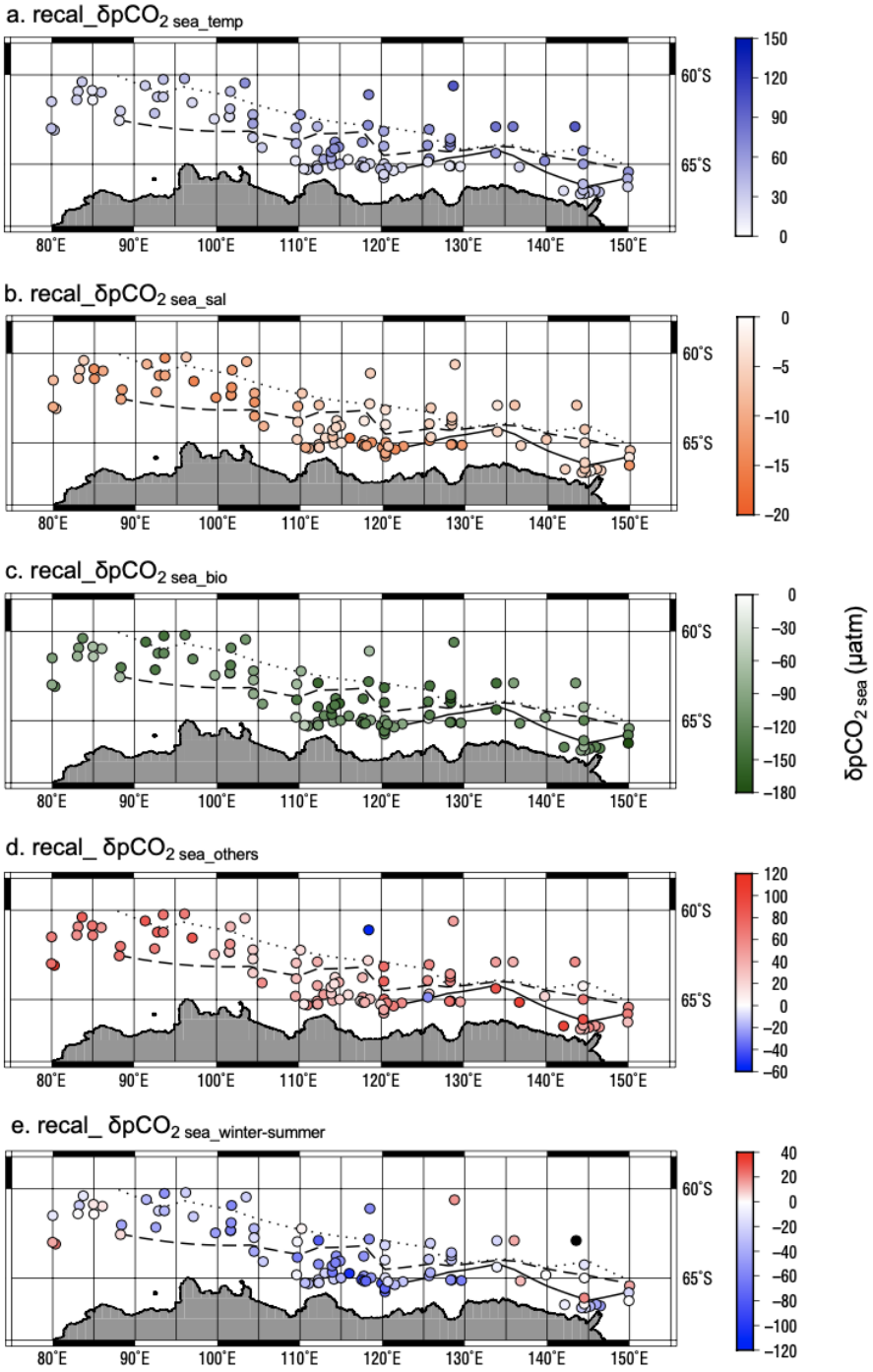

Figure 2.10. Spatial distribution of recalculated $\delta pCO_{2\ sea}$: (a) based on temperature ($recal\_\delta pCO_{2\ sea\_temp}$), (b) based on salinity ($recal\_\delta pCO_{2\ sea\_sal}$), (c) based on biological activity ($recal\_\delta pCO_{2\ sea\_bio}$), (d) based on other factors ($recal\_\delta pCO_{2\ sea\_others}$), and (e) $recal\_\delta pCO_{2\ sea\_winter\text{-}summer}$. SACCF: Southern Antarctic Circumpolar Current Front indicated by the dotted line. SB: Southern Boundary of ACC indicated by the dashed line. ASF: Antarctic Slope Front indicated by the solid line.

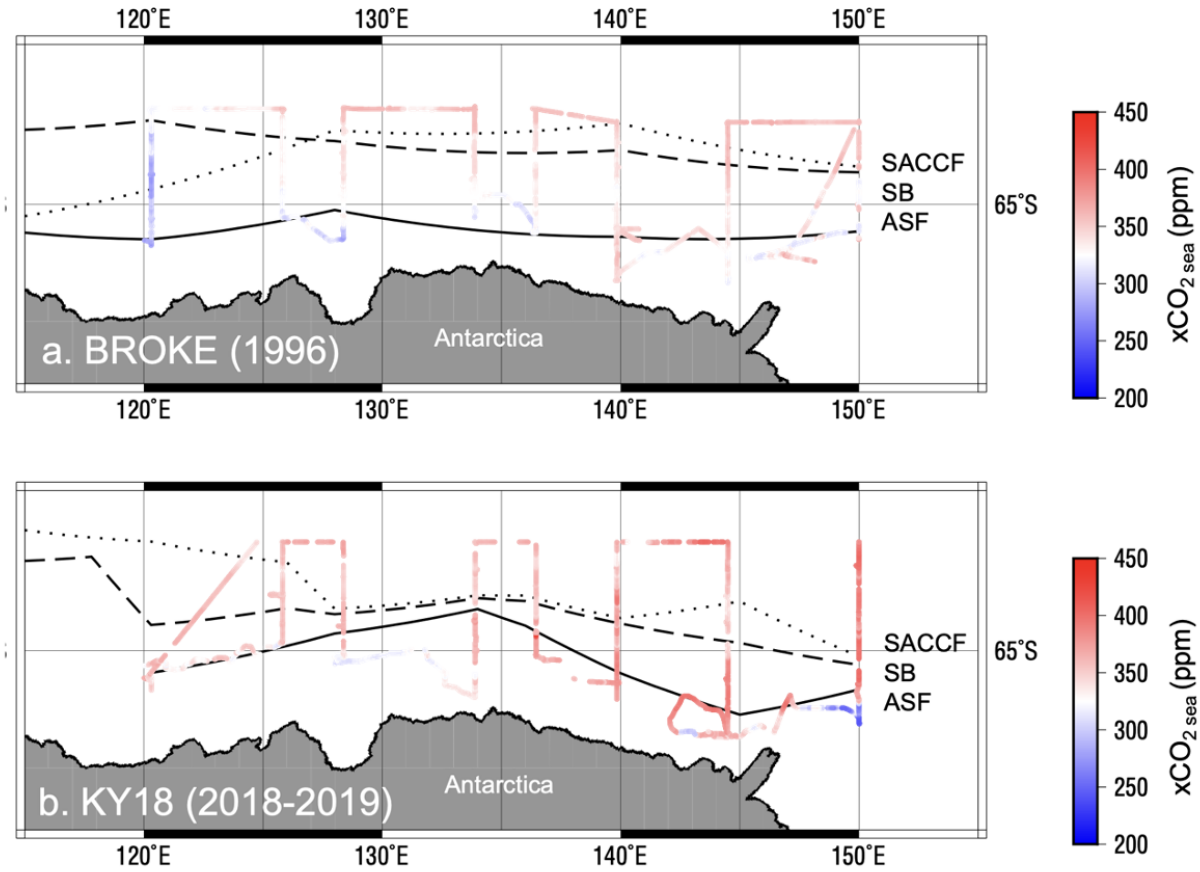

Figure 2.11. Spatial distribution of $xCO_{2\ sea}$ along cruise tracks (colored lines) during (a) BROKE (1996), (b) this study (2018–2019). SACCF: Southern Antarctic Circumpolar Current Front indicated by the dotted line. SB: Southern Boundary of ACC indicated by the dashed line. ASF: Antarctic Slope Front indicated by the solid line.

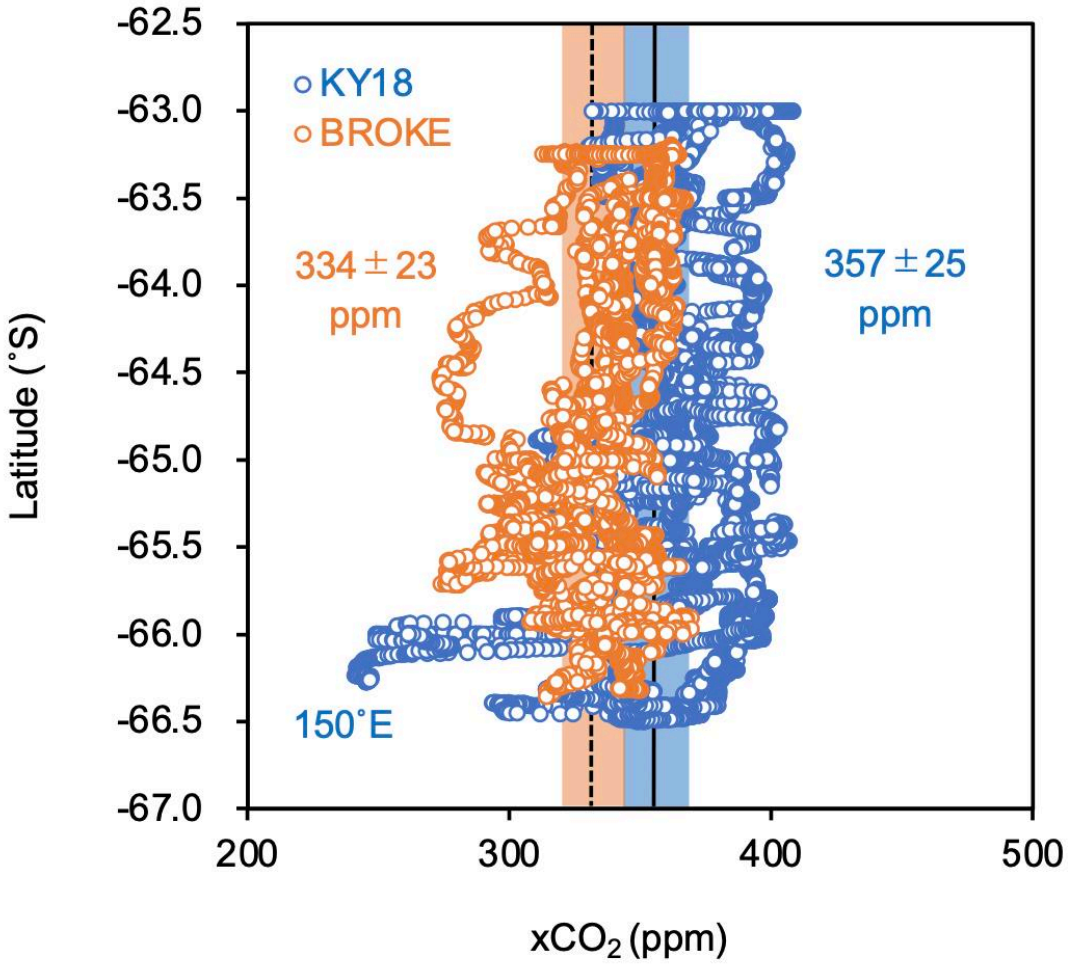

Figure 2.12. Latitudinal distribution of $xCO_{2\ air}$ (orange: BROKE; blue: this study). Black vertical dashed and solid lines are averages $xCO_{2\ air}$ during BROKE and this study, respectively. Widths of colored areas indicate standard deviations.

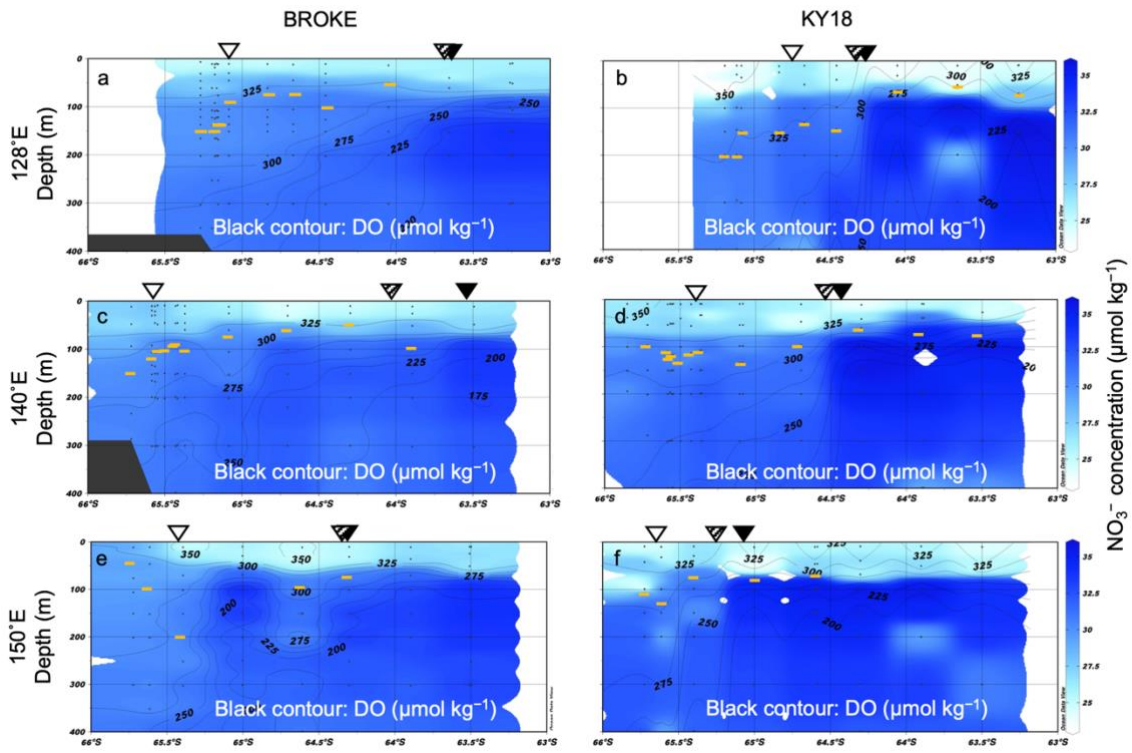

Figure 2.13. Nitrate concentrations as functions of depth and latitude along longitudes of (a), (b) 128 ℉; (c), (d) 140 ℉; and (e), (f) 150 ℉ (BROKE, KY18, respectively). Black contours indicate dissolved oxygen concentrations. This figure was built using Ocean Data View (Schlitzer, 2020). Depth of the TML was indicated by orange line. The frontal positions were indicated by open (ASF), shadow (SB), and solid (SACCF) triangles.

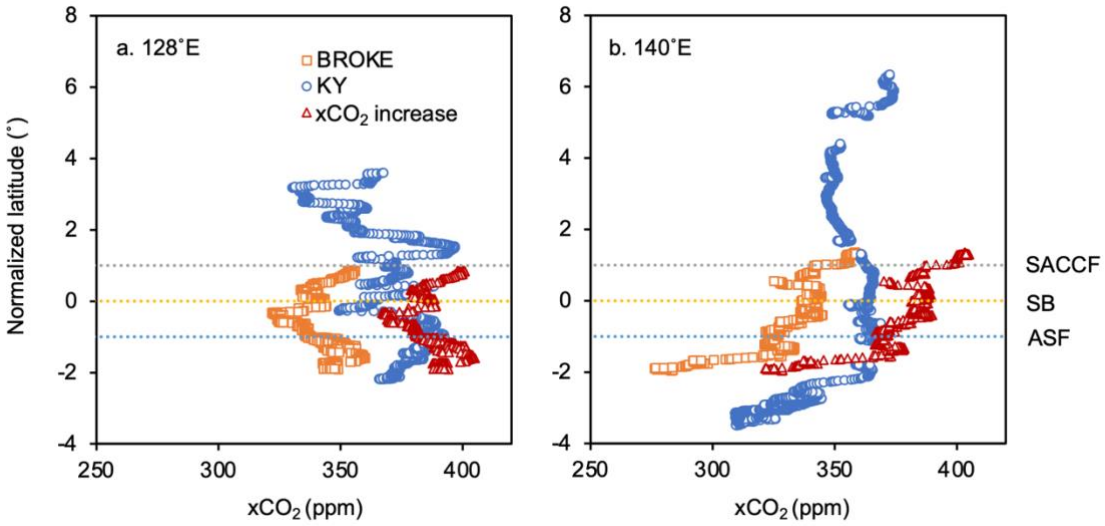

Figure 2.14. Relationship between normalized latitude and frontal distributions of $xCO_{2\ sea}$ (orange square: BROKE, blue circle: KY18, red triangle: $xCO_{2\ sea}$ increase). The Southern Antarctic Circumpolar Current Front corresponds to 1 on the ordinate; the Southern Boundary to 0, and the Antarctic Slope Front to −1. The $xCO_{2\ sea}$ increase was estimated by adding the difference between $xCO_{2\ air}$ in BROKE and this study (45 ppm) and the $xCO_{2\ sea}$ increase due to the increase of surface water temperature (about 1.5˚C) (4% $^{\circ}C^{-1}$) to the $xCO_{2\ sea}$ in BROKE.

3. Oceanographic factors determining the distribution of nutrients and primary production in the subpolar Southern Ocean

Abstract

To investigate the spatial distributions and determinants of nutrient concentrations, we measured NO_3^-+NO_2^-, PO_4^{3-}, and $Si(OH)_4$ concentrations in the eastern Indian Ocean sector of the Southern Ocean (80−150˚E, south of 60˚S) between December 2018 and February 2019. In the region influenced by the Antarctic Circumpolar Current, nutrient concentrations were increased by nutrients supplied from the deep layer and by organic matter decomposition and remineralization within the seasonal pycnocline after the development of strong stratification. Strong stratification also enhanced phytoplankton growth and nutrient consumption by photosynthesis. In contrast, in the subpolar region, nutrient concentrations were increased by nutrients supplied by brine discharged during sea ice formation and decreased by dilution with sea ice meltwater. Although high salinity in the surface and subsurface layers corresponded well to upwelling areas around subpolar subgyres, high salinity was not necessarily correlated with nutrient concentrations. We estimated primary production both from in situ nutrient data and from satellite-acquired chlorophyll-*a* data. According to both estimation methods, primary production was high in the subpolar region, especially around 120−130˚E. However, nutrient-based estimation also showed high production in coastal areas where, because of sea ice and cloud cover, estimation based on satellite data was not possible. To understand primary production in seasonal ice areas, the best estimation method should be selected for the research goals or multiple methods should be used in combination.

3.1. Introduction

In the Southern Ocean, primary production supports a rich ecosystem and creates a strong carbon sink (e.g., Takahashi et al., 2012). In the mid-latitudes, primary production is limited mainly by light and macronutrient (NO_3^-+NO_2^-, PO_4^{3-}, and $Si(OH)_4$) concentrations. When sufficient nutrients are present in the photic layer, phytoplankton consume nutrients for photosynthesis and cease photosynthesis when any of the nutrients becomes depleted. In polar regions, however, light availability varies seasonally because of the formation of sea ice during winter; the lack of light

under the sea ice limits primary production. After the sea ice melts, the phytoplankton resume photosynthesizing. In addition to light and the nutrients mentioned above, phytoplankton need iron for primary production (e.g., Benner, 2011). In the Southern Ocean, which is a high-nutrient low-chlorophyll region (Martin et al., 1990; Sakshaug, 2004; Popova et al., 2010), a lack of iron also limits primary production. The Southern Ocean is far from continental sources of iron; therefore, in most of the Southern Ocean, primary production is low because of an iron limitation (Martin et al., 1990). However, when sea ice forms, it takes up iron from under-ice water, and during the sea ice melting season iron may be supplied to the Southern Ocean in the meltwater (Lannuzel et al., 2008), thereby contributing to photosynthesis by phytoplankton. Estimates by Duprat et al. (2019), based on sea ice samples from Prydz Bay, indicate that during the melting season 0.6 ± 0.2 ton day^{-1} of dissolved iron is supplied to the eastern bayshore area and then transported to iron-limited offshore areas, where up to 170 mg C m^{-2} day^{-1} of biomass can be generated.

In the Southern Ocean, which plays a pivotal role in the global biogeochemical cycle, several factors determining nutrient distributions have been identified (e.g., Nissen et al., 2021; Iida et al., 2013). Nutrient concentrations are affected by oceanographic factors such as oceanic circulation as well as by biogeochemical factors such as remineralization during organic matter decomposition (e.g., Codispoti et al., 2013). For example, isopycnal mixing by eddies homogenizes nutrient concentrations and suppresses remineralization by organic matter decomposition and silicate dissolution (Pollard et al., 2006). During sea ice formation, brine with high nutrient concentrations is discharged, whereas when the sea ice melts, nutrient concentrations in the surface layer may be either diluted or increased, depending on whether the nutrient concentrations in the sea ice are higher than those in the surface layer (Fripiat et al. 2017; Sahashi et al., 2022).

In the eastern Indian sector of the Southern Ocean, the research area in this study, Hirano et al. (2021) have recently shown that Circumpolar Deep Water (CDW) that originates in the Antarctic Circumpolar Current (ACC) is transported to the continental shelf by subpolar subgyres. In addition, Yamazaki et al. (2021) have shown that the southern boundary of the ACC moved southward from the 1990s to the 2010s, and we observed increased subsurface nutrient concentrations and biological activity associated with the resultant displacement of deep water, as mentioned in section 2.4.5. Furthermore, studies of krill and cetacean distributions (Tynan, 1998; Matsuoka et al., 2003), satellite chlorophyll observations (Sokolov and Rintoul, 2007), and observations of submesoscale mixing (Siegelman et al., 2019) have demonstrated the importance of ocean front structures to Antarctic marine ecosystems. Mori et al. (2022) showed by using satellite-

derived sea surface velocities that toothfish eggs and fry are transported by the subarctic circulation in the Indian Ocean sector, and Thorpe et al. (2007) showed that the interaction between circulation and sea ice strongly influences the krill distribution in the Southern Ocean. Thus, oceanographic factors in the Southern Ocean strongly influence nutrient distributions and marine ecosystems, but the direct and indirect relationships between these factors and primary production are still being studied.

In Chapter 2, we quantitatively assessed the factors influencing sea surface pCO_2 variations from winter to summer, and we reported that biological activity in summer decreased pCO_2 by 92 μatm on average. This increase greatly offsets the increase in pCO_2 associated with increasing water temperatures and keeps ocean surface pCO_2 under-saturated with respect to the atmosphere. Therefore, the estimation of primary production in this area is important for understanding the carbon cycle. Two methods are commonly used to estimate primary production. One popular method uses satellite-based chlorophyll-*a* data (Hirawake et al., 2017). Satellite-based estimation of primary production has the advantage that it can be applied in large areas and over long time periods, including in sea ice areas. However, it has the disadvantage that satellite data cannot be acquired beneath clouds or sea ice. Primary production can be estimated from nutrient consumption (e.g., Shadwick et al., 2014) in any environment where water sampling is possible, although the use of in situ nutrient data has the disadvantage that it requires ship observations, which limits the observation area. Moreover, by using nutrient data obtained by vertical sampling, primary production can be estimated in the entire water column. Although both methods have been used in the Southern Ocean, the consistency of estimates obtained by the two methods has not been fully explored. Thus, comparing and evaluating estimates obtained by the two methods is important for future research on primary production in this region.

In this study, we used data from oceanographic observations conducted in 2018/2019 in the eastern Indian sector of the Southern Ocean to investigate both vertical and horizontal distributions of nutrients and inferred the factors dominantly responsible for distributional differences. We then used the observed nutrient data to estimate primary production and compared the results with satellite-based primary production estimates. Finally, we assessed the validity and applicability of each method in this region.

3.2. Materials and methods

3.2.1. Sampling

In situ nutrient water samples were collected during survey KY1804 by R/V *Kaiyo-Maru* (Fisheries Agency of Japan) in the eastern Indian sector of the Southern Ocean from 12 December 2018 to 8 January 2019 (Leg 1; 60−66˚S, 80−120˚E) and from 25 January to 24 February 2019 (Leg 2; 63−65˚S, 113−150˚E) (Figure 3.1). The sampled area covers the full longitudinal range included in Division 58.4.1 of the Commission for the Conservation of Antarctic Marine Living Resources (https://www.ccamlr.org/en/organisation/home-page). This study was conducted as a part of a multidisciplinary ecosystem survey in the eastern Indian Ocean sector of the Antarctic with a focus on Antarctic krill.

Sea surface temperature (SST), sea surface salinity, and fluorescence were measured continuously with an electronic plankton counting and sizing system (Nippon Kaiyo Co., Ltd., Tokyo, Japan). Temperature and salinity were measured with an SBE 3 plus temperature sensor and an SBE-4C conductivity sensor, respectively (Sea-Bird Scientific, Bellevue, WA, USA), with a precision of ±0.005˚C and ±0.001, respectively. These temperatures were slightly biased by a rise in the temperature of the seawater while samples were being collected. Vertical profiles of temperature, salinity, and dissolved oxygen were measured with a CTD probe (SBE 3 plus, SBE-4C, and SBE 43, Sea-Bird Scientific) that was calibrated by the manufacturer before and after the cruise. The precisions of dissolved oxygen with this probe was ±0.1 ml L^{-1}. In addition, seawater samples were collected to calibrate the salinity sensor. Seawater samples for measurements of nutrients were collected along vertical profiles in rosette-mounted, 10-L Niskin bottles (Ocean Test Equipment, Inc., Ft. Lauderdale, FL, USA). The samples were subsampled into 10-mL polyethylene screw-cap vials (Eiken Chemical Co., Ltd, Tokyo, Japan) for measurement of inorganic nutrient concentrations (NO_3^-+NO_2^-, PO_4^{3-}, $Si(OH)_4$) and stored in a freezer (−30˚C) until analysis in the laboratory on land.

3.2.2. Sample analysis

The concentrations of nutrients in the seawater were determined in accord with the Joint Global Ocean Flux Study (JGOFS) spectrophotometric method (JGOFS, 1994) using QuAAtro 2-HR (BL-

tec, Osaka, Japan) and Seal Analytical (Norderstadt, Germany) autoanalyzer systems, which were calibrated with reference materials for nutrient analysis (Lots BZ, CB, and CC; KANSO Technos Co., Ltd., Osaka, Japan). Twenty subsamples of the reference water samples for NO_3^-+NO_2^-, PO_4^{3-}, and $Si(OH)_4$ (9.8, 2.1, and 117.5 μmol L^{-1}, respactively) yielded standard deviations of 0.3, 0.1, and 1.1 μmol L^{-1}, respectively. Four standards (3.0, 11.9, 23.8, and 74.3 μmol L^{-1} for NO_3^-+NO_2^-, 0.19, 0.78, 1.55, and 4.85 μmol L^{-1} for PO_4^{3-}, and 7.1, 28.5, 57.0, and 178.0 μmol L^{-1} for $Si(OH)_4$) were used to make calibration curves for each measurement ($r > 0.998$). Data that appeared to be outliers were removed: for each 30 dbar pressure range from 100 to 400 dbar and each 100 dbar pressure range from 100 to 2000 dbar, outliers were defined as values outside of three standard deviations of all bottle data.

3.2.3. Satellite images

We used satellite remote sensing data to understand the oceanographic environment in the study area during the austral summer of 2018/2019. Satellite images of sea ice concentrations (SIC) near sampling stations with a spatial resolution of 10 km × 10 km and a temporal resolution of 1 day were derived from passive microwave imagery from the Advanced Microwave Scanning Radiometer 2 onboard the GCOM-W satellite provided by the Arctic Data Archive System, National Institute of Polar Research, Japan (https://ads.nipr.ac.jp/dataset/A20170123-003). In this study, we used monthly averaged sea ice concentrations. Monthly averaged SST (Figure 3.2) and chlorophyll-*a* concentrations were derived from satellite images in the moderate resolution imaging spectroradiometer (MODIS) database provided by the NASA Oceancolor web site (https://oceancolor.gsfc.nasa.gov/) with a spatial resolution of 9 km × 9 km. Satellite-based ocean productivity data were obtained from the Oregon State ocean productivity web site (http://sites.science.oregonstate.edu/ocean.productivity/). In this product, net primary production (NPP) is estimated by the Vertically Generalized Production Model (VGPM) (Behrenfeld and Falkowski, 1997) as a function of chlorophyll-*a*, available light, and photosynthetic efficiency. This model uses chlorophyll-*a*, temperature, and photosynthetic available radiation (PAR) data from MODIS satellites, along with estimates of euphotic zone depth obtained with a model developed by Morel and Berthon (1989) and based on the chlorophyll-*a* concentration. The spatial resolution of these data is 9 km × 9 km, and the temporal resolution is monthly. We also used satellite remote sensing sea surface salinity data (Figure 3.2) from the Soil Moisture Active Passive (SMAP) observatory database provided by the NASA Physical Oceanography Distributed Active Archive

Center (https://podaac.jpl.nasa.gov/). We downloaded the JPL SMAP Level 3 CAP Sea Surface Salinity Standard Mapped Image Monthly V5.0 Validated Dataset, which has a spatial resolution of 0.25˚ × 0.25˚.

3.3. Results

3.3.1. Meridional and zonal sections

In meridional sections, the vertical distributions of NO_3^-+NO_2^- and PO_4^{3-} were very similar (Figures. 3.3a–j, 3.4a–f). These nutrients were low in the surface layer, reached a maximum at about 100–200 dbar depth in the subsurface, and were generally uniform below that depth interval. The vertical distribution of $Si(OH)_4$ was different (Figures. 3.4k–o, 3.4g–i); like NO_3^-+NO_2^- and PO_4^{3-}, $Si(OH)_4$ was low in the surface layer, but then its concentration increased with depth, reaching a maximum in the deep layer. NO_3^-+NO_2^- and PO_4^{3-} concentrations were high in the upper part of the 1.5˚C isotherm (white contours). These distributions showed few east-west and north-south differences, with broad distributional trends generally consistent.

3.3.2. Horizontal distributions

Figures 3.5 shows the horizontal distributions of nutrients at 10 m depth and in the temperature minimum (T-min) layer (i.e., the depth at which the lowest temperature was observed at each observation point). Distributions at 10 m depth reflect primary production and are expected to show large seasonality due to sea ice and other factors. In contrast, in the temperature minimum layer, seasonality associated with sea ice and biological activity is expected to be small. At 10 m depth, nutrient concentrations were lower offshore, while high concentrations were observed in the coastal area and at 80 and 90˚E. In addition, relatively high concentrations were observed at 110–120˚E. At T-min, nutrient concentrations also tended to be lower offshore and higher in the coastal area, especially east of 140˚E.

Figures 3.6a-d show the horizontal distributions of temperature and salinity at 10 m depth and in the T-min layer. At 10 m depth, temperature and salinity were low toward the west and high toward the east (Figures. 3.6a, c). Figures 3.5e and f represent the density difference between 10 m and 100 m,

and ice-free period (Number of days between the first time SIC fell below 15% after 1 November and the date of observation), respectively. As mentioned above, distributions at 10 m depth were affected by seasonal factors, such as sea ice. This distribution may indicate a larger influence of sea ice meltwater in the west, where there is a greater amount of sea ice, and a clockwise circulation field. In the low-salinity areas, the stronger stratification at depths shallower than 100 m (Figure 3.6e) supports this inference, because sea ice melting significantly affects surface stratification. In addition, higher temperatures in both the surface and subsurface layers in the eastern part reflect the gradual southward migration of the eastward-flowing ACC in this region. The area of high-salinity water observed in the surface layer at 110−120˚E (Figure 3.6c) corresponds well to the upwelling region of subpolar circulation (Yamazaki et al., 2020). Moreover, at the same location, the cumulative thickness of sea ice meltwater estimated from oxygen stable isotope ratios was the smallest in the area of observation (Aoki et al., 2023).

3.4. Discussion

3.4.1. Determinants of vertical and horizontal distribution of nutrients

Nutrients are consumed by phytoplankton during photosynthesis, and they are remineralized during organic matter decomposition or by the dissolution of diatom frustules. The concentrations of all nutrients are low in the euphotic layer because of biological activity, whereas the influence of biological activity is small in the aphotic layer (below the subsurface layer). In the aphotic layer, nutrient concentrations are determined by organic matter decomposition, and the distribution of each nutrient is determined by its rate of remineralization. NO_3^-+NO_2^- and PO_4^{3-} are contained in organic matter, so these nutrients are remineralized rapidly when the organic matter decomposes. As a result, their concentrations are high in the pycnocline, where organic matter decomposition is active. In contrast, $Si(OH)_4$ occurs in diatom frustules, which are less soluble than organic matter (e.g., Kamatani and Ueno, 1980). Therefore, $Si(OH)_4$ is not remineralized in the pycnocline and is high in the deeper layer because diatom frustules generally dissolve after sedimentation. We observed this general difference in distribution in our study region.

The maximum concentrations of NO_3^-+NO_2^- and PO_4^{3-} in the subsurface layer coincided with the upper part of the 1.5˚C line (Figures. 3.3 and 3.4, white contour). The 1.5˚C isotherm indicates the southern boundary of the ACC (Orsi et al., 1995), and this represents the southern boundary of

upwelling of Circumpolar Deep Water (CDW), which is characterized by an oxygen minimum layer. The CDW, which dominates the northern and eastern parts of the study region, is rich in nutrients (e.g., Prézelin et al., 2000); thus, nutrients transported by the inflowing CDW may explain the large maximum nutrient concentrations observed in the subsurface layer in those areas (Figures. 3.3e, j, 3.4a−b, d−e).

Considering the horizontal differences, nutrient concentrations were lower offshore, possibly reflecting active primary production in the offshore region. In contrast, high nutrient concentrations were observed in the coastal area and at 80 and 90˚E. These values may be due to the relatively short time since the sea ice retreat in these areas (Figure 3.6f), thus, to less biological production and therefore less consumption of nutrients. In addition, deep mixing in the coastal area (Figure 3.6e) would have prevented phytoplankton from remaining at a suitable depth for growth, thereby limiting biological production and resulting in low nutrient consumption (Matsuno et al., 2023).

The influence of the oceanographic field is expected to be more apparent where there is less biological activity. The relatively high nutrient concentrations at 110−120˚E appear to correspond to the upwelling area of the CDW, as suggested by the high salinity in that area. The concentrations of nutrients contained in the sea ice sampled during this cruise were significantly lower than their concentrations in seawater (Nomura et al., 2023); therefore, meltwater would be expected to dilute nutrient concentrations. Because upwelling areas are generally characterized by divergent flows and southward currents (e.g., Yamazaki et al., 2020), we can infer that sea ice meltwater inflow from the coast was lower at 110−120˚E.

At T-min, nutrient concentrations were lower offshore and higher in the coastal area (Figures. 3.5b, d, f). These high nutrient concentrations east of 140˚E correspond to high salinity in the subsurface layer (Figure 3.6d), which likely reflects the influence of a polynya off the Adélie Coast (136−142˚E). In general, brine discharged during sea ice formation has high nutrient concentrations (Fripiat at al., 2017). In addition, the temperature minimum layer preserves the water mass characteristics of the winter mixing layer (Pondaven et al., 2000). Therefore, high nutrient concentrations in the coastal area can be interpreted as reflecting brine rejection during winter sea ice formation. Also, offshore (63–64˚S) nutrient concentrations were higher at 140˚E compared to the surrounding area. This result suggests that in this area, nutrients may have been supplied by the inflow of CDW from offshore. The low concentrations of $Si(OH)_4$ observed in some locations (62˚S, 100˚E and 64˚S, 150˚E), where concentrations of NO_3^-+NO_2^- and PO_4^{3-} were high, can be

explained by the influence of organic matter decomposition.

3.4.2. Frontal zones and vertical profiles

There are three oceanographic fronts in the study region: the Southern ACC Front (SACCF), the Southern Boundary (SB), and the Antarctic Slope Front (ASF) (Sokolov and Rintoul, 2007). The front positions were determined from the in situ temperature profiles, and the zones in which the observation points were located were defined based on these front positions (Figure 3.1) (Yamazaki et al., this issue). In this region, however, the SACCF branches off upstream near the Kerguelen Plateau and does not exhibit a pronounced frontal structure, so we refer to the entire area north of the SB, which is the southern boundary of the poleward upwelling area of the Upper CDW (oxygen minimum layer), as the Southern Zone. We refer to the area south of the SB and north of the ASF as the Subpolar Zone. This zone characteristically includes cyclonic circulations such as the Weddell Gyre, and it is bounded on the south by westward currents on the shelf slope associated with the ASF. The cyclonic circulation in the Subpolar Zone includes subgyres that are related to the continental shelf slope structure, which controls CDW upwelling and shoreward transport (Yamazaki et al., 2020; Hirano et al., 2021). The area south of the ASF is the Continental Zone. In general, the area south of the SB corresponds to the seasonal ice zone The division of the study region into zones by these fronts is also reflected in the ecosystems. In the eastern and western Indian Ocean sectors, Antarctic krill are mainly distributed between the outer edge of the continental shelf (the shelf break, approximately corresponding to the ASF) and the SACCF (i.e., the Southern and Subpolar zones) (Nicol and Raymond, 2012); thus, in this area, the ecosystem is krill-based. Farther north, is a copepod- and fish-based ecosystem (Pruvost et al., 2005). These two ecosystems are separated by a transitional zone (McCormack et al., 2020). On the continental shelf itself (Continental Zone), the krill species *Euphausia crystallorophias* is dominant. The presence of these fronts could significantly affect the water mass characteristics and the horizontal distribution of nutrients. In the following, we will discuss the vertical distribution of nutrients in each front zone.

As in the meridional sections (Figure 3.3), in the averaged vertical profiles of nutrient concentrations in each frontal zone, NO_3^-+NO_2^- and PO_4^{3-} show similar trends (Figures. 3.7a–f), but $Si(OH)_4$ shows a different trend (Figures. 3.7g–i). In the Southern Zone, NO_3^-+NO_2^- and PO_4^{3-} concentrations in the subsurface layer were higher than they were closer to the continent (Figures.

3.7a, d), possibly because the nutrients were derived from the CDW. Conversely, $Si(OH)_4$ tended to be slightly lower farther offshore, possibly because $Si(OH)_4$ is transported by continental shelf water. In addition, concentration maxima of NO_3^-+NO_2^- and PO_4^{3-} were observed in the inverse layer (yellow layer in Figure 3.7), which is the layer where water temperature increases with depth, in the Southern Zone, but in the Subpolar Zone and Continental Zone, their concentrations increased gradually with depth to a constant value (Figures. 3.7b−c, e−f). In all three zones, $Si(OH)_4$ increased continuously with depth. These characteristics of the distribution of each nutrient for each zone were consistent with the GLODAPv2 data (Key et al., 2015; Olsen et al., 2016) in the same area in February 2018 (Gray lines in Figure 3.7).

We compared these vertical profiles of nutrients with those of conservative temperature (θ), absolute salinity (S_A), Apparent Oxygen Utilization (AOU), and buoyancy frequency (N^2) (Figure 3.8). AOU was determined as the difference between the measured dissolved oxygen and saturation oxygen concentration, calculated by using temperature and salinity. In the Southern Zone, these parameters changed more rapidly in the subsurface layer (100−200 m) than they did in the zones closer to the continent. The vertical profiles of buoyancy frequency (Figures. 3.8g−i) show that stratification at the base of the mixing layer became stronger further offshore. When stratification is strong, organic matter is more likely to remain within the pycnocline, where organic matter decomposition is active. As a result, NO_3^-+NO_2^- and PO_4^{3-} were remineralized as described in section 3.4.1; in contrast, $Si(OH)_4$ was not remineralized in the pycnocline because diatom frustules take a long time to dissolve. This difference may explain why maxima were observed for NO_3^-+NO_2^- and PO_4^{3-}, but not for $Si(OH)_4$, in the Southern Zone. The possible decomposition of organic matter at the base of the mixing layer is also supported by the high AOU there (Figure 3.8d). In the Southern Zone, the temperature maximum layer, which is located on average at 300−400 m, corresponds to the oxygen minimum layer, which constitutes the Upper CDW (Whitworth et al., 1998). Although CDW is also considered to present a high AOU, the water mass is very low in salinity compared to the CDW (Figure 3.8d); therefore, the formation of extremely high AOU water is inferred to be a result of local organic matter decomposition.

To verify the influence of CDW and organic matter decomposition on nutrient concentrations, we examined the relationships between nutrients and salinity in the inverse layer (Figure 3.9). $Si(OH)_4$ showed a strong positive correlation with salinity in all zones (Southern Zone, $r = 0.67$; Subpolar Zone, $r = 0.97$; Continental Zone, $r = 0.92$; all $p < 0.01$; Figures. 3.9g−i). The correspondence between $Si(OH)_4$ and the physical oceanography in the inverse layer is also evident in their vertical

profiles (Figures.3.7, 3.8); this correspondence suggests that the $Si(OH)_4$ distribution is determined by the CDW. $NO_3^-+NO_2^-$ showed a significant weak to moderate positive correlation to salinity in the Subpolar Zone and Continental Zone (Subpolar Zone, $r = 0.53$, $p < 0.01$; Continental Zone, $r = 0.28$, $p < 0.01$; Figure 3.9b–c) but no such trend was observed in the Southern Zone ($r = -0.19$, $p = 0.22$, Figure 3.9a). Similar to $NO_3^-+NO_2^-$, a positive correlation was also observed between PO_4^{3-} and salinity in the Subpolar and Continental Zones (Subpolar Zone, $r = 0.58$, $p < 0.01$; Continental Zone, $r = 0.35$, $p < 0.01$, Figure 3.9e–f), whereas no correlation was found in the Southern Zone ($r = 0.14$, $p = 0.36$, Figure 3.9d). In addition to the inflow of CDW, the effect of organic decomposition may explain this trend.

.

The relationship between salinity and AOU can be an indicator of organic matter decomposition. The overall strong negative correlation between AOU and salinity in the inverse layer (Figure 3.10) indicates that the values of both were determined by oceanographic factors. However, values for the Southern Zone plotted below the regression line (Figure 3.10a), and they were also associated with high $NO_3^-+NO_2^-$ concentrations (Figure 3.10b). This result supports the occurrence of organic matter decomposition. On the other hand, in the Continental Zone, salinity and AOU may have plotted under the regression line (Figure 3.10a) because of an increase in subsurface salinity following brine rejection. Although Briggs et al. (2018), using Biogeochemical (BGC) Argo float data, showed that organic matter degradation is also active under sea ice in winter, in the inverse layer of the Subpolar and Continental zones, both of which are seasonal sea ice zone, an organic matter decomposition signal (high AOU relative to the regression line) was rarely observed (Figure 3.10a). It is likely that the ratio of oxygen to salinity did not change before and after decomposition, due to the inflow of CDW with progressive decomposition in this zone.

3.4.3. Primary Production

3.4.3.1. Nitrate-based estimation

The temperature minimum layer described in section 3.4.1 refers only to the depth at which the lowest water temperature was observed at each point. When determined by the method of Tomczak and Liefrink (2005) ($-1.9^\circ C < T < -1.5^\circ C$, $34.2 < S < 34.5$), however, the temperature minimum layer retains surface characteristics in winter (Pondaven et al., 2000). As a result, biological nutrient

consumption can be estimated from nutrient concentration differences between the temperature minimum layer and the surface, and used to calculate Net Community Production (NCP); i.e., Gross primary production minus ecosystem respiration (e.g., Shadwick et al., 2014; Tamura et al., 2022). However, in Southern Zone, where nutrient concentrations are influenced by organic matter decomposition as described in section 3.3.1.3, and the sea ice-formation area (Continental zone), which is affected by brine rejection, may have different characteristics from other zones. In this study, we assumed that the mean NO_3^-+NO_2^- concentration in the water temperature minimum layer, as defined by Tomczak and Liefrink (2005), in the Subpolar Zone, represented the surface concentration in winter and used that value to calculate the integrated NCP from the surface to 100 m depth.

$$\mathrm{NCP\_N} = \left(\int_{z=\mathrm{surface}}^{z=100} [N]^{\mathrm{winter}} - [nN]^{\mathrm{obs}}\, dz\right) \times 7.5 \quad (1)$$

where z is depth, $[N]^{\mathrm{winter}}$ is the average [NO_3^-+NO_2^-] in winter, and $[nN]^{\mathrm{obs}}$ is the salinity normalized [NO_3^-+NO_2^-] during the observation. Here, $[N]^{\mathrm{winter}}$ was 31.2 ± 0.8 μmol L^{-1}. In diatom-predominant regions, the C/N ratio is approximately 7.5, different from the Redfield ratio (DeJong and Dunbar, 2017). Therefore, in equation (1), we multiplied the integrated [NO_3^-+NO_2^-] by 7.5 to convert it to carbon content.

By integrating NCP estimated by equation (1) from winter to the time of observation, we obtained a mean NCP of 2.0 ± 1.0 mol C m^{-2} (Figure 3.10a). Roden et al. (2016) estimated NCP in the southwest Indian Ocean sector (30−80˚E) during the same season by similar methods as 0.9 ± 0.6 mol C m^{-2} (30−45˚E) offshore and 0.9 ± 0.4 mol C m^{-2} (45−80˚E) and 2.1 ± 1.1 mol C m^{-2} in coastal areas. These values are generally consistent with our estimates.

Estimated NCP values were relatively high south of 65˚S at 110−130˚E, and the maximum NCP in the coastal zone of 4.9 mol C m^{-2} occurred at 130˚E. The high primary production at 110−120˚E generally corresponds to the area where CDW upwelling associated with subgyre circulation occurs. High NCP estimates were also obtained on the continental shelf at 150˚E, where warm CDW is also predominant in the subsurface on the upper continental shelf slope (Yamazaki et al., this issue). In contrast, NCP estimates were low offshore at 140˚E (63−64˚S), despite the high NO_3^-+NO_2^- in the temperature minimum layer (Figure 3.5b) and the low NO_3^-+NO_2^- at 10 m (Figure 3.5a). Because CDW flows from offshore into the area around 140˚E, vertical NO_3^-+NO_2^- consumption is likely underestimated there because the re-supply of nutrients to the shallower layer

counterbalances their consumption by biological activity. Similarly, primary production may be underestimated at some offshore stations, resulting in a discrepancy between NCP estimates and the strong offshore productivity inferred as described in section 3.4.1.

3.4.3.2. Silicate-based estimation

We also calculated NCP in the same way as in 3.4.3.1, using silicate concentrations;

$$\mathrm{NCP\_Si} = \left(\int_{z=\mathrm{surface}}^{z=100} [Si]^{\mathrm{winter}} - [nSi]^{\mathrm{obs}}\, dz\right) \times (106/15) \quad (2)$$

$[Si]^{\mathrm{winter}}$ was 66.3 ± 6 μmol L^{-1}. In equation (2), we multiplied the integrated [$Si(OH)_4$] by 106/15 following the Redfiled ratio.

$NCP_{\_Si}$ represents only primary production by diatoms. The difference between $NCP_{\_N}$ and $NCP_{\_Si}$ shows that $NCP_{\_Si}$ is higher than $NCP_{\_N}$ (Figure 3.11b). Because $Si(OH)_4$ is not related to the organic matter decomposition in surface layer, i.e., $NCP_{\_Si}$ is similar to the total production by diatoms. In contrast, the remineralization of NO_3^- occurred in the surface layer, which was consistent with the positive AOU values even at depths shallower than 100 m (Figure 3.8d, e, f).

3.4.3.3. Chlorophyll-based estimates

We compared primary production estimated by using nutrient concentrations with that estimated by using satellite-based chlorophyll-*a* data (Figures. 3.12b–f). Satellite remote sensing data were used to calculate NPP as follows (Behrenfeld and Falkowski, 1997):

$$\mathrm{NPP} = \mathrm{Chl.}\,a * P_{opt}^{B} * \mathrm{DL} * \frac{0.066125 * \mathrm{PAR}}{\mathrm{PAR} + 4.1} * z_{eu} \quad (3)$$

where Chl.*a* is the satellite-based chlorophyll-*a* concentration, P_{opt}^{B} is the chlorophyll-specific assimilation efficiency, DL is daylength, PAR is photosynthetic available radiation, and z_{eu} is the euphotic zone depth. As indicated in 3.2.3., NPP estimates by using satellite data were obtained from the Oregon Marine Productivity website

(http://sites.science.oregonstate.edu/ocean.productivity/).

Monthly averaged daily NPP estimates were low in November throughout the study area (Avg. 0.016 ± 0.004 mol C m^{-2} day^{-1}, Figure 3.11b), but in December they increased in some areas, such as where gaps in the coastal sea ice occurred (Avg. 0.023 ± 0.016 mol C m^{-2} day^{-1}, Figure 3.10c). In January, a band of significantly higher NPP was seen south of 60˚S at 90˚–140˚E (mean, 0.026 ± 0.014 mol C m^{-2} day^{-1}; Figure 3.10d), and a zonal structure in NPP was also seen in February (mean, 0.021 ± 0.009 mol C m^{-2} day^{-1}; Figure 3.11e). In March, NPP was again low across the region, indicating the end of the phytoplankton bloom (mean, 0.012 ± 0.004 mol C m^{-2} day^{-1}; Figure 3.11f). During December−January, chlorophyll-*a* was particularly high at 90−100˚E and 110−130˚E (Figures. 3.12c, d); from these locations, the water might be transported and merged by the eastward flow, resulting in zonally high NCP.

3.4.3.4. Comparison of methods for primary production

Here, we consider the two methods used to determine primary production. To compare the two results, the $NCP_{\_N}$ calculated on the basis of nutrients was divided by the period since sea ice retreat and converted to $NCP_{\_N}$ per day (Figure 3.12f). Because the satellite-method provides monthly averages, whereas nutrient-method provides averages for the entire period after sea ice retreat, removing seasonal variations, the results cannot be simply compared. However, the spatial distribution trends appear to be in general agreement between the two methods (Figure 3.12). Examination of the integrated values, while considering the monthly trends obtained from the satellite data, suggests that the higher integrated NCP values in the east may have been influenced by the eastward transport inferred in section 3.4.3.3, as well as by the timing of the phytoplankton bloom. In this area, the mean east–west flow is about 5−10 cm s^{-1} and the eddy diffusion flow is about 5 cm s^{-1} (Yamazaki et al., 2020); therefore, the water can be estimated to flow at about 10 cm s^{-1}. If it is assumed that the water mass is transported about 260 km (about 5˚ in longitude) in a month, then the water observed in February at 120−130˚E would represent inflow from the west of water affected by biological activity during December−January. This result is consistent with the high NCP estimates (Figure 3.11a). Although in some coastal areas where integrated NCP estimates were high, satellite-based data for calculating NPP were not available because of sea ice, in the offshore area (63−64˚S) where nutrient-based NPP estimates were low (Figure 3.12f), satellite-based NPP estimates were higher than in the surrounding area. Thus, in this case, the satellite-based

estimates corrected the underestimation obtained by using in situ nutrient data.

In situ nutrient data can be used for estimating primary production in seasonal ice zone whereas satellite data are not available in those areas. In addition, because the nutrient-based method uses data obtained at individual observation stations, comparisons with data for other parameters are facilitated. However, the nutrient-based method does not provide a history of seasonal changes in primary production from winter to the observation period. As a result, differences in NCP due to the timing of observations cannot be distinguished from differences due to differences in primary production capacity in individual areas. In addition, NCP is sometimes underestimated because nutrients are re-supplied before the observation period. Satellite data, which provide chlorophyll-*a* data from before the observation period, allow us to examine seasonal changes in primary production, thereby minimizing assessment errors due to the limited observation time.

Some recent studies have estimated primary production by observing changes in dissolved inorganic carbon and dissolved oxygen data obtained by BGC Argo floats (e.g., Briggs et al., 2018). The use of BGC Argo float data, which provide the history of biogeochemical composition changes, allows estimation of NCP under seasonal sea ice. Using BGC Argo float data, Briggs et al. (2018) found that the NCP under sea ice is balanced by the NCP in the spring, resulting in an annual NCP of almost zero. However, Argo floats cannot replace ship observations because their observation depth is limited and because sea ice sometimes prevents the floats from rising to the surface, resulting in a lack of data at those positions.

Thus, the two methods can yield different results, and each method has advantages and disadvantages. In seasonal sea ice zone, it is important to select the method appropriate for the research goal. For example, it may be reasonable to use a satellite-based method or one based on BGC float data if the aim is to examine temporal changes across a vast region, whereas if the aim is to investigate detailed NCP distributions and relationships with other parameters, then estimation of NCP from in situ nutrient data collected at individual stations is more suitable. Furthermore, although simple comparisons of the results obtained by the two methods are not appropriate, examination of the combined results can potentially clarify detailed spatial-temporal variations of primary production in seasonal ice zone.

3.4. Conclusion

In this study, we summarized the vertical and horizontal distribution of nutrient concentrations in the eastern Indian Ocean sector of the Southern Ocean and examined their determinants (Figure 3.14). The vertical distribution of nutrients observed in this study is consistent with the generally known characteristics of the vertical distribution of nutrient concentrations. Stronger stratification in the Southern Zone north of the Southern Boundary, with higher nutrient concentrations at around 200 m depth, suggests that organic matter decomposition may have occurred. Horizontal distributions were dominantly affected by oceanic circulation, including that related to sea ice formation/melting and CDW upwelling and inflow. The strength of the stratification also may facilitate nutrient remineralization during organic matter decomposition and also have enhanced nutrient consumption for photosynthesis by phytoplankton in the surface layer.

Our results indicate that the oceanographic environment has a strong influence on the distribution of nutrient concentrations. For this reason, environmental changes such as a sea ice reduction and front migration have the potential to alter future nutrient distributions. Such changes would directly affect primary production and ultimately the entire ecosystem and the transport of carbon to the deep layer. Therefore, continuous monitoring of nutrient concentrations with high spatial-temporal resolution is required.

The estimation of primary production from nutrient concentrations allows NCP to be calculated in sea ice areas, where it cannot be estimated by using satellite data. However, to understand the strength and distribution of primary production, it is important to obtain information about its temporal (monthly) and spatial variations by using satellite data. In seasonal ice zone, results obtained by using a combination of in situ nutrient-based and satellite-based methods, along with results obtained by using BGC Argo float data, should improve our understanding of ecosystems during periods for which observations are not available.

Acknowledgements

We thank the officers, crew, and scientists onboard R/V *Kaiyo-Maru* for their dedication to the fieldwork. The *Kaiyo-Maru* survey was supported by the Institute of Cetacean Research and Japan Fisheries Research and Education Agency, Fisheries Agency of Japan. This work was supported by

grants from the Japan Society for the Promotion of Science (21H04931, 20H04345, 17H04715, 15H05116), General Collaboration Projects 2-13 and a grant for young scientists of the National Institute of Polar Research, the Joint Research Program of the Institute of Low Temperature Science, Hokkaido University.

Data Availability Statement

This chapter is a modified version of Tozawa et al. (2024a). Data and support information for this research are available from Tozawa et al. (2024a).

References

Aoki, S., Yamazaki, K., Hirano, D., Nomura, D., Sasaki, H., Murase, H. (2023). Distribution of stable oxygen isotope of sea water and implication on freshwater cycle off the coast from Wilkes to George V Land, Antarctica. *Progress in Oceanography*, Volume 217, 103101, ISSN 0079-6611. https://doi.org/10.1016/j.pocean.2023.103101

Behrenfeld, M.J and Falkowski, P.G. (1997). Photosynthetic rates derived from satellite-based chlorophyll concentration. *Limnology and Oceanography*, 42, 1−20. https://doi.org/10.4319/lo.1997.42.1.0001

Benner, R. (2011). Loose ligands and available iron in the ocean. *Proceedings of the National Academy of Sciences*, 108, 3, 893−894. https://doi.org/10.1073/pnas.1018163108

Briggs, E. M., Martz, T. R., Talley, L. D., Mazloff, M. R., Johnson, K. S. (2018). Physical and biological drivers of biogeochemical tracers within the seasonal sea ice zone of the Southern Ocean from profiling floats. *Journal of Geophysical Research: Oceans*, 123, 746−758. https://doi.org/10.1002/2017JC012846

Codispoti, L. A., Kelly, V., Thessen, A., Matrai, P., Suttles, S., Hill, V., Steele, M., Light, B. (2013). Synthesis of primary production in the Arctic Ocean: III. Nitrate and phosphate based estimates of net community production. *Progress in Oceanography*, 110, 126–150. doi:

10.1016/j.pocean.2012.11.006.

DeJong, H. B. and Dunbar, R. B. (2017). Air−sea CO_2 exchange in the Ross Sea, Antarctica. *Journal of Geophysical Research: Oceans*, 122, 8167–8181. https://doi.org/10.1002/2017JC012853

Duprat, L., Kanna, N., Janssens, J., Roukaerts, A., Deman, F., Townsend, A. T. (2019). Enhanced Iron Flux to Antarctic Sea Ice via Dust Deposition From Ice-Free Coastal Areas. *Journal of Geophysical Research: Oceans*, 124, 8538−8557. https://doi.org/10.1029/2019JC015221

Fripiat, F., Meiners, K. M., Vancoppenolle, M., Papadimitrio, S., Thomas, D.N., et al. (2017). Macro-nutrient concentrations in Antarctic pack ice: Overall patterns and overlooked processes. *Elementa Science of Anthropocene*, 5−13. https://doi.org/10.1525/elementa.217

Hirano, D., Mizobata, K., Sasaki, H., Murase, H., Tamura, T., Aoki, S. (2021). Poleward eddy-induced warm water transport across a shelf break off Totten Ice Shelf, East Antarctica. *Communications Earth & Environment*, 2, 153. https://doi.org/10.1038/s43247-021-00217-4

Hirawake, T., Takao, S., Suzuki, K., Nishioka, J., Watanabe, Y. W., Isada, T. (2017). Estimation of ocean primary production from satellite remote sensing. *Oceanography in Japan*, 2017, 26, 3, 65−77. https://doi.org/10.5928/kaiyou.26.3_65

Iida, T., Odate, T., Fukuchi, M. (2013). Long-Term Trends of Nutrients and Apparent Oxygen Utilization South of the Polar Front in Southern Ocean Intermediate Water from 1965 to 2008. *PLoS ONE* 8, 8, e71766. https://doi.org/10.1371/journal.pone.0071766

JGOFS (1994). Protocols for the Joint Global Ocean Flux Study core measurements. *International JGOFS Report Series*, 19. http://hdl.handle.net/11329/220

Kamatani, A. and Ueno, Y. (1980). Regeneration Rate and Extent of Phosphorus and Silicon from Decomposing Phytoplankton Assemblages. *Bulletin of Japanese Society of Scientific Fisheries*, 46, 5, 537−542. https://doi.org/10.2331/suisan.46.537

Key, R.M., Olsen, A., Heuven, S., Lauvset, S. K., Velo, A., et al. (2015). Global Ocean Data Analysis Project, Version 2 (GLODAPv2), ORNL/CDIAC-162, NDP-093. Carbon Dioxide

Information Analysis Center, Oak Ridge National Laboratory, US Department of Energy, Oak Ridge, Tennessee. doi:10.3334/CDIAC/OTG.NDP093_GLODAPv2

Lannuzel, D., Schoemann, V., de Jong, J., Chou, L., Delille, B., Becquevort, S., Tison, J. L. (2008). Iron study during a time series in the western Weddell pack ice. *Marine Chemistry*, 108, 1-2, 85−95. https://doi.org/10.1016/j.marchem.2007.10.006

Martin, J.H., Fitzwater, S.E. Gordon, R.M. (1990). Iron deficiency limits phytoplankton growth in Antarctic waters. *Global Biogeochem Cycles* 4, 5−12. https://doi.org/10.1029/GB004i001p00005

Matsuno, K, Sumiya, K, Tozawa, M, Nomura, D, Sasaki, H, Yamaguchi, A, Murase, H. (2023). Responses of diatom assemblages and life cycle to sea ice variation in the eastern Indian sector of the Southern Ocean during austral summer 2018/2019. *Progress in Oceanography,* Volume 218, 103117, ISSN 0079-6611. https://doi.org/10.1016/j.pocean.2023.103117.

Matsuoka, K., Watanabe, T., Ichii, T., Shimada, H., Nishiwaki, S. (2003). Large whale distributions (south of 60ºS, 35ºE−130ºE) in relation to the southern boundary of the Antarctic Circumpolar Current. In A.H.L. Huiskes, W.W.C. Gieskes, J. Rozema, R.M.L. Schorno, S.M. van der Vies, W.J. Wolff (Eds.), Antarctic Biology in a Global Context. Leiden: Backhuys Publishers.

McCormack, S.A., Melbourne-Thomas, J., Trebilco, R., Blanchard, J.L., Constable, A. (2020). Alternative energy pathways in Southern Ocean food webs: Insights from a balanced model of Prydz Bay, Antarctica. *Deep Sea Research Part II: Topical Studies in Oceanography*, 174. 10.1016/j.dsr2.2019.07.001

Morel, A. and Berthon, J.F. (1989). Surface pigments, algal biomass profiles, and potential production of the euphotic layer: Relationships reinvestigated in view of remote-sensing applications. *Limnology and Oceanography*, 34, 1545−1562. https://doi.org/10.4319/lo.1989.34.8.1545

Mori, M., Mizobata, K., Ichii, T., Ziegler, P., Okuda, T. (2022). Modeling the egg and larval transport pathways of the Antarctic toothfish (*Dissostichus mawsoni*) in the East Antarctic region: New insights into successful transport connections. *Fisheries Oceanography*, 31, 1, 19−39. https://doi.org/10.1111/fog.12560

Nicol, S., and Raymond, B. (2012). Pelagic Ecosystems in the Waters off East Antarctica (30˚E−150˚E). Antarctic Ecosystems: An Extreme Environment in a Changing World. (eds Rogers, A. D., Johnston, N. M., Murphy, E. J. & Clarke, A.) Ch. 8, 243−254 (Blackwell Publishing Ltd., 2012). https://doi.org/10.1002/9781444347241.ch8

Nissen, C., Gruber, N., Münnich, M., Vogt, M. (2021). Southern Ocean phytoplankton community structure as a gatekeeper for global nutrient biogeochemistry. *Global Biogeochemical Cycles*, 35, e2021GB006991. https://doi.org/10.1029/2021GB006991

Nomura, D., Sahashi, R., Takahashi, D. K., Makabe, R., Ito, M., et al. (2023). Biogeochemical characteristics of brash sea ice and icebergs during the summer and autumn in the Indian sector of the Southern Ocean. *Progress in Oceanography*, Volume 214, 103023, ISSN 0079-6611. https://doi.org/10.1016/j.pocean.2023.103023

Olsen, A., Key, R. M., Heuven, S., Lauvset, S. K., Velo, A., et al. (2016). The Global Ocean Data Analysis Project version 2 (GLODAPv2) – an internally consistent data product for the world ocean, Earth Syst. Sci. Data, 8, 297–323, 2016. doi:10.5194/essd-8-297-2016

Orsi, A. H., Whitworth, T., Nowlin, W. D. (1995). On the meridional extent and fronts of the Antarctic Circumpolar Current. *Deep Sea Research Part I: Oceanographic Research Papers*, 42, 5, 641−673. https://doi.org/10.1016/0967-0637(95)00021-W

Pollard, R., Tréguer, P., Read, J. F. (2006). Quantifying nutrient supply to the Southern Ocean. *J. Geophys. Res.*, 111, C05011. doi:10.1029/2005JC003076

Pondaven, P., Ragueneau, O., Tréguer, P., Hauvespre, A., Dezileau, L., Reyss, J. L. (2000). Resolving the “opal paradox” in the Southern Ocean. *Nature*, 405, 168−172. https://doi.org/10.1038/35012046

Popova, E. E., Yool, A., Coward, A. C., Aksenov, Y. K., Alderson, S. G., Cuevas, B. A., Anderson, T. R. (2010). Control of primary production in the Arctic by nutrients and light: Insights from a high resolution ocean general circulation model. *Biogeosciences*, 7, 11, 3569−3591. doi:10.5194/bg-7-3569-2010

Prézelin, B. B., Hofmann, E. E., Klinck, J. M., Mengelt, C. (2000). The linkage between Upper Circumpolar Deep Water (UCDW) and phytoplankton assemblages on the west Antarctic Peninsula continental shelf. *Journal of Marine Research*, 58, 2, 165−202(38). https://doi.org/10.1357/002224000321511133

Pruvost, P., Duhamel, G., Palomares, M.L.D. (2005). An ecosystem model of the Kerguelen Islands' EEZ. In: Palomares, M.L.D., Pruvost, P., Pitcher, T.J., Pauly, D. (Eds.), Modeling Antarctic Marine Ecosystems, 13. Fisheries Centre Research Reports, 40−64.

Roden, N. P., Tilbrook, B., Trull, T. W., Virtue, P., Williams, G. D. (2016). Carbon cycling dynamics in the seasonal sea-ice zone of East Antarctica. *Journal of Geophysical Research: Oceans*, 121, 8749−8769. https://doi.org/10.1002/2016jc012008

Sahashi, R., Nomura, D., Toyota, T., Tozawa, M., Ito, M., et al. (2022). Effects of snow and remineralization processes on nutrient distributions in multi-year Antarctic landfast sea ice. *Journal of Geophysical Research-Oceans*, 127, e2021JC018371. https://doi.org/10.1029/2021JC018371

Sakshaug, E. (2004). Primary and secondary production in the Arctic Seas, in The Organic Carbon Cycle in the Arctic Ocean. edited by R. Stein and R. MacDonald, 57−81, Springer, Berlin Heidelberg.

Shadwick, E. H., Tilbrool, B., Williams, G. D. (2014). Carbonate chemistry in the Mertz Polynya (East Antarctica): Biological and physical modification of dense water outflows and the export of anthropogenic CO_2. *Journal of Geophysical Research: Oceans*, 119, 1, 1−14. https://doi.org/10.1002/2013JC009286

Siegelman, L., O'toole, M., Flexas, M., Rivière, P., Klein, P. (2019). Submesoscale ocean fronts act as biological hotspot for southern elephant seal. *Scientific reports*, 9,1, 1−13. https://doi.org/10.1038/s41598-019-42117-w

Sokolov, S. and Rintoul, S. R. (2007). On the relationship between fronts of the Antarctic Circumpolar Current and surface chlorophyll concentrations in the Southern Ocean. *Journal of Geophysical Research: Oceans*, 112(C7). https://doi.org/10.1029/2006JC004072

Takahashi, T., Sweeney, C., Hales, B., Chipman, D. W., Newberger, T., Goddard, J. G., Iannuzzi, R. A., Sutherland, S. C. (2012). The changing carbon cycle in the Southern Ocean. *Oceanography*, 25, 26−37. https://doi.org/10.5670/oceanog.2012.71

Tamura, T. P., Nomura, D., Hirano, D., Tamura, T., Kiuchi, M., et al. (2022). Impacts of basal melting of the Totten Ice Shelf and biological productivity on marine biogeochemical components in Sabrina Coast, East Antarctica. *Global Biogeochemical Cycles*, 36, e2022GB007510. https://doi.org/10.1029/2022GB007510

Thorpe, S.E., Murphy, E.J., Watkins, J.L. (2007). Circumpolar connections between Antarctic krill (*Euphausia superba* Dana) populations: Investigating the roles of ocean and sea ice transport. *Deep Sea Research Part I: Oceanographic Research Papers*, 54, 5, 792−810. https://doi.org/10.1016/j.dsr.2007.01.008

Tomczak, M., and Liefrink, S. (2005). Interannual variations of water mass volumes in the Southern Ocean. *Journal of Atmospheric and Ocean Scienc*e, 10, 31−42. https://doi.org/10.1080/17417530500062838

Tozawa, M., Nomura, D., Nakaoka, S., Kiuchi, M., Yamazaki, K., Hirano, D., Aoki, S., Sasaki, H., Murase, H. (2022). Seasonal variations and drivers of surface ocean pCO_2 in the seasonal ice zone of the eastern Indian sector, Southern Ocean. *Journal of Geophysical Research: Ocean*, 127, e2021JC017953. https://doi.org/10.1029/2021JC017953

Tozawa, M., Nomura, D., Yamazaki, K., Kiuchi, M., Hirano, D., Aoki, S., Sasaki, H., Murase, H. (2024a). Oceanographic factors determining the distribution of nutrients and primary production in the subpolar Southern Ocean. *Progress in Oceanography*, Volume 225, 103266. https://doi.org/10.1016/j.pocean.2024.103266

Tynan, C. T. (1998). Ecological importance of the southern boundary of the Antarctic Circumpolar Current. *Nature*, 392, 6677, 708−710. https://doi.org/10.1038/33675

Whitworth, T., Orsi, A. H., Kim, S.-J., Nowlin, W. D., Locarnini, R. A. (1998). Water masses and mixing near the Antarctic slope front. In Ocean, Ice, and Atmosphere: Interactions at the Antarctic Continental Margin. *Antarctic Research Series*, 75, 1−27. https://doi.org/10.1029/ AR075p0001

Yamazaki, K., Aoki, S., Shimada, K., Kobayashi, T., Kitade, Y. (2020). Structure of the subpolar gyre in the Australian−Antarctic Basin derived from Argo floats. *Journal of Geophysical Research: Oceans*, 125(8), e2019JC015406. https://doi.org/10.1029/2019JC015406

Yamazaki, K., Aoki, S., Katsumata, K., Hirano, D., Nakayama, Y. (2021). Multidecadal poleward shift of the southern boundary of the Antarctic circumpolar Current off east Antarctica. *Science Advances*, 7, eabf8755. https://doi.org/10.1126/ sciadv.abf8755

Yamazaki, K., Katsumata, K., Hirano, D., Nomura, D., Sasaki, H., et al. (2024). Revisiting the circulation and water masses over the East Antarctic margin (80−150˚E). *Progress in Oceanography*, 225, 103285. https://doi.org/10.1016/j.pocean.2024.103285

Figures and Table

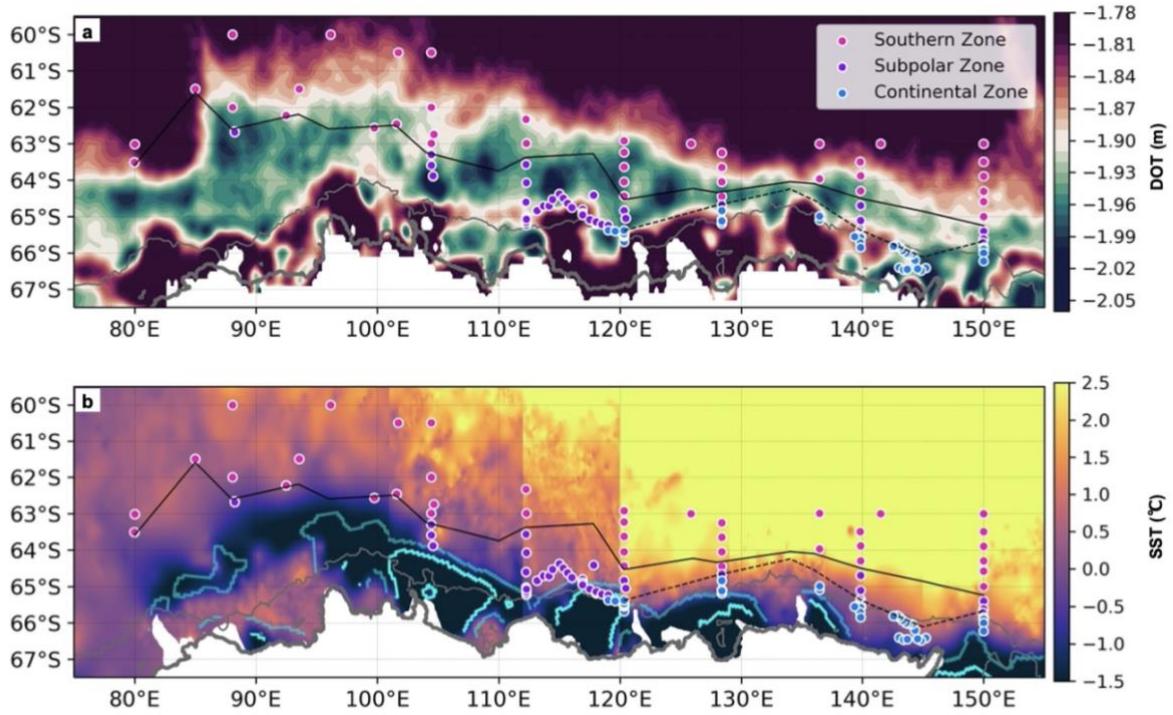

Figure 3.1. Physical and biogeochemical conditions in the study region. (a) Dynamic ocean topography (DOT) in January 2019 (color scale); mean flow directions were inferred to be clockwise around DOT minima. (b) Sea surface temperature (SST) obtained from satellite observations (color scale) (composited data over the week of observation). Hydrographic stations during the KY1804 survey are colored according to the frontal zones in which they are located. The solid line indicates the Southern Boundary (SB), and the dashed line indicates the Antarctic Slope Front (ASF). In each panel, coastline and the 1000 m isobath are indicated by thick and thin gray lines, respectively. In (b), thin cyan contours denote a sea ice concentration of 40% and thick contours indicate a sea ice concentration of 80%.

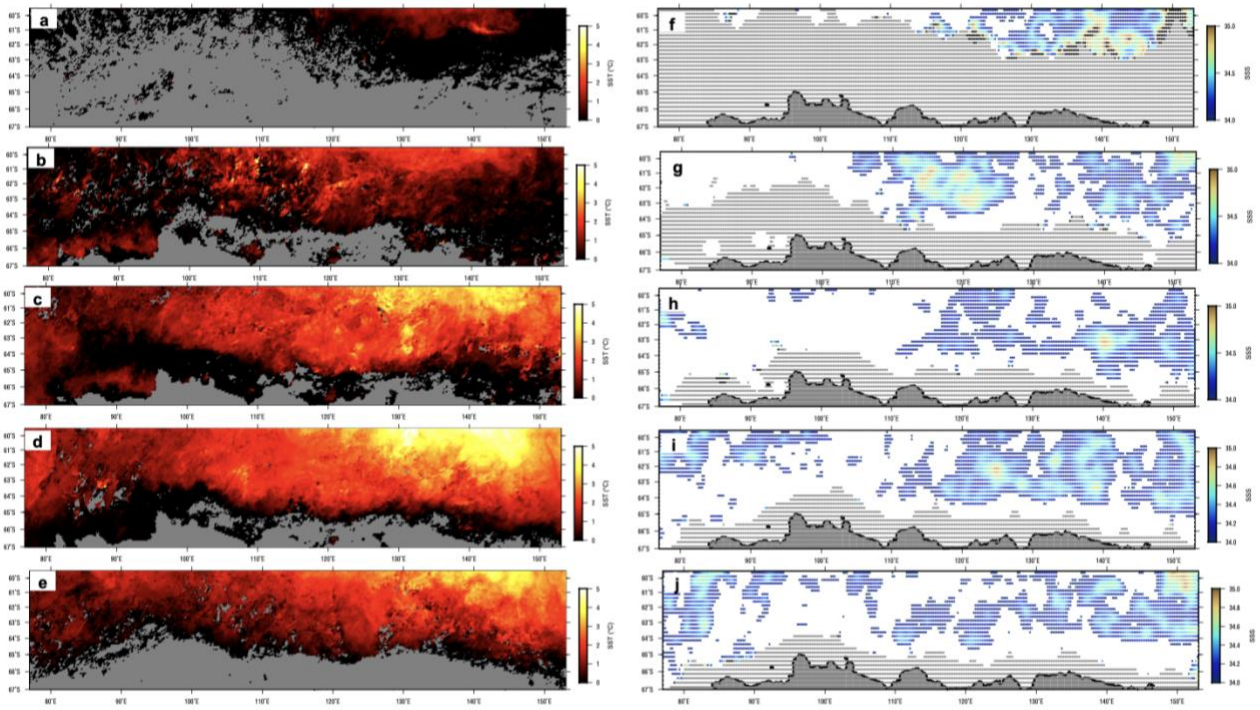

Figure 3.2. Satellite images of (a–e) SST and (f–j) sea surface salinity from November to March, respectively.

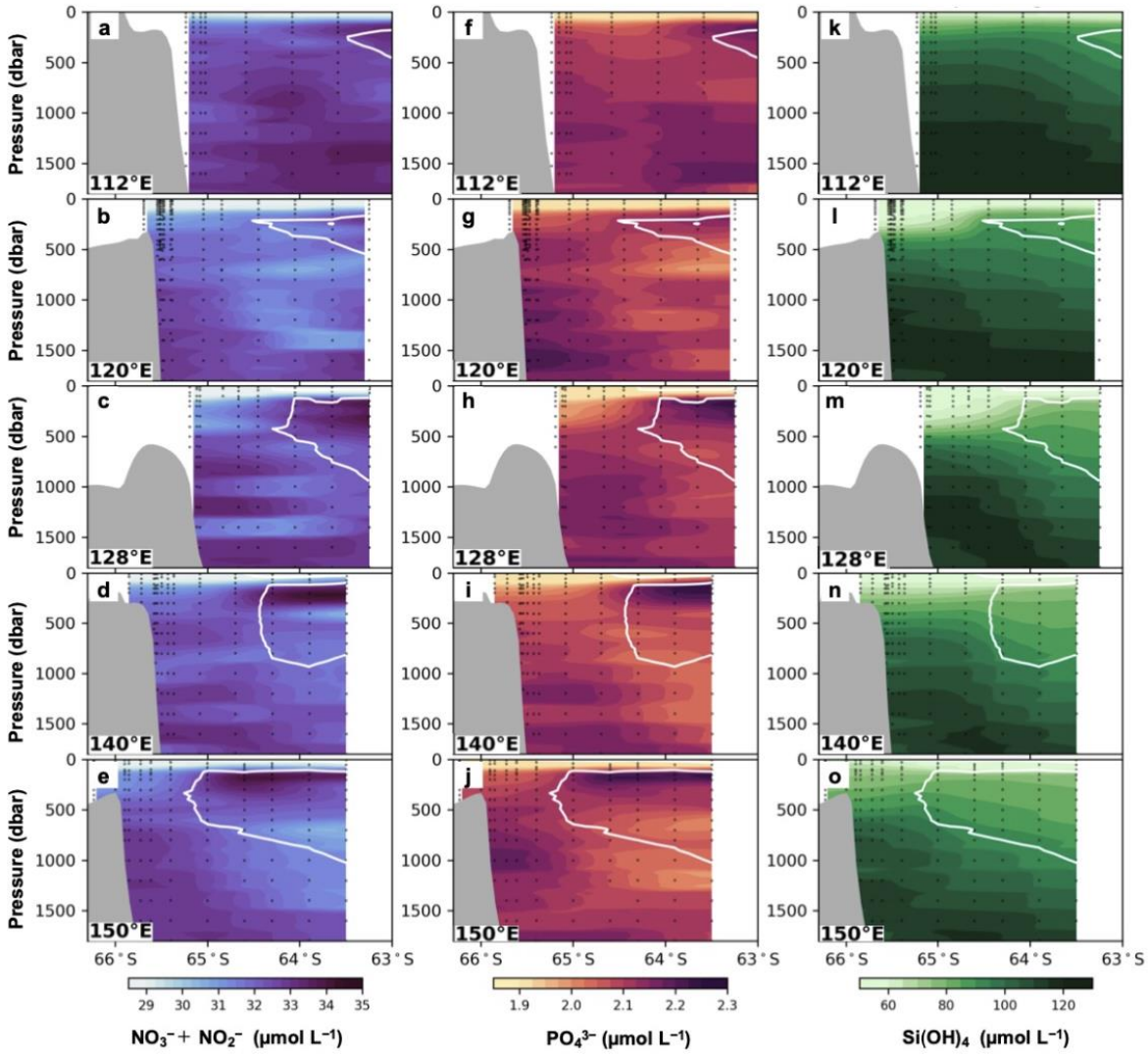

Figure 3.3. Meridional sections along 112, 120, 128, 140, and 150˚E of nutrient concentrations: (a–e) NO_3^-+NO_2^-, (f–j) PO_4^{3-}, and (k–o) $Si(OH)_4$). The white contours denote the 1.5˚C isotherm as a proxy for the warm core of Circumpolar Deep Water. Black dots show where bottle data were obtained.

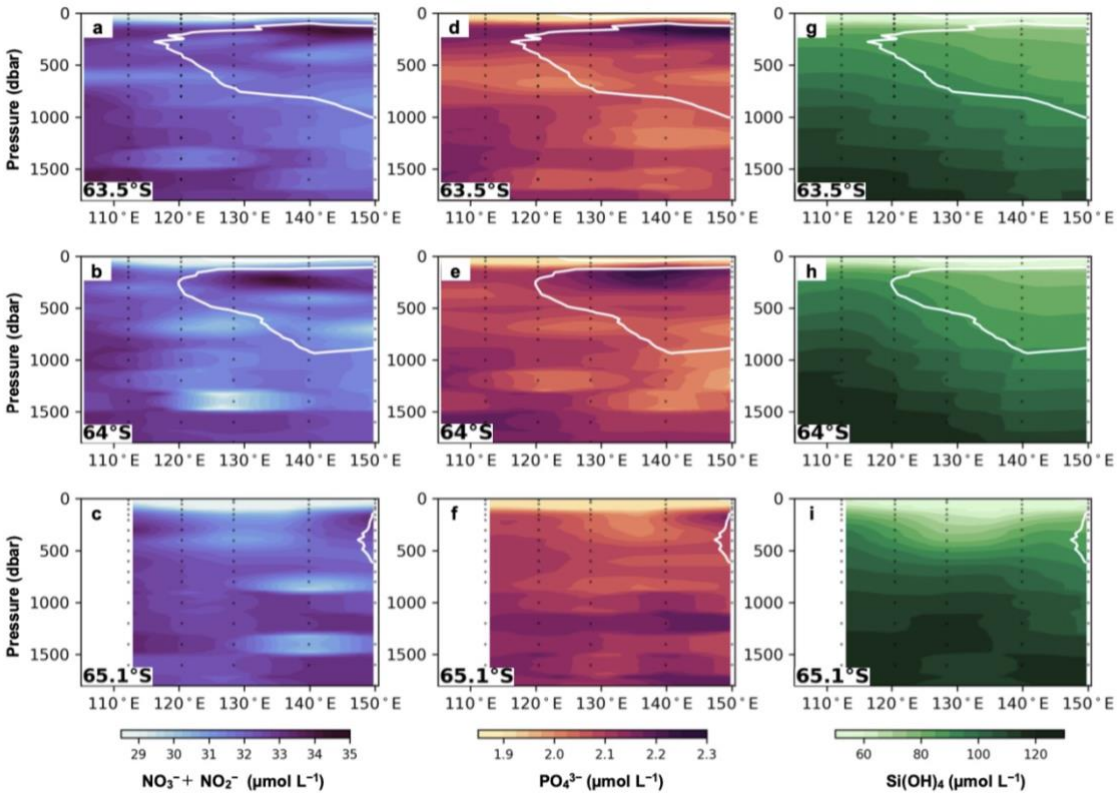

Figure 3.4. Same as Figure 3.2, but for zonal sections along 63.5, 64, and 65.1˚S.

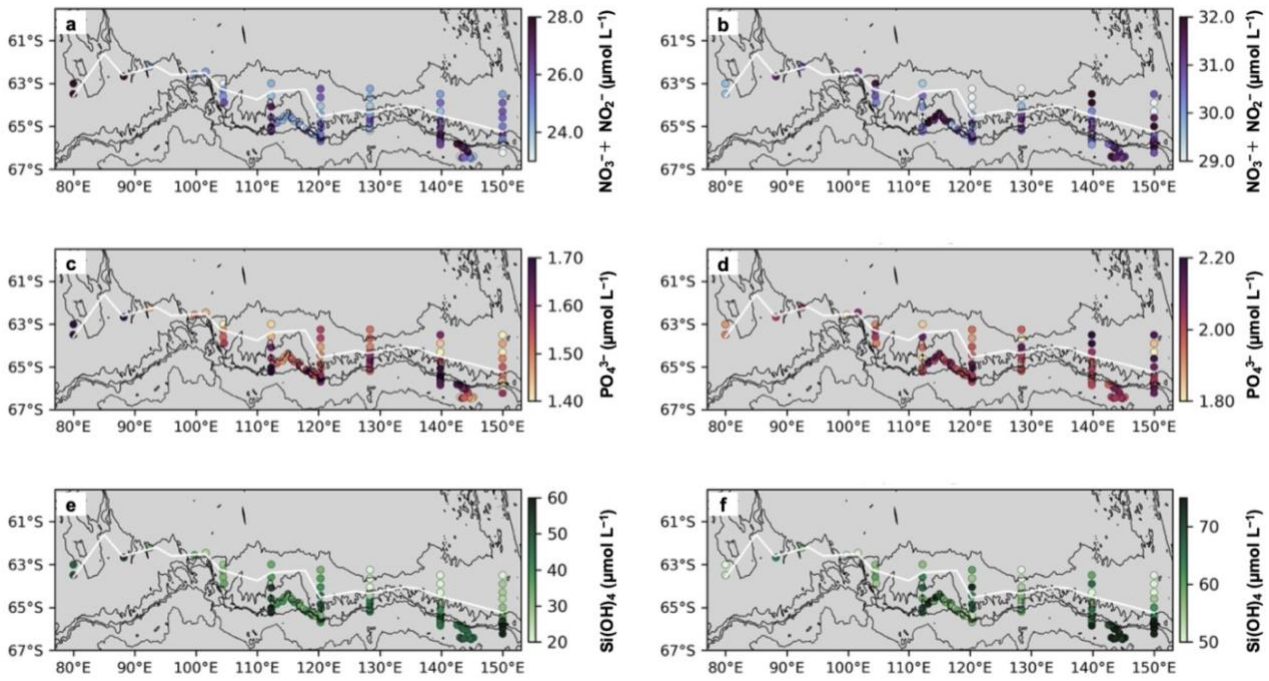

Figure 3.5. Horizontal distribution maps of (a, b) NO_3^-+NO_2^-, (c, d) PO_4^{3-}, and (e, f) $Si(OH)_4$ at 10 m and T-min, respectively. Contours show the bathymetry (interval, 1,000 m).

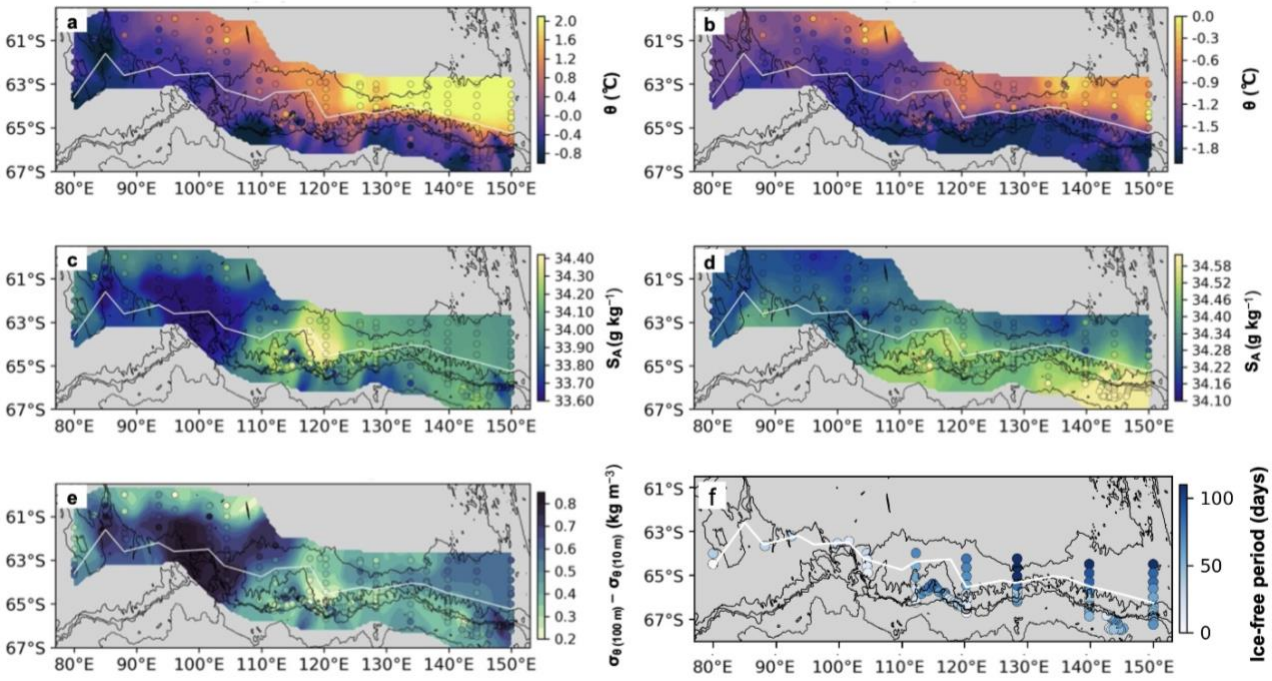

Figure 3.6. Horizontal distribution maps of (a, b) temperature and (c, d) salinity at 10 m depth and T-min, respectively and of (e) the density difference between 10 m and 100 m and, (f) ice-free period. Circle colors indicate the data at each station, and the background colors show spatially interpolated data. The white line denotes the SB. Contours show the bathymetry (interval, 1,000 m).

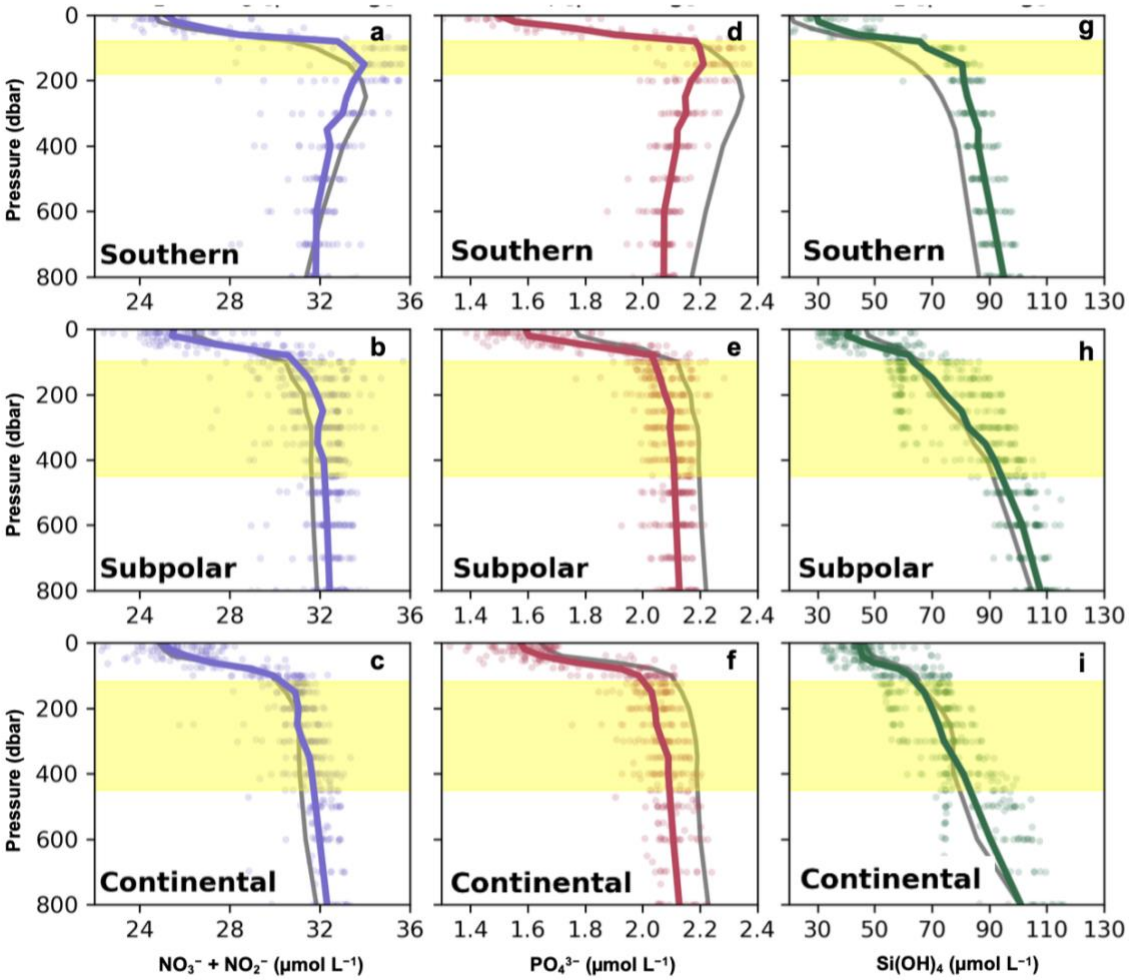

Figure 3.7. Vertical profiles of nutrients (NO_3^-+NO_2^-, PO_4^{3-}, and $Si(OH)_4$) averaged over (a, d, g) Southern, (b, e, h) Subpolar, and (c, f, i) Continental frontal zones. The colored dots represent individual bottle data. Yellow layers indicate the inverse layers.

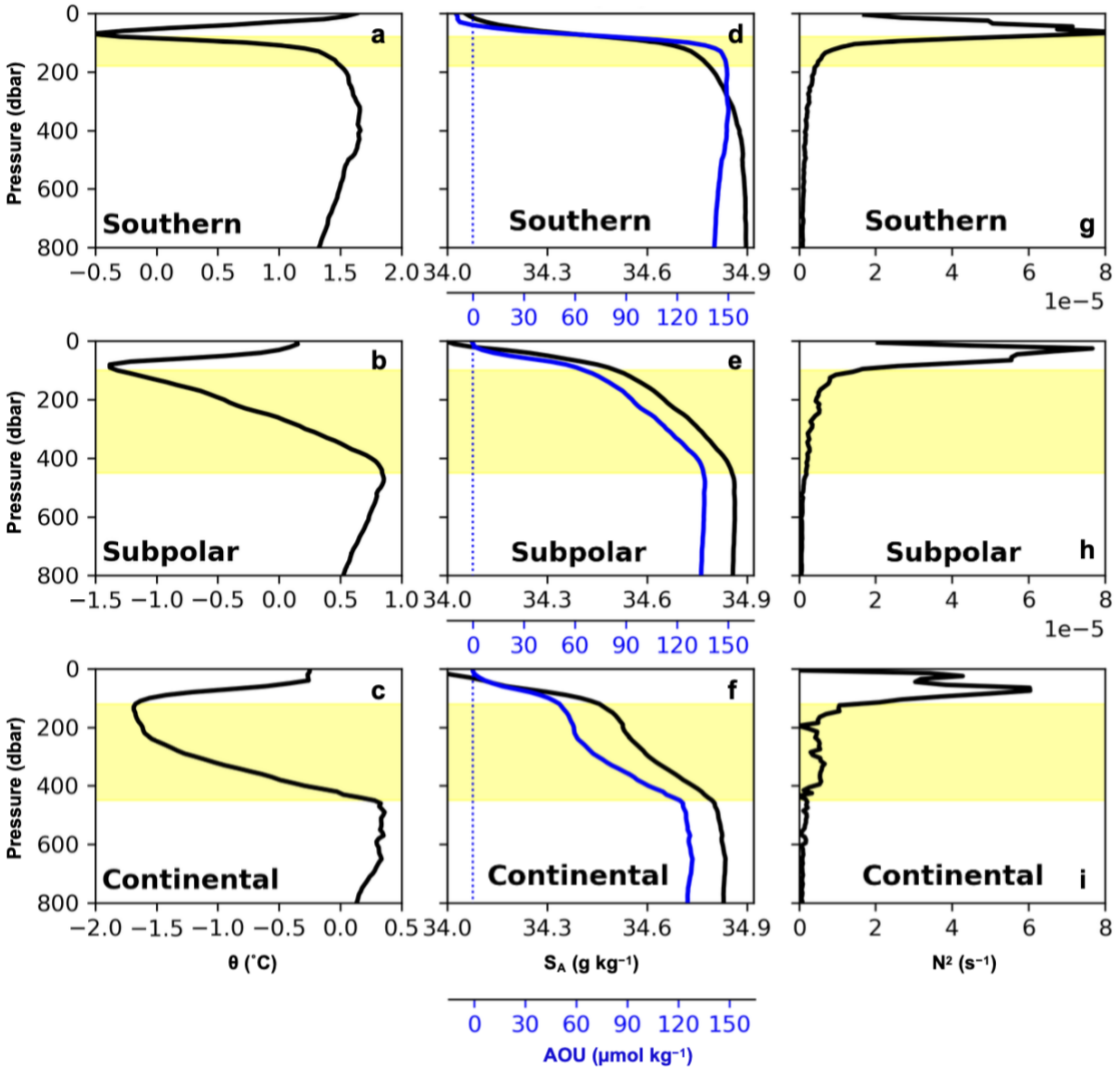

Figure 3.8. Vertical profiles of physical variables averaged over (a, d, g) Southern, (b, e, h) Subpolar, and (c, f, i) Continental frontal zones: conservative temperature (θ), absolute salinity (S_A), dissolved oxygen, and N^2 (buoyancy frequency). Colored dots represent individual bottle data. Gray lines indicate the distributions of nutrients in 2018 obtained from GLODAPv2. Yellow layers indicate the inverse layers.

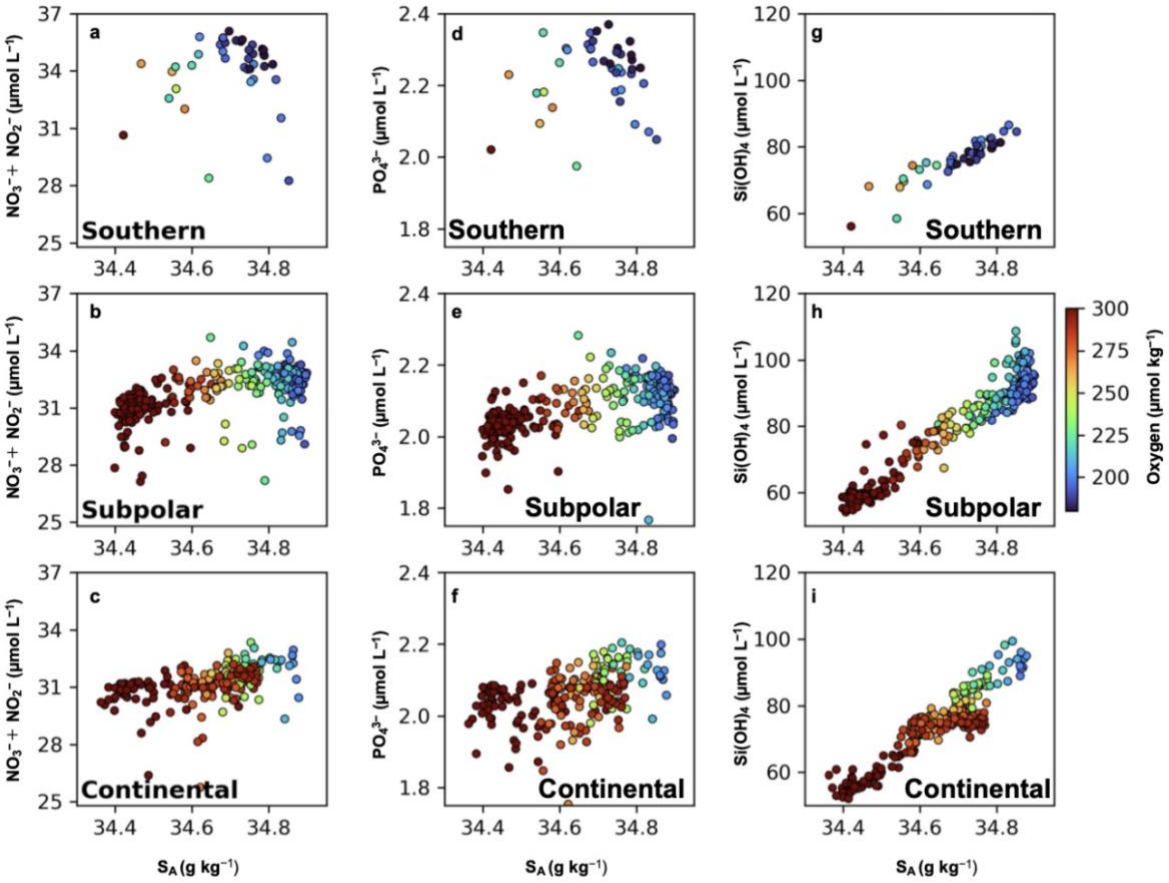

Figure 3.9. Scatter plots of absolute salinity (S_A) versus nutrients in the inverse layer in (a, d, g) Southern, (b, e, h) Subpolar, and (c, f, i) Continental frontal zones. The symbol colors indicate the oxygen content.

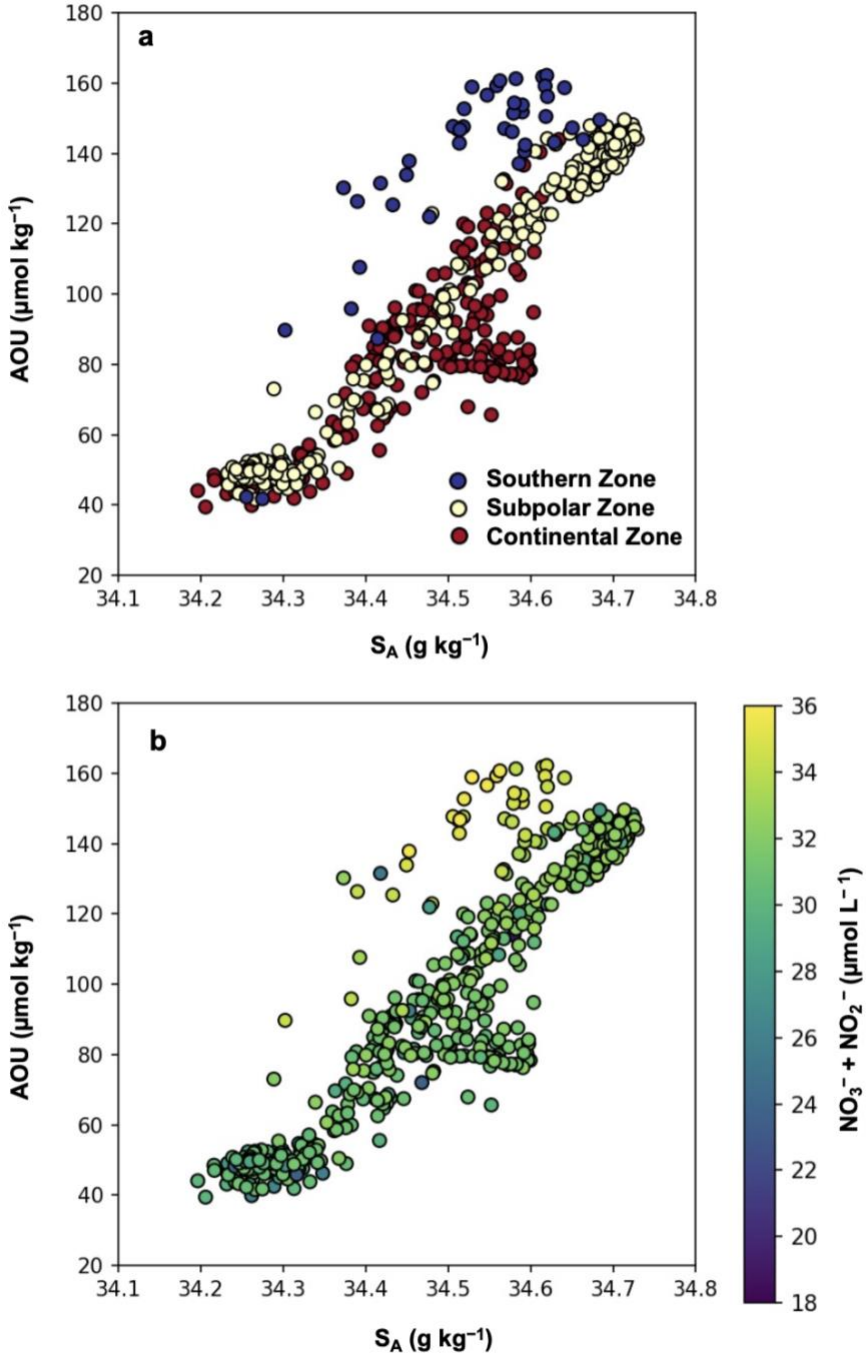

Figure 3.10. Scatter plots of absolute salinity (S_A) versus AOU in the inverse layer. Symbol colors in (a) indicate the frontal zone and in (b) the NO_3^-+NO_2^- concentration.

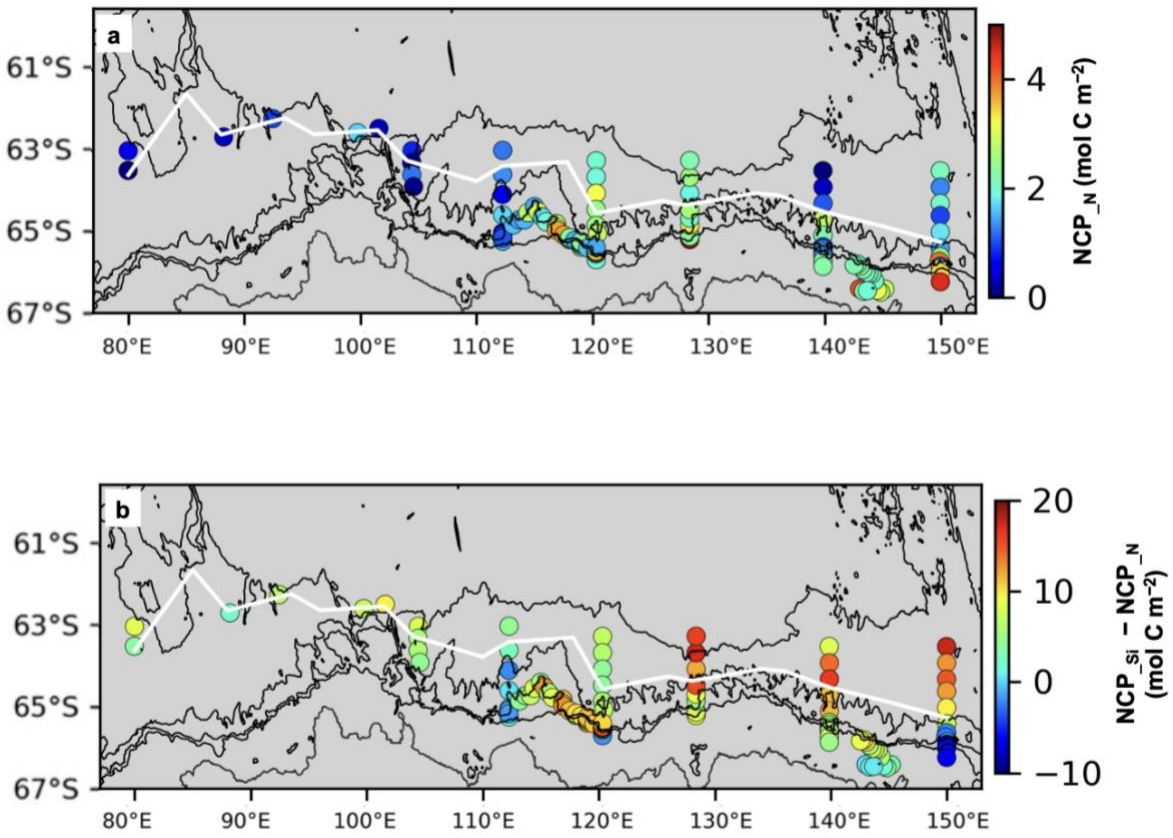

Figure 3.11. (a) $NCP_{\_N}$ calculated by using in situ nitrate concentration, (b) Difference between $NCP_{\_N}$ and $NCP_{\_Si}$ (NCP calculated by using in situ silicate concentration).

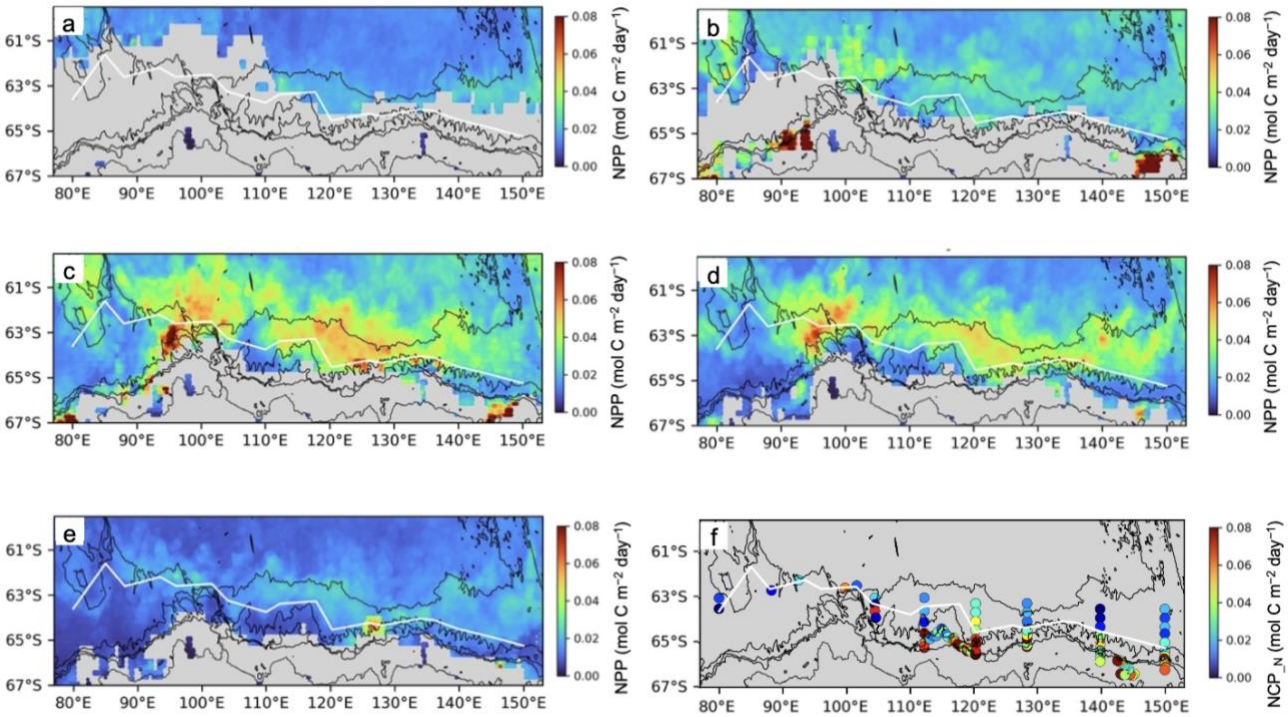

Figure 3.12. (a–e) NPP calculated by using satellite chlorophyll-*a* data from November to March, respectively, (f) NCP per day at observation stations calculated by using in situ nutrient concentrations.

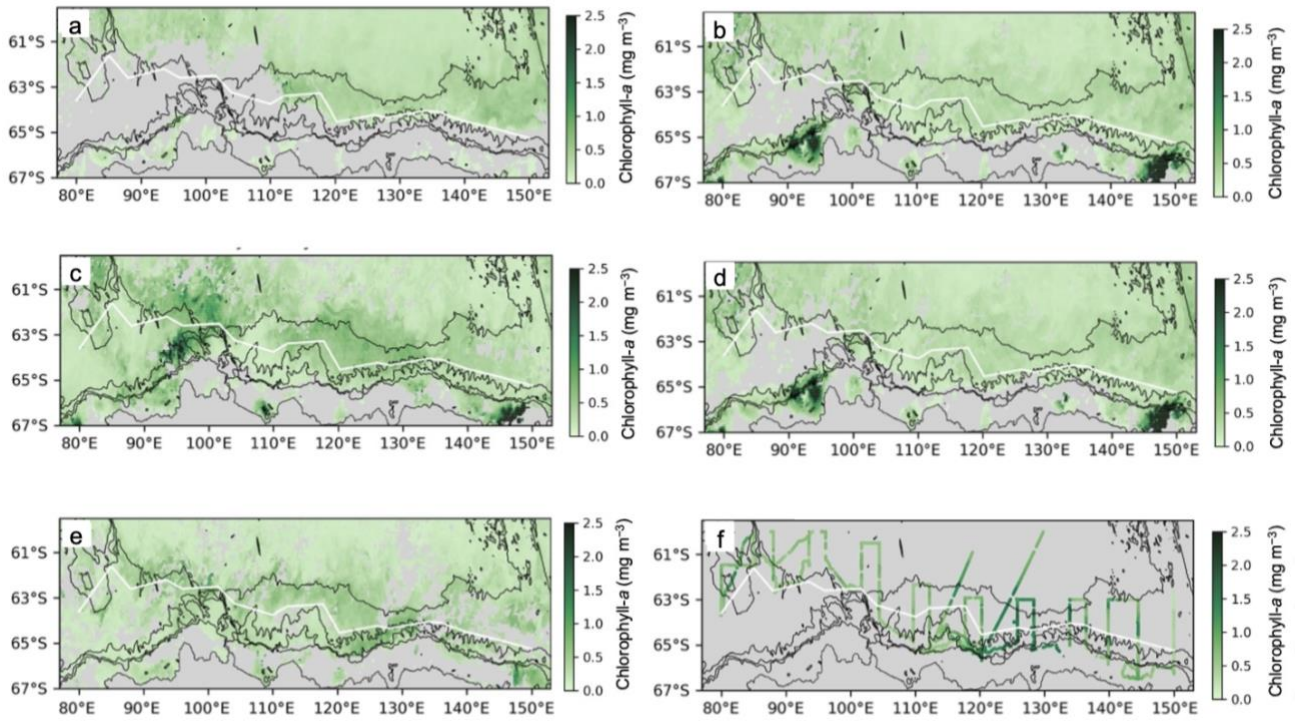

Figure 3.13. (a–e) Satellite-based chlorophyll-*a* distributions from November to March, respectively, (f) Chlorophyll-*a* measured underway during the observation period.

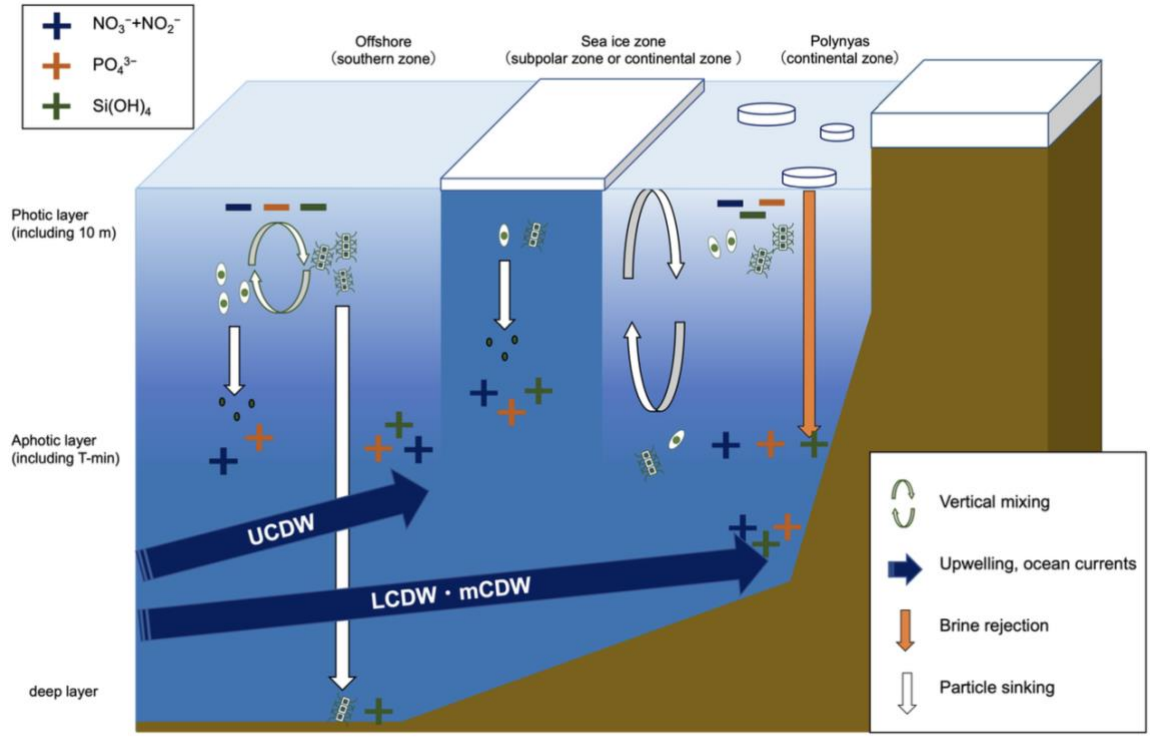

Figure 3.14. Schematic diagram of nutrient concentration changes from winter to summer in the eastern Indian Ocean sector of the Southern Ocean. UCDW, LCDW, mCDW, and ACC mean Upper Circumpolar Deep Water (CDW), Lower CDW, modified CDW, and Antarcitic Circumpolar Current, respectively.

4. Quantitative Assessment of Factors Contributing to Variations in Sea Surface pCO_2 in the Pacific Sector of the Arctic Ocean

Abstract

To quantitatively assess seasonal variations in the partial pressure of carbon dioxide (pCO_2) in the Pacific sector of the Arctic Ocean (Canada Basin and Chukchi Sea) in 2021, water temperature, salinity, chlorophyll-*a*, pCO_2, dissolved inorganic carbon (DIC), total alkalinity (TA), and nutrients were measured. During summer 2021, surface water pCO_2 in our study area (315 ± 41 µatm) was undersaturated with respect to the atmosphere (404 ± 4 µatm), and the ocean was a sink for atmospheric CO_2 (−10.5 ± 11.0 mmol C m^{-2} day^{-1}). Using DIC, TA, and nutrients in the temperature minimum layer, we estimated the under-ice pCO_2 in the water during the previous winter and calculated changes in pCO_2 (δpCO_2) due to temperature changes, freshwater inflow, biological activity, and other factors (gas exchange and advection) from winter to summer. In the Chukchi Sea, biological activity and temperature changes had significant impacts on pCO_2, whereas in the Canada Basin, the influx of freshwater caused a significant decrease in pCO_2. Our results suggested that different types of freshwaters had different effects on pCO_2, with sea ice meltwater having a greater effect on reducing pCO_2 than river water or snowmelt water. We therefore emphasize the importance of freshwater type and proportion, as well as freshwater supply, for prediction of future pCO_2 changes.

4.1. Introduction

The Arctic Ocean is one of the oceans most strongly affected by global warming. For example, temperature increases have been very pronounced; sea surface temperatures in the Arctic Ocean are rising nearly four times faster than the global average rate ≈ et al., 2022). Moreover, in September 2012, the smallest sea ice extent (3.4×10^6 km^2) since satellite sea ice observations began in 1978 was recorded (Parkinson & Comiso, 2013). Déry et al. (2016) have also reported that river water inflows from northern Canada have increased as a result of global warming.

These environmental changes have a significant impact on the biogeochemistry of ocean waters. A reduction in sea ice can stimulate primary production by improving the light environment (Arrigo et al., 2008). In contrast, increases in meltwater and enhanced stratification may limit the nutrient

supply (Zhuang et al., 2021). The Arctic Ocean is known to be a carbon dioxide (CO_2) sink (e.g., Bates & Mathis, 2009; Yasunaka et al., 2018, 2023). The amount of CO_2 exchanged between the atmosphere and the ocean is determined by the difference in the partial pressure of carbon dioxide (pCO_2) between the atmosphere and the ocean surface (Wanninkhof, 2013). Because atmospheric pCO_2 does not change substantially over short periods, changes in ocean pCO_2 essentially determine the direction of the CO_2 exchange. Sea surface pCO_2 depends on water temperature, freshwater inflow, and biological activity (e.g., Bates et al., 2006). Increases in water temperature and freshwater inflows associated with global warming and subsequent changes to the biogeochemical environment therefore play an important role in determining changes in oceanic CO_2 uptake and the global carbon cycle. However, studies aimed at assessing how much various factors change Arctic pCO_2 have been limited (e.g., Kosugi et al., 2017; Burgers et al., 2017). Most studies have been qualitative assessments of pCO_2 (e.g., Burgers et al., 2017) or quantitative assessments of changes in dissolved inorganic carbon (DIC) or total alkalinity (TA) (e.g., Jones et al., 2020); few studies have directly and quantitatively assessed the drivers of changes in pCO_2. To assess and predict the future impact of environmental changes on CO_2 absorption from the atmosphere to the Arctic Ocean, it is important to quantitatively assess the changes in pCO_2 and to clarify how environmental factors have influenced these changes.

The Pacific Sector of the Arctic Ocean consists of the Chukchi Sea, a shallow continental shelf area; the Canada Basin, a deep basin area; and the Beaufort Sea, a marginal sea facing Canada and Alaska (Figure 4.1). During the summer ice-melting season, low-salinity sea ice meltwater spreads over the Chukchi Sea, and Pacific Ocean water flows into the Chukchi Sea through the Bering Strait (e.g., Li et al., 2017). The meltwater is one of the sources of freshwater in the Arctic Ocean (e.g., Haine et al., 2015; Carmack et al., 2016). Furthermore, the Yukon River in Alaska and the Anadyr River in Siberia discharge directly into the Bering Shelf, and these waters are transported into the Chukchi Sea via the Alaskan Coastal Current (e.g., Li et al., 2017). The Chukchi Sea therefore receives large amounts of freshwater, and it is expected to be strongly affected by increases in the freshwater supply associated with global warming (e.g., Shu et al., 2018). Although the impact of sea ice melting on pCO_2 has been much discussed (e.g., Burgers et al., 2017), there are few detailed studies on the effects of river water on carbonate chemistry. For example, Yamamoto-Kawai et al. (2013) mentioned that river water affects the saturation state of calcium carbonate. Burgers et al. (2017) have reported that the sea surface pCO_2 in the Eastern Canadian Arctic Ocean is affected by freshwater inflows. In particular, they have shown that pCO_2 is lower in areas where the sea ice meltwater fraction is high and higher in areas where the river water signal is strong. However, their

assessment was qualitative; they did not quantitatively assess the impact of different freshwater sources on pCO_2.

In this study, we estimated winter-to-summer pCO_2 variations and quantified the driving factors by using observational data for the Pacific sector of the Arctic Ocean, especially the Chukchi Sea and Canada Basin, during the summer of 2021. This assessment of factors is based on methods described in Chapter 2. However, because the Arctic Ocean differs from the Southern Ocean in terms of both water depth and freshwater supply, their methods needed to be modified. In this study, we estimated changes in oceanic geochemical parameters from winter to summer using data from ship-based observations. Because freshwater volume as well as its composition will be important for the prediction of pCO_2 variations in the future, we estimated the origins of freshwater inputs (sea ice meltwater, snow meltwater, and river water) by using the stable oxygen isotopic ratio ($\delta^{18}O$) and concentration of colored dissolved organic matter (CDOM), and we examined the differences in the impacts of each type of freshwater input on pCO_2.

4.2. Materials and Methods

4.2.1. Underway Measurements and Surface Seawater Sampling

Sampling was conducted in the Pacific sector of the Arctic Ocean (north of 65˚N, 150−170˚W) in September−October 2021 (Figure 4.1a) during cruise MR21−05C of the R/V *Mirai* (Japan Agency for Marine-Earth Science and Technology; JAMSTEC).

During the cruise, surface seawater was pumped via an intake at a depth of ~4.5 m below the sea surface into an equilibrator at a flow rate of 4−5 L min^{-1}. Equilibrated air was circulated by the pump at a flow rate of 0.6−0.7 L min^{-1} through an electronic cooler (2˚C) and a Stirling cooler (−70˚C) and then analyzed by an integrated cavity output spectrometer (Off-Axis ICOS; 911−0011, Los Gatos Research, USA) at 1.5-min intervals. For calibration, three standard gases (240, 378, and 471 ppm) were also measured approximately once every 4 h. In addition, the pCO_2 of air was sampled from the bow of the ship (~13 m above the sea surface) and measured twice every ~3 h (air samples were also dehumidified with a Perma Pure dryer). Dissolved inorganic carbon (DIC) in surface seawater was also continuously measured by the coulometric titration method (Johnson et al., 1985; Johnson, 1992) using a DIC-measuring system (Nihon ANS, Inc., Japan) installed on the

R/V *Mirai*. The measuring method was the same as in Murata et al. (2022). In addition, at surface water sampling stations (Figure 4.1b), seawater samples pumped via the same intake used for pCO_2 measurements were collected (a) in 10-mL polyethylene screw-cap vials (Eiken Chemical Co., Ltd, Japan) for nutrient measurements (NO_3^-, NO_2^-, NH_4^+, PO_4^{3-}, $Si(OH)_4$), (b) in 15-mL glass screw-cap vials (Nichiden-Rika Glass Co. Ltd, Kobe, Japan) for $\delta^{18}O$ measurement, and (c) in 110-mL glass vials (Laboran Screw Tube Bottle, AS ONE, Tokyo, Japan) that had been acid-washed and combusted (450˚C, 4 h) for CDOM measurements. Samples for nutrient and $\delta^{18}O$ measurements were stored in a refrigerator at +4˚C. Samples for CDOM measurements (~300 ml) were filtered through a 0.2-μm Nuclepore filter (Whatman, 47 mm) within a few hours after sampling and then stored in a refrigerator.

Sea surface temperature and electrical conductivity (salinity) were measured with a thermosalinograph (SBE-45, Sea-Bird Electronics, Inc., USA) in the surface seawater analysis room. The temperature increase (~0.4˚C) due to pumping was corrected for by using measurements made by a thermometer on the bottom of the ship (SBE-38, Sea-Bird Electronics). Fluorescence was measured with a C3 submersible fluorometer (Turner Designs, Inc., USA), and dissolved oxygen was measured with a RINKO II ARO-CAR DO sensor (JFE Advantech, Inc., Japan). The accuracy of the sensors for temperature (SBE-45), conductivity (SBE-45), temperature on the bottom of the ship (SBE-38), and dissolved oxygen (RINKO II ARO-CAR) were 0.002˚C, 0.0003 S m^{-1}, 0.001˚C, and saturation ± 2% full scale, respectively.

4.2.2 Sampling at CTD Stations

Conductivity-temperature-depth (CTD) observations and vertical water column sampling were conducted at the stations shown in Figure 1c. Vertical water temperature and conductivity were measured with SBE03 and -04/F and SBE04C sensors calibrated prior to the cruise. Acid-cleaned 12-L Niskin bottles (Sea-Bird Electronics) were used for vertical seawater sampling, and seawater from the ocean surface was collected at the CTD stations using a bucket. The procedures used for sampling, processing, and storage were the same as those used for the underway sampling. Seawater samples for fluorescence were collected in Nalgene polyethylene bottles. Seawater samples for DIC measurement were collected in 250-mL glass bottles (SCHOTT DURAN®, Schott AG, Germany). For collecting DIC samples, silicone rubber tubes with perfluoroalkoxy tips were connected to the Niskin bottle outlet. The bottle was gently filled with water from the bottom until

it overflowed for 20 s to eliminate air bubbles (Dickson et al., 2007). Immediately after the sampling, the bottles with the DIC water samples were transported to the laboratory onboard the R/V *Mirai*, where 100 µL of a saturated solution of mercuric chloride ($HgCl_2$) was added. They were then sealed with polyethylene inner lids with a diameter of 31.9 mm and stored in a refrigerator at approximately +5˚C until analysis on board within 24 h. Seawater samples for TA were collected in 125-mL glass bottles (SCHOTT DURAN®, Schott AG, Germany). Nutrient samples were similarly stored in the refrigerator. Samples for chlorophyll-*a* analysis were vacuum-filtered (<0.02 MPa) in the dark through a 25-mm Advantec GF75 filter. The filters were immediately soaked in 7 mL of *N*,*N*-dimethylformamide (DMF, Wako Pure Chemical Industries Ltd., Japan) in a polypropylene tube (Suzuki & Ishimaru, 1990). The tubes were stored at −20˚C for at least 24 h to extract the chlorophyll-*a*.

4.2.3. Sea Ice and Snow Sampling

Sea ice samples were collected at three sites (Figure 4.1b, blue triangles). We collected less than 1 m^3 of sea ice in a wire mesh pallet cage (1.2 m × 1.0 m × 0.9 m) connected to a crane on board. Immediately after the sampling, temperatures outside and inside the sea ice were measured with a needle-type temperature sensor (Testo 110 NTC, Brandt Instruments, Inc., USA). Snow samples were also collected immediately after a snowfall on 17−21 September by snow sampling boards on the deck. The sea ice samples were cut into 0.15 m × 0.15 m × 0.15 m pieces, which were allowed to melt in gas-tight bags (AAK10, GL Science, Japan) in a cool, dark room. Snow samples were packed in Ziploc-type bags and then allowed to melt in a cool, dark room. The salinity of the melted samples was measured with an electrical conductivity sensor (Cond 315i, WTW, Germany). Meltwater from the sea ice samples was sampled for measurement of DIC, TA, nutrients, and $\delta^{18}O$. The collected snow meltwater samples were measured only for $\delta^{18}O$.

4.2.4. Onboard Sample Analysis

The seawater and meltwater samples for DIC and seawater samples for TA were measured onboard. The samples for DIC measurement were taken from the refrigerator about 1 h before analysis and held in a water bath at ~20˚C to maintain them at a constant temperature. The samples were analyzed within 24 h after sampling. For DIC measurements, a total CO_2 measuring system (Nihon

Ans Inc., Japan) was used. The system comprised a seawater dispensing unit, a CO_2 extraction unit, and a coulometer (Model 3000A, Nihon Ans Inc.). In the seawater dispensing unit, seawater was dispensed into a 15-mL measuring pipette by an autosampler and maintained at 20.00 ± 0.05˚C. The CO_2 was extracted by adding a 10% phosphoric acid solution. The extracted CO_2 was carried to the coulometer by nitrogen gas (flow rate 140 mL min−1) through two electric dehumidifiers (2˚C) containing magnesium perchlorate as a desiccant. A CO_2 standard gas of about 1.5% in a nitrogen base, a phosphoric acid blank, and the seawater sample were measured repeatedly, and the standard gas and blank signals were used to correct for signal drift caused by chemical changes of the coulometer solution. The solutions were prepared every two days, and 10 bottles of KANSO TECHNOS reference material were measured (batch AV; 2043.6 ± 1.0 μmol kg−1, average measured value 2041 ± 1.0 μmol kg−1) traceable to the Certified Reference Material distributed by Prof. A. G. Dickson (Scripps Institution of Oceanography, La Jolla, CA, USA). An adjustment was applied to the measured value to remove this average measured difference. The relative standard deviation of the count values from repeated standard gas measurements was less than 0.05% (n = 5), and the mean and standard deviation of the measured differences for replicate samples was 1.62 ± 1.60 μmol kg−1 (n = 53).

Total alkalinity was measured using a spectrophotometric system (Nihon ANS Inc.). The samples for TA were transferred via a dispensing device (~42 mL) kept at 25.0˚C to a titration cell with a light path length of 4 cm. The TA was calculated by measuring two sets of absorbances at three wavelengths (730, 616, and 444 nm) with a spectrometer (TM UV/VIS C10082CAH, Hamamatsu photonics, Japan). One set was the absorbance of the seawater sample (blank) before the injection of an acid with an indicator solution (bromocresol green sodium), and the other was the absorbance of the seawater after the injection. The mixed solution was circulated in a circulation line by a peristaltic pump for 5 min to sufficiently mix the acidified indicator solution with the seawater. Nitrogen bubbles were introduced into the titration cell to thoroughly degas CO_2 from the mixed solution. From these absorbances, the absorbance ratio (R) was calculated as $R = (A_{616} - A_{730})/(A_{444} - A_{730})$, where A_i is the absorbance of seawater mixed with acid titrant at wavelength i (nm) after subtracting the absorbance of the seawater blank. Then pH on the total hydrogen ion scale $[H^+]_T$ was calculated from A_i and salinity following Yao and Byrne (1998). TA was finally obtained from $TA = ([H^+]_T V_{SA} + M_A V_A)/V_S$, where V_S, V_A, and V_{SA} are the initial seawater volume, the added acid titrant volume, and the combined seawater plus acid titrant volume, respectively, and M_A is the molarity of the acid titrant added to the seawater sample. Twenty-two bottles of KANSO TECHNOS reference material were measured (batch AV; 2313.1 ±

1.2 μmol kg^{-1}, average measured value 2313.1 ± 1.7 μmol kg^{-1}). An adjustment was applied to the measured value to remove this average measured difference. The mean ± standard deviation of the measured differences for replicate samples was 2.1 ± 1.9 μmol kg^{-1} (n = 55).

Nutrient samples were put in a water bath adjusted to 22.4 ± 0.7˚C for at least 30 min before measurement to ensure a constant sample temperature. Samples with a permeability of less than 95% were measured after sedimentation of suspended particles using a centrifuge. (CN-820 centrifuge, Hsiangtai Machinery Industry Co., Ltd., Taiwan; 3400 rpm, 2.5 min). Samples were analyzed within 24 h after collection using a QuAAtro 39 system (BL TEC K.K., Japan). The repeatability of NO_3^- was 0.14% (n = 28). Samples for chlorophyll-*a* analysis were extracted with DMF and analyzed within 24 h of collection with a fluorometer (10-AU, Turner Designs, Inc., USA) following Welschmeyer (1994). The fluorometer was calibrated against pure chlorophyll-*a* (Sigma-Aldrich Co., LLC, USA).

4.2.5. On-land Sample Analysis

The TA was determined by titration (Dickson et al., 2007) using a TA analyzer (ATT-05, Kimoto Electric Co., Ltd., Japan) for meltwater samples. Two replicates of KANSO TECHNOS reference material (batch AV; 2311.6 ± 1.2 μmol kg^{-1}; average measured value 2313.4 ± 0.5 μmol kg^{-1}) were measured at the beginning of each analyzing day to correct the measured values. The standard deviation of the TA measurements, calculated from 10 subsamples taken from reference water, were less than 2.0 mmol kg^{-1}.

To check the salinity range for TA analyses, we prepared low-salinity TA water by stepwise dilution of KANSO reference seawater with Milli-Q water. The salinity and TA were highly correlated (r^2 = 0.9999) and almost directly proportional to one another (Figure S4.1).
Stable oxygen isotopic ratios ($\delta^{18}O$) of surface seawater were measured with a mass spectrometer (DELTA V Advantage; Thermo Fisher Scientific, Germany) (dual inlet mode) at Shoko Science (Saitama, Japan) by the equilibration method. $\delta^{18}O$ (‰) was calculated using the ^{18}O:^{16}O ratio of standard mean ocean water (SMOW) as the standard. Three different working standards (DOW3, −0.07‰; AGW, −18.58‰; and SLW4, −9.62‰) were used to confirm the accuracy of the measurements. The standard deviation of $\delta^{18}O$ values, calculated from six subsamples of reference water with a $\delta^{18}O$ value of −0.07‰, was <0.05‰.

For measurements of the spectral absorption coefficient of CDOM (aCDOM(λ)), we followed the protocol of the IOCCG (International Ocean Colour Coordinating Group) CDOM working group (https://ioccg.org/wp-content/uploads/2019/10/cdom_abs_protocol_public_draft-19oct-2019-sm.pdf). The optical density spectra of CDOM ($OD_{CDOM}(\lambda)$) were measured using an Ultrapath spectrophotometer (World Precision Instruments, Inc.) at wavelengths of 200−735 nm and a path length of 200 cm. The null correction was performed against reference milli-Q water with a predetermined salinity correction curve as follows:

$$OD_{CDOM}(\lambda) = (OD_{meas}(\lambda) - (slope * Sal - intercept)) - OD_{mq}(\lambda) \quad (1)$$

where the slope and intercept are the coefficients of the salinity correction curve, and OD_{meas} and OD_{mq} are the spectral optical density of measured CDOM samples and milli-Q water, respectively. Then, aCDOM (λ) was calculated as follows:

$$aCDOM(\lambda) = 2.303\, OD_{CDOM}/l \quad (2)$$

where 2.303 is the factor to convert natural logarithms to common logarithms, and l is the optical path length (= 2 m).

4.2.6. Air−Sea CO_2 flux

The sea surface CO_2 flux, $F_{air-sea}$, was calculated using the following equation:

$$F_{air-sea} = k\, \alpha\, \Delta pCO_2 \quad (3)$$

where k is the gas transfer velocity (Ho et al., 2006), α is CO_2 solubility (Weiss, 1974), and ΔpCO_2 is the pCO_2 difference, which is defined as sea surface pCO_2 minus atmospheric pCO_2. Negative fluxes indicate that atmospheric CO_2 is being absorbed by the ocean. Gas transfer velocities were calculated by converting daily mean wind speeds. Wind speed and direction were observed on board during the cruise.

4.3. Results and Discussion

4.3.1. Spatial Distribution and Temporal Variations of the Surface Environment and CO_2 fluxes

Figure 4.2 shows the spatial distribution of marine biogeochemical properties in the surface ocean during the observation period, and Figure 4.3 shows the temporal variations. North of 65˚N, pCO_2 showed strong spatial variation in the range 180−405 µatm (Figure 4.2d). The mean pCO_2 was 315 ± 41 µatm and was undersaturated with respect to the atmospheric pCO_2 of 404 ± 4 µatm observed during the cruise. This result indicates that this area was potentially a sink for atmospheric CO_2 during September−October. The pCO_2 was particularly low (<250 µatm) around 65−66˚N and 71−72˚N (Figure 4.2d). Observations were conducted on the outward leg of this cruise in early September and on the return leg in early October (Figure 4.1a). Low pCO_2 values were observed in early September (Figure 4.3d). At 71−72˚N, the low sea surface temperature and salinity (Figures 4.2a, b) may have been the result of a large influx of freshwater. In contrast, pCO_2 was relatively high in the northernmost part of the Arctic Ocean (north of 72˚N). The pCO_2 was expected to be lower in this area because the water temperature and salinity are relatively low. This discrepancy is discussed in more detail in section 4.3.2.

The air−sea CO_2 flux was calculated using Equation (3) and the pCO_2 data (except no flux was calculated for 5 October, when wind speed data were missing). The mean CO_2 flux ± standard deviation was −10.5 ± 11.0 mmol C m^{-2} day^{-1} (−54.1 to −0.4 mmol C m^{-2} day^{-1}). The ocean was therefore taking up CO_2 from the atmosphere. Zheng et al. (2021) have estimated the air−sea CO_2 flux in the Chukchi Sea in September based on the coupled ocean–sea ice biogeochemical model to be −9.0 ± 3.5 mmol C m^{-2} day^{-1}, which is consistent with our results. The spatial distribution of the flux was generally similar to the spatial distribution of sea surface pCO_2, which was always below atmospheric pCO_2 (Figure 4.2e). However, CO_2 absorption was small around 68˚N, where pCO_2 was relatively low (approximately 250 µatm). The temporal data (Figures 4.3d, e), which indicate that CO_2 absorption was large in the middle and at the end of the observation period, were inconsistent with the distribution of sea surface pCO_2. This inconsistency may have been due to wind speed, which strongly influences the air−sea CO_2 flux. South of 68˚N, a large difference in wind speeds was observed between September and October (7.4 ± 0.2 m s^{-1} during 8−9 September and 12.7 ± 2.8 m s^{-1} from 30 September to 2 October). The variations of CO_2 fluxes may thus have reflected temporal differences in wind speed rather than spatial differences in sea surface properties in some cases.

4.3.2. Quantitative Assessment of Drivers of pCO_2 Variations from Winter to Summer

We used the methods described in Chapter 2 to estimate the variations of pCO_2 caused by biological activity, freshwater inflows, and changes in water temperature. We have estimated winter values in the Southern Ocean based on data in Chapter 2 for the temperature minimum layer (TML). In addition, Kosugi et al. (2017), who carried out studies in the Pacific sector of the Arctic Ocean, have also estimated carbonate system parameters by assuming that the water in the TML preserves the characteristics of Pacific water (the TML is also known as the Pacific-origin water layer, e.g., Shimada et al., 2005). Using the same approach, we determined the winter water temperature and salinity to be −1.4˚C and 32.5, respectively. However, in the Arctic Ocean, biogeochemical parameters in the TML may be affected by decomposition of organic matter because of the shallow slope, which is affected by sediments. We therefore corrected the DIC, TA, and NO_3^- values based on dissolved oxygen content and a remineralization N/−O_2/C molar ratio of 16/170/117 (Anderson and Sarmiento, 1994). Because AOU is more similar to "true oxygen utilization" in the Arctic Ocean than in other regions (Carter et al., 2021), we used AOU to correct the parameters here.

The average of our estimated DIC, TA, and NO_3^- contents were 2168 ±14 μmol kg^{-1}, 2269 ± 12 μmol kg^{-1}, and 6.6 ± 1.2 μmol kg^{-1}, respectively. Our estimates were consistent with those Kosugi et al. (2017), who studied the same region and estimated the DIC and TA contents in Pacific-origin water to be 2170 μmol kg^{-1} and 2264.2 μmol kg^{-1}, respectively. Then, pCO_2 in winter was calculated using the estimated values of water temperature, salinity, DIC, and TA. The winter pCO_2 averaged 383 μatm and ranged from 373 to 390 μatm, depending on the DIC and TA. According to Murata et al. (2022), the high values of pCO_2 during early winter in this area are 370−400 μatm. The implication is that our estimates are reasonable and, considering that the water is covered with ice in the winter, can be assumed to be spatially uniform.

The increase in sea surface temperature during the summer causes the solubility of CO_2 to decrease and, hence, pCO_2 to increase (Takahashi et al., 2002). We therefore calculated the pCO_2 for the case where the temperature changed from winter to summer by substituting the observed sea surface temperature into CO2SYS ver. 02.05 (Orr et al., 2018). For the calculation, we used the equilibrium constants of Dickson and Millero (1987), which were refit from Mehrbach et al. (1973). In contrast, a decrease in salinity caused by the inflow of freshwater, which contains fewer carbonate ions,

dilutes the carbonate components and salinity, and results in a higher CO_2 solubility and a lower pCO_2. DIC and TA after dilution (DIC_{dil} and TA_{dil}) were calculated by normalization of their values relative to the sea surface salinity based on following equations and substituted into CO2SYS to calculate the change in pCO_2 due solely to the freshwater supply.

$$DIC_{dil} = DIC_{winter} \times (S_{obs} / S_{winter}) \quad (4)$$

$$TA_{dil} = TA_{winter} \times (S_{obs} / S_{winter}) \quad (5)$$

where S is salinity, and the subscripts "winter" and "obs" means winter data and observation data. In accord with the salinity endmember for seawater in Yamamoto-Kawai et al. (2008), S_{winter} was set to 32.5.

The seasonal variation in DIC from winter to summer due to biological effects ($\Delta[nDIC]_{winter-summer;}$ i.e., net community production) can be calculated from the change in nutrient content from winter to summer. (e.g., Shadwick et al., 2014; Tamura et al., 2022).

$$\Delta[DIC]_{winter-summer} = ([nN]_{TML} - [nN]_{surface}) \cdot (106/16) \quad (6)$$

where $[nN]_{TML}$ is the nitrate content in the water temperature minimum layer and $[nN]_{surface}$ is the observed nitrate content normalized by the salinity in winter. The difference in nutrient content between winter and summer was multiplied by 106/16 according to the Redfield ratio (Redfield et al., 1963) to convert nitrate content into changes in DIC. We calculated the normalized change of TA, Δ(nTA), in the same way as Δ(nN). Substituting these DIC and TA values into CO2SYS, we calculated the change in pCO_2 due to only biological activity.

The differences from the pCO_2 after it was changed by each of these effects (temperature, freshwater supply, and biological activity) minus winter pCO_2 are referred to as δpCO_{2_temp}, δpCO_{2_sal}, and δpCO_{2_bio}, respectively. The residual difference that could not be explained by δpCO_{2_temp}, δpCO_{2_sal}, and δpCO_{2_bio} was considered to be due to other effects (such as gas exchange, nonlinearities in the seawater carbonate system, and advection) and is referred to as δpCO_{2_others}.

When we calculated δpCO_2 values (δpCO_2) (Figure 4.4), δpCO_{2_temp} was 72 ± 40 μatm (8 to 162

μatm) (Figure 4.4a), δpCO_{2_sal} was −63 ± 25 μatm (−111 to −22 μatm) (Figure 4.4b), and δpCO_{2_bio} was −108 ± 8 μatm (−113 to −60 μatm) on average (Figure 4.4c). These values mean that, on average, winter pCO_2 changed by +19%, −17%, and −28%, respectively. δpCO_{2_temp} tended to be smaller toward the north (~50 μatm) and larger toward the south (~150 μatm). δpCO_{2_sal} was largely negative (implying a large reduction in pCO_2) in the southern part of the region (~ −100 μatm), and it was also relatively small around 68˚N (~ −80 μatm). δpCO_{2_bio} was almost uniform spatially, as indicated by its small standard deviation.

δpCO_{2_others} (= $\delta pCO_{2\_winter\text{-}summer}$ − (δpCO_{2_temp} + δpCO_{2_sal} + δpCO_{2_bio})) includes the effects of air–sea gas exchange and advection. The winter pCO_2 was 383 μatm, whereas atmospheric pCO_2 was 404 ± 4 μatm. Comparison of winter pCO_2 and atmospheric pCO_2 suggests a potential CO_2 uptake from the atmosphere to the sea surface and an increase of 21 μatm of pCO_2 because of air–sea gas exchange. However, most δpCO_{2_others} values were positive in the Canada Basin (83 ± 63 μatm) and negative in the Chukchi Sea (−22 ± 37 μatm; Figure 4.4d). This difference may reflect the difference of water properties between the Chukchi Sea and Canada Basin. For example, according to Walsh et al. (2005), the winter NO_3^- content is lower in the Canada Basin than in the Chukchi Sea (0.5 μmol kg^{-1} in the Canada Basin and 10 μmol kg^{-1} on the eastern side of the Bering Strait). Therefore, the $[nN]_{TML}$ may need to be changed in the Canadian Basin and the Chukchi Sea. If we calculated the $\delta pCO_{2\_bio\_recal}$ in the Canada Basin by using 0.5 μmol kg^{-1} of NO_3^-, it increased to over −15 μatm, and the $\delta pCO_{2\_others\_recal}$ became negative (−26 ± 63 μatm) (Figure S4.2). This result shows the uncertainty of this estimate and emphasizes the importance of in situ observations of the differences of conditions in the Canadian Basin and the Chukchi Sea in the winter. Furthermore, we must consider the effects of simultaneous freshwater inflow and biological activity to interpret δpCO_{2_others}. The decrease of DIC and the increase of TA due to biological activity both contribute to a decrease in pCO_2, whereas the decrease of TA due to dilution contributed to an increase of pCO_2. If they occur simultaneously, the impact of lowering pCO_2 may therefore be smaller than the sum of the effects. Indeed, the negative correlation between δpCO_{2_sal} and δpCO_{2_others} (r^2 = 0.86; Figure S3) indicates that the higher the freshwater inflow, the higher the pCO_2 due to other factors. Some of the δpCO_{2_other} could therefore be attributed to changes in the carbonate system due to the simultaneous occurrence of freshwater inflow and biological activity. Therefore, we calculated δpCO_2 assuming simultaneous changes in temperature, salinity, and biological activity (δpCO_{2_total}). The difference between the sum of three δpCO_2 and δpCO_{2_total} (=δpCO_{2_total}−(δpCO_{2_temp} + δpCO_{2_sal} + δpCO_{2_bio})) was −21 ± 16 μatm (−52 to 8 μatm). This difference indicates the effect of the nonlinearity of carbonate chemistry.

Furthermore, we also need to consider the equilibrium constants in CO2SYS. We recalculated the pCO_2 with the carbonate chemistry constants from Sulpis et al. (2020). The recalculated pCO_2 was 3.8 ± 0.9% higher than original pCO_2, with larger change at the low temperature. Accordingly, δpCO_{2_temp}, δpCO_{2_sal}, and δpCO_{2_sal} changed by −9, −7, and −12 µatm, respectively. This uncertainty based on the carbonate chemistry constants was also included in δpCO_{2_others}.

When we considered the standard deviations of DIC, TA, and NO_3^-, we found that these uncertainties changed δpCO_{2_temp} and δpCO_{2_sal} by about 5 µatm at most. In contrast, δpCO_{2_bio} changed by nearly 20 µatm because of the large absolute values of pCO_2 change. These errors underline the importance of estimating winter data. The accuracy of this estimation can be improved by in situ observations of the under-ice water in winter.

4.3.3. Impacts of Freshwater Type on Sea Surface pCO_2

The Southern Ocean dataset indicated that most of the freshwater in this region was sea ice meltwater, and the effects of sea ice meltwater on pCO_2 were small because of the low abundance of sea ice meltwater (See section 2.4.2). However, as mentioned in the introduction, the Arctic Ocean has a high abundance of freshwater, including snow meltwater and river water in addition to sea ice meltwater. However, our assessment of δpCO_{2_sal} ignored the difference of freshwater types. If the effects of these different freshwater types on pCO_2 differ, they cannot be correctly assessed by the method described above. Therefore, in this section, we examine the effect of each freshwater type on pCO_2.

To determine the different impact of each freshwater type on pCO_2, we first examined the distribution of each freshwater type based on $\delta^{18}O$ and salinity values using the following equations (Burgers et al., 2017; Östlund & Hut, 1984):

$$f_{sw}\,S_{sw} + f_{sim}\,S_{sim} + f_{mw}\,S_{mw} = S_{obs} \quad (7)$$

$$f_{sw}\,\delta_{sw} + f_{sim}\,\delta_{sim} + f_{mw}\,\delta_{mw} = \delta_{obs} \quad (8)$$

$$f_{sw} + f_{sim} + f_{mw} = 1 \quad (9)$$

where *f* indicates the fraction, *S* is salinity, δ is $\delta^{18}O$, and the subscripts "sw", "sim", "mw", and "obs" indicate seawater, sea ice meltwater, meteoric water (snow meltwater and river water), and the observed value, respectively. The salinity and $\delta^{18}O$ endmember values were obtained from Yamamoto-Kawai et al. (2008) (Table 4.1). Note that differences between the effects of rain and snow and evaporation on the observed $\delta^{18}O$ values were not taken into account, which could be a source of error. We further distinguish between these two meteoric water components (rivers and snow melt) using CDOM, as described below.

Sea ice meltwater increased towards the north (Figure 4.5b). The meteoric water fraction was higher (10−15%) north of 72˚N and around 68˚N than elsewhere (Figure 4.5c). Calculation of the fractions from salinity and $\delta^{18}O$ does not allow snow meltwater and river water to be distinguished in the meteoric water signal. Therefore, we used aCDOM(λ) at wavelengths of 375 nm (aCDOM(375)), an indicator of river water, to distinguish the river water and snow meltwater fractions (Blough & Del Vecchio, 2002; Nelson & Guarda, 1995; Nieke et al. 1997; Twardowski & Donaghay, 2001).

Figure 4.5d shows the relationship between the fraction of meteoric water and aCDOM(375). Mungall et al. (2017) have reported that aCDOM(375) via rivers can be high, and high aCDOM(375) is often used as an indicator of river water. In the southern area (around 68˚N), the meteoric water fraction and aCDOM(375) were positively correlated; this result suggests an inflow of river water into this area. North of 72˚N, however, the meteoric water fraction showed no correlation with aCDOM(375); this result suggests that the meteoric water fraction there consisted of snow meltwater. Snow sometimes accumulates on sea ice (Merkouriadi et al., 2020) and is captured within the sea ice. A large amount of multi-year ice was observed in the northern area during the cruise; thus, the sea ice in this area could have been affected by the accumulation of snow over a long period. Indeed, the results of the salinity, $\delta^{18}O$ (See next paragraph for details; Figure 4.6) and thin section analysis (photographs not shown) of sea ice samples indicate that the sea ice contained a large amount of snow. The snow meltwater signal observed north of 72˚N therefore reflected snow in the multi-year ice.

We next investigated the carbonate chemistry of the snow-affected sea ice samples and assessed their impact on pCO_2. Figures 4.6a and b show the relationship between salinity and DIC or TA in sea ice meltwater. Both DIC and TA were strongly correlated with salinity (DIC, $r = 0.98$; TA, $r = 0.97$; $p < 0.01$ for both).

To determine the mass fraction of snow in sea ice meltwater samples, we used a mass balance equation model (Jeffries et al., 1994; 2001):

$$f_{snow} + f_{sea} = 1 \quad (10)$$

$$f_{snow}\,\delta_{snow} + f_{sea}\,\delta_{sea} = \delta_{obs} \quad (11)$$

where f represents the mass fraction of snow or seawater, δ represents their $\delta^{18}O$ values, and the subscripts 'snow', 'sea', and 'obs' indicate snow, seawater, and observed bulk ice, respectively. The same endmember of the seawater as equation (7) was used and corrected (+2‰; i.e., 1.2‰) according to Jefferies et al. (1994, 2001). The endmember of snow was the same as the endmember of meteoric water in equation (7).

The mean percentage of snow in sea ice samples was 17 ± 9% (n = 71). The estimated volume of sea ice meltwater from March to October in the area bounded by 72−74˚N, 150−170˚W was 260 km^3 based on the concentration and thickness of sea ice estimated from CyroSat-2 satellite data. If the salinities of sea ice and snow were 4 and 0, respectively (Table 4.2), and the mixed layer depth in summer was 10 m, melting of sea ice would have caused the salinity to decrease from 32.5 to 27.3. The implication is that sea ice meltwater and the contribution of snow to it could explain a large part of the winter-to-summer change of salinity.

Some sea ice samples contained a high snow fraction (>70%, Figures 4.6a, b), but even in those samples, the relationship between salinity and DIC or TA was similar to that in other samples. The regression lines for salinity and DIC or TA were DIC = 55.4S + 18.0 and TA = 70.2S + 4.1 (RMSE were 6 and 10 μmol kg^{-1}), respectively, and the slopes were statistically significantly different (p < 0.05). The implication is that TA decreased more rapidly than DIC as salinity decreased. The balance between the effect of DIC decrease and effect of TA decrease had a significant impact on pCO_2 values, because pCO_2 decreases as DIC decreases, whereas it increases as TA decreases (DeGrandpre et al., 2019). We used CO2SYS to calculate the pCO_2 in sea ice meltwater using the observed DIC and TA values of the sea ice meltwaters and assuming a freezing point of −1.8˚C. For the calculation, we used the equilibrium constants of Dickson and Millero (1987), which were refit from Mehrbach et al. (1973), and the $[B]_T$ value from Uppstrom (1974). pCO_2 increased as salinity decreased below 1, possibly because the decrease in TA had a greater effect than the decrease in

DIC on the pCO_2 in the low-salinity meltwater (Figure 4.6c). Because the salinity of sea ice decreases as brine is discharged (Malmgren, 1927), sea ice salinity is lower in older sea ice than younger sea ice. This result suggests that meltwater of older sea ice or snow-rich sea ice (i.e., low-salinity meltwater) has a smaller effect on reducing pCO_2 than meltwater from younger sea ice (relatively high salinity meltwater). The implication is that snowmelt water would show a pCO_2 similar to these low-salinity samples (Figure 4.6c) and that snow and ice with low salinity, irrespective of their ice origin, would have a smaller effect on lowering pCO_2. If snow meltwater flows into the sea surface layer, it would be expected to greatly reduce salinity and strongly dilute DIC and TA but not reduce pCO_2 very much. This prediction is consistent with the high pCO_2 values in the northern part of the study area, despite the very low salinity observed there.

We next examined the impact of river water on pCO_2. Around 68˚N, where the river water signal was strong, pCO_2 was higher (375−400 µatm) than in the surrounding area (approximately 300 µatm). Although river water may flow into this area from both Alaskan and Siberian rivers, the carbonate chemistry of river water is different in each river, and in particular, Alaskan rivers have higher DIC and TA than Siberian rivers (Tank et al., 2012; Cooper et al., 2008). The mean TA ± standard deviation calculated from the pCO_2 and DIC values obtained by underway measurements around 68−69˚N was 2106 ± 47 µmol kg^{-1} (n = 107). A river water percentage of 10% and an underway TA of 2106 µmol kg^{-1} during the observation gave a river water TA of approximately 1182 µmol kg^{-1}. According to Cooper et al. (2008), the flow-weighted average of TA for the six largest Arctic rivers (Ob', Yenisey, Lena, Kolyma, Yukon, Mackenzie) is 1048 µmol kg^{-1}. The average value for Siberian rivers (Ob', Yenisey, Lena, Kolyma) is 816 µmol kg^{-1}, whereas the value for the Alaskan river is 1628 µmol kg^{-1}. When these values are used in the calculations, it is estimated that 45% of the river water in this area originates from Alaskan rivers and 55% from Siberian rivers.

In addition, we calculated the fraction of meteoric water (f_{mw_TA}) in the Canada Basin by using the endmembers of salinity and TA for seawater, sea ice meltwater, and Alaskan rivers (Table 4.2). The mean f_{mw_TA} was 2.8 ± 2.2%, which was smaller than f_{mw} based on $\delta^{18}O$ (10.6 ± 3.1%). This result indicated that most meteoric water in the Canada Basin was river water.

On the basis of the above results, we discuss the change in pCO_2 when freshwater is mixed with seawater. Using the regression equation for DIC and TA in sea ice meltwater (Figures 4.6a, b) and the endmember values for Alaskan and Siberian rivers from previous studies (Tank et al., 2012;

Cooper et al., 2008), we estimated pCO_2 values for mixtures of each freshwater type with seawater in the Chukchi Sea in winter (Figure 4.7, Table 4.2). The DIC and TA of the rivers that discharge into the Chukchi Sea were determined assuming that the rivers on the Alaska side and Siberian side were mixed at 45% and 55%, respectively. In that case, pCO_2 increased because of the inflow of river water. Mixing of river water and seawater sometimes may improve the light environment if particles settle out because of coagulation. The result is a temporary increase of production and lower pCO_2 in the estuary (Zhai et al., 2007). However, CDOM limits light availability by absorbing light in the same range as the absorption peak of chlorophyll *a* (Arrigo and Brown, 1996). The pCO_2 around 68˚N was therefore relatively high. On the other hand, the inflow of sea ice meltwater with a salinity of 4 and snow meltwater with a salinity of 0 decreased pCO_2. As mentioned above, snow meltwater (i.e., low-salinity meltwater) has a smaller effect on pCO_2 than sea ice meltwater. Assuming that salinity decreases to 27 because of the inflow of each freshwater, pCO_2 changes to 391 μatm due to river water, 276 μatm due to sea ice meltwater and 300 μatm due to snow meltwater (Figure 4.7).

4.3.4. New Method for Quantifying pCO_2 Changes That Considers Freshwater Type

To take account of the impact of each freshwater type on pCO_2, we re-examined the quantification method presented in section 4.3.2. We calculated the fractions of seawater, sea ice meltwater, snow meltwater, and river water by using salinity, DIC, and TA endmember values for these freshwater types (Table 4.2) to assess the impact of the freshwater supply. Considering the results shown in Figure 4.5d, we assumed that in the Canada Basin and Chukchi Sea, the meteoric water fraction consisted of snow meltwater and river water, respectively. We then estimated the change of DIC and TA due to the influx of freshwater using the freshwater fractions and endmember values for each freshwater type (Table 4.2). We then used these results to estimate the pCO_2 change, $\delta pCO_{2\_sal\_recal}$.

$$DIC_{\_sal\_recal} = f_{sw} \times DIC_{sw} + f_{sim} \times DIC_{sim} + f_{mw} \times DIC_{mw} \quad (12)$$

$$TA_{\_sal\_recal} = f_{sw} \times TA_{sw} + f_{sim} \times TA_{sim} + f_{mw} \times TA_{mw} \quad (13)$$

Figure 4.8a shows the distribution of $\delta pCO_{2\_sal\_recal}$. This distribution was comparable with that in Figure 4.4b. Figure 4.8b shows the distribution of $\delta pCO_{2\_sal\_differences}$ ($\delta pCO_{2\_sal\_recal} - \delta pCO_{2\_sal}$). In a wide area, the $\delta pCO_{2\_sal\_recal}$ from the new method was lower than the previous value δpCO_{2_sal}.

On the other hand, $\delta pCO_{2\_sal\_differencel}$ was found to be higher in areas with more river water (68−69˚N, +51.6 ± 22.1 µatm). In the Canada Basin, $\delta pCO_{2\_sal\_differences}$ was large and negative because there was a lot of sea ice meltwater as well as snow meltwater. We suggest that $\delta pCO_{2\_sal\_recal}$ has the potential to assess changes in pCO_2 more accurately than conventional methods.

4.3.5. Factors Driving pCO_2 Variability in the Pacific Sector of the Arctic Ocean.

In the Pacific sector of the Arctic Ocean, biological activity and temperature changes both had significant impacts on pCO_2 (Figures 4.4a, c), but because they were offsetting effects, they resulted in relatively small changes in pCO_2 from winter to summer. Considering the difference in nutrient content between the Chukchi Sea and Canada Basin, the effect of biological activity was larger in the Chukchi Sea than in the Canada Basin. In contrast, in the Canada Basin, the freshwater supply caused a significant decrease in pCO_2 (Figure 4.4b). In addition, pCO_2 was low at 72˚N, near the boundary between the Chukchi Sea and the Canada Basin, because of the high inflow of sea ice meltwater and the associated low water temperatures (Figures 4.2a, b). In addition, around 68˚N, where pCO_2 was relatively high, there was a locally high inflow of river water (Figure 4.5c).

Locally high or low pCO_2 was influenced mainly by freshwater inflows. In a study similar to ours, Kosugi et al. (2017) also found large differences in surface pCO_2 between the Chukchi Sea and the Canada Basin and suggested that suppression of biological production by nutrient-limited sea ice meltwater was a cause of the high pCO_2, up to 360 µatm, in the Canada Basin. This suggestion is consistent with our results. However, unlike our results, they reported that near Barrow, where river water was abundant, a high nutrient supply and high alkalinity were responsible for the lower pCO_2. This discrepancy suggests that the impact of river water in different areas may differ depending on its source and the volume of inflow. Further investigation of the carbonate components and nutrient content of freshwater is therefore needed to better understand the effect of changes in their contents and the degree of ocean stratification on sea surface pCO_2 when freshwater enters the sea surface water layer.

The results of this study as well as those of Kosugi et al. (2017) suggest that environmental changes might cause significant changes of pCO_2 in this area. Improved light conditions associated with reduced sea ice might also increase biological activity and lead to lower pCO_2, whereas increased

river water inflows might lead to a higher pCO_2. In addition, if sea ice production and the proportion of sea ice meltwater decrease, the effect of the freshwater supply on reductions in pCO_2 would be smaller. Therefore, in future projections of the freshwater supply, it will be important to consider not only the overall amount of freshwater but also the detailed composition of the freshwater supply.

4.4. Conclusion

We have presented results from observations in the Pacific Sector of the Arctic Ocean during summer 2021 to understand the spatial distribution of sea surface pCO_2 and the factors driving its variability. In this area, because pCO_2 is undersaturated with respect to the atmosphere, the area is a CO_2 sink. To determine the factors responsible for the observed spatial distribution of pCO_2, we focused on the pCO_2 changes from winter to summer and quantitatively assessed the changes in pCO_2 due to changes in water temperature, the freshwater supply, and biological activity. Freshwater inflow affected the spatial distributions of pCO_2 significantly. The pCO_2 was low in areas with a high sea ice meltwater contribution, and it was high in areas with a high river water contribution. The carbonate chemistry in sea ice samples and sea surface water clearly showed that sea ice meltwater, snow meltwater, and river water have different effects on pCO_2. Previous studies have assessed changes in pCO_2 due to freshwater supply, regardless of type, based on salinity, but this study used a method of analysis that considered the different effects of each freshwater source. For more accurate predictions of future CO_2 uptake in the Arctic Ocean, changes in the inflow of each freshwater type must be estimated and its impact on pCO_2 must be assessed. Furthermore, the error due to uncertainty of the winter estimate of δpCO_2 underlines the importance of understanding conditions under the ice. In situ data under ice would improve the accuracy of the estimation of seasonal changes in pCO_2.

Acknowledgments

We thank the crew and other cruise members of the R/V *Mirai* and Daisuke Hirano of the National Institute of Polar Research for useful advice and input into this research. We also thank the Hokkaido University Ambitious Doctoral Fellowship. This research was supported by the Japan Society for the Promotion of Science (23KJ0017). The study was conducted as part of the Arctic

Challenge for Sustainability II (ArCS II) project.

Data Availability Statement

This chapter is a modified version of Tozawa et al. (2024b). Observational data for this study are available from the data repository of the National Institute of Polar Research, Tokyo, Japan (https://ads.nipr.ac.jp/dataset/A20220803-006) and the JAMSTEC web page (http://www.jamstec.go.jp/e/). Note that the data site of JAMSTEC is now temporarily closed because of a security incident. Nevertheless, all of the data used in the present study can be obtained through the site (https://www.godac.jamstec.go.jp/darwin_tmp/explain/81/e). Supporting information is available from Tozawa et al. (2024b).

References

Anderson, L. A. and Sarmiento, J. L. (1994). Redfield ratios of remineralization determined by nutrient data analysis. *Global Biogeochemical Cycles*, 8, 65−80. https://doi.org/10.1029/93GB03318

Arrigo, K. R. and Brown, C. W. (1996). Impact of chromophoric dissolved organic matter on UV inhibition of primary productivity in the sea. *Marine Ecology Progress Series*, 140, 207−216. https://doi.org/10.3354/meps140207

Arrigo, K. R., van Dijken, G., Pabi, S. (2008). Impact of a shrinking Arctic ice cover on marine primary production. *Geophysical Research Letters*, 35, L19603. https://doi.org/10.1029/2008GL035028

Bates, N. and Mathis, J. (2009). The Arctic Ocean marine carbon cycle: Evaluation of air−sea CO_2 exchanges, ocean acidification impacts and potential feedbacks. *Biogeosciences*, 6, 2433−2459. https://doi.org/10.5194/bg−6−2433−2009

Bates, N. R., Moran, S. B., Hansell, D. A., Mathis, J. T. (2006). An increasing CO_2 sink in the Arctic Ocean due to sea−ice loss, *Geophysical Research Letters*, 33, L23609.

https://doi.org/10.1029/2006GL027028

Blough, N.V. and Del Vecchio, R. (2002). Biogeochemistry of Marine Dissolved Organic Matter, Academic Press, San Diego, California, pp. 509−546

Burgers, T. M., Miller, L. A., Thomas, H., Else, B. G. T., Gosselin, M., & Papakyriakou, T. (2017). Surface water pCO_2 variations and sea−air CO_2 fluxes during summer in the Eastern Canadian Arctic, *Journal of Geophysical Research: Oceans*, 122, 9663− 9678. https://doi.org/10.1002/2017JC013250

Carmack, E. C., Yamamoto-Kawai, M., Haine, T. W. N., Bacon, S., Bluhm, B. A., et al. (2016). Freshwater and its role in the Arctic Marine System: Sources, disposition, storage, export, and physical and biogeochemical consequences in the Arctic and global oceans. *Journal of Geophysical Research: Biogeosciences*, 121(3), 675-717. https://doi.org/10.1002/2015JG003140

Carter, B. R., Feely, R. A., Lauvset, S. K., Olsen, A., DeVries, T., Sonnerup, R. (2021). Preformed properties for marine organic matter and carbonate mineral cycling quantification. *Global Biogeochemical Cycles*, 35, e2020GB006623. https://doi.org/10.1029/2020GB006623

Cooper, L. W., McClelland, J. W., Holmes, R. M., Raymond, P. A., Gibson, J. J., Guay, C. K., Peterson, B. J. (2008). Flow−weighted values of runoff tracers ($\delta^{18}O$, DOC, Ba, alkalinity) from the six largest Arctic rivers, *Geophysical Research Letters*, 35, L18606. doi:10.1029/2008GL035007

DeGrandpre, M. D., Lai, C.−Z., Timmermans, M.−L., Krishfield, R. A., Proshutinsky, A., Torres, D. (2019). Inorganic Carbon and pCO_2 Variability During Ice Formation in the Beaufort Gyre of the Canada Basin. *Journal of Geophysical Research: Oceans*, 124, 4017− 4028.

Déry, S. J., Stadnyk, T. A., MacDonald, M. K., Gauli−Sharma, B. (2016). Recent trends and variability in river discharge across northern Canada. *Hydrology and Earth System Sciences,* 20(12), 4801−4818. https://doi.org/10.5194/hess−20−4801−2016

Dickson, A. G., and Millero, F. J. (1987). A comparison of the equilibrium constants for the dissociation of carbonic acid in seawater media. *Deep-Sea Research Part A* 34, 1733−1743. doi:10.1016/0198-0149(87)90021-5.

Dickson, A. G., Sabine, C. L., Christian, J. R. (2007). Guide to best practices for ocean CO_2 measurement (Vol. 3, p. 191). PICES Special Publication.

Haine, T. W. N., Curry, B., Gerdes, R., Hansen, E., Karcher, M., et al. (2015). Arctic freshwater export: Status, mechanisms, and prospects. *Global and Planetary Change*, 125, 13–35. https://doi.org/10.1016/j.gloplacha.2014.11.013

Ho, D. T., Law, C. S., Smith, M. J., Schlosser, P., Harvey, M., Hill, P. (2006). Measurements of air-sea gas exchange at high wind speeds in the Southern Ocean: Implications for global parameterizations, *Geophysical Research Letters*, 33, L16611. doi:10.1029/2006GL026817.

Jeffries, M., Shaw, R., Morris, K., Veazey, A., Krouse, H. (1994). Crystal structure, stable isotopes ($\delta^{18}O$), and development of sea ice in the Ross, Amundsen, and Bellingshausen seas, Antarctica. *Journal of Geophysical Research: Oceans*, 99 (C1), 985−995. https://doi.org/10.1029/93JC02057

Jeffries, M. O., Krouse, H. R., Hurst-Cushing, B., Maksym, T. (2001). Snow-ice accretion and snow-cover depletion on Antarctic first-year sea-ice floes. *Annals of Glaciology*, 33, 51−60.

Johnson, K. M. (1992). *Operator's manual: Single−Operator Multiparameter Metabolic analyzer (SOMMA) for total carbon dioxide (CT) with coulometric detection*. Brookhaven National Laboratory.

Johnson, K. M., King, A. E., Sieburth, J. M. (1985). Coulometric TCO_2 analyses for marine studies: An introduction, *Marine Chemistry*, *16*, 61−82. https://doi.org/10.1016/0304−4203(85)90028−3

Jones, E. M., Renner, A. H. H., Chierici, M., Wiedmann, I., Lødemel, H. H., Biuw, M. (2020). Seasonal dynamics of carbon-ate chemistry, nutrients and CO_2uptake in a sub-Arctic fjord. *J. Elementa: Science of the Anthropocene* 8: 41. https://doi.org/10.1525/elementa.438

Kosugi, N., Sasano, D., Ishii, M., Nishino, S., Uchida, H., and Yoshikawa-Inoue, H. (2017). Low pCO_2 under sea-ice melt in the Canada Basin of the western Arctic Ocean, *Biogeosciences*, 14, 5727−5739. https://doi.org/10.5194/bg-14-5727-2017

Li, Q., Chen, M., Jia, R.M., Zeng, J., Lin, H., Zheng, M.F., Qiu, Y.S. (2017). Transit time of river water in the Bering and Chukchi seas estimated from delta O−18 and radium isotopes. *Progress in Oceanography*, 159, pp. 115−129. https://doi.org/10.1016/j.pocean.2017.08.004

Malmgren, F. (1927). On the properties of sea-ice: Norwegian north polar expedition with the *Maud*, 941 1918-1925, sci. Results.

Mehrbach, C., Culberson, C. H., Hawley, J. E., Pytkowicz, R. M. (1973). Measurement of the Apparent Dissociation Constants of Carbonic Acid in Seawater at Atmospheric Pressure. *Limnology and Oceanography* 18, 897−907. doi:10.4319/lo.1973.18.6.0897

Merkouriadi, I., Liston, G. E., Graham, R. M., Granskog, M. A. (2020). Quantifying the potential for snow-ice formation in the Arctic Ocean. *Geophysical Research Letters*, 47, e2019GL085020. https://doi.org/ 10.1029/2019GL085020

Mungall, E. L., Abbatt, J. P. D., Wentzell, J. J. B., Lee, A. K. Y., Thomas, J. L., et al. (2017). Microlayer source of oxygenated volatile organic compounds in the summertime marine Arctic boundary layer, Proceedings of the National Academy of Sciences of the United States of America, 114(24), 6203−6208. https://doi.org/10.1073/pnas.1620571114

Murata, A., Inoue, J., Nishino, S., Yasunaka, S. (2022). Early Wintertime CO_2 Uptake in the Western Arctic Ocean. *Journal of Geophysical Research: Oceans*. 127. 10.1029/2021JC018037.

Nelson, J. R. and S., Guarda. (1995). Particulate and dissolved spectral absorption on the continental shelf of the southeastern United States. *Journal of Geophysical Research*, 100, p. 8715–8732. https://doi.org/10.1029/95JC00222

Nieke, B., Reuter, R., Heuermann, R., Wang, H., Babin, M., Therriault, C. (1997). Light absorption and fluorescence properties of chromophoric dissolved organic matter (CDOM), in the St. Lawrence Estuary (Case 2 waters). *Continental Shelf Research*, 17, p. 235~252. https://doi.org/10.1016/S0278−4343(96)00034−9

Orr, J. C., Epitalon, J. M., Dickson, A. G., Gattuso, J. P. (2018). Routine uncertainty propagation for the marine carbon dioxide system. *Marine Chemistr*y, 207, 84−107.

https://doi.org/10.1016/j.marchem.2018.10.006

Östlund, H. G., and Hut, G. (1984). Arctic Ocean water mass balance from isotope data, *Journal of Geophysical. Research*, 89, 6373−6381.

Parkinson, C. L. and Comiso, J. C. (2013). On the 2012 record low Arctic sea ice cover: Combined impact of preconditioning and an August storm. *Geophysical. Research Letters*, 40, 1356−1361. doi:10.1002/grl.50349

Rantanen, M., Karpechko, A.Y., Lipponen, A. et al. (2022). The Arctic has warmed nearly four times faster than the globe since 1979. *Communications Earth & Environment* 3, 168. https://doi.org/10.1038/s43247-022-00498-3

Redfield, A.C., Ketchum, B.H., Richards, F.A. (1963) .The Influence of Organisms on the Composition of the Sea Water. In: Hill, M.N., Ed., The Sea, Vol. 2, Interscience Publishers, New York, 26−77.

Shadwick, E. H., Tilbrool, B., Williams, G. D. (2014). Carbonate chemistry in the Mertz Polynya (East Antarctica): Biological and physical modification of dense water outflows and the export of anthropogenic CO_2, *Journal of Geophysical Research: Oceans*, 119, 1, 1−14. https://doi.org/10.1002/2013JC009286

Shimada, K., Itoh, M., Nishino, S., McLaughlin, F., Carmack, E., Proshutinsky, A. (2005). Halocline structure in the Canada Basin of the Arctic Ocean, *Geophysical Research Letters*, 32, L03605. https://doi.org/10.1029/2004GL021358

Shu, Q., Qiao, F., Song, Z., Zhao, J., Li, X. (2018). Projected freshening of the Arctic Ocean in the 21st century. *Journal of Geophysical Research: Oceans*, 123, 9232−9244. https://doi.org/10.1029/2018JC014036

Sulpis, O., Lauvset, S. K., Hagens, M. (2020). Current estimates of K_1* and K_2* appear inconsistent with measured CO_2 system parameters in cold oceanic regions, *Ocean Science*, 16, 847−862. https://doi.org/10.5194/os-16-847-2020.

Suzuki, R. and Ishimaru, T. (1990). An improved method for the determination of phytoplankton chlorophyll using N, N− dimethylformamide, *Journal of the Oceanographical Society of Japan*, 46, 190−194. https://doi.org/10.1007/BF02125580

Takahashi, T., Sutherland, S.C., Sweeney, C., Poisson, A., Metzl, N., et al. (2002). Global sea−air CO_2 flux based on climatological surface ocean pCO_2, and seasonal biological and temperature effects, *Deep−Sea Research II; Topical Studies in Oceanography*, 49, 1601−1622. https://doi.org/10.1016/S0967−0645(02)00003−6

Tamura, T. P., Nomura, D., Hirano, D., Tamura, T., Kiuchi, M., et al. (2022). Impacts of basal melting of the Totten Ice Shelf and biological productivity on marine biogeochemical components in Sabrina Coast, East Antarctica. *Global Biogeochemical Cycles*, 36, e2022GB007510. https://doi.org/10.1029/2022GB007510

Tank, S. E., Manizza, M., Holmes, R. M., McClelland, J. W., Peterson, B. J. (2012). The processing and impact of riverine nutrients and organic matter in the near− and offshore Arctic Ocean. *Estuaries Coasts*, 35, 353− 368. doi:10.1007/s12237−011−9417−3

Tozawa, M., Nomura, D., Matsuura, M., Hatta, M., Fujiwara, A., Yasunaka, S., Murata, A. (2024b). Quantitative assessment of factors contributing to variations in sea surface pCO_2 in the pacific sector of the Arctic Ocean. *Journal of Geophysical Research: Oceans*, 129, e2024JC021012. https://doi.org/10.1029/2024JC021012

Twardowski, M. S. and Donaghay, P. L. (2001). Separating in situ and terrigenous sources of absorption by dissolved materials in coastal waters. *Journal of Geophysical Research*, 106, p. 2545~2560. https://doi.org/10.1029/1999JC000039

Uppstrom, L. R. (1974). The boron/chlorinity ratio of deep-sea water from the Pacific Ocean. *Deep Sea Research and Oceanographic Abstracts*, 21 (2), 161−162. https://doi.org/10.1016/0011-7471(74)90074-6

Walsh, J. J., Dieterle, D. A., Maslowski, W., Grebmeier, J. M., Whitledge, E.E., et al. (2005). A numerical model of seasonal primary production within the Chukchi/Beaufort Seas. *Deep Sea Research Part II*, 52(24−26), 3541−3576. doi:10.1016/j.dsr2.2005.09.009

Wanninkhof, R. H., Park, G.−H., Takahashi, T., Sweeney, W., Feely, R., et al. (2013). Global ocean carbon uptake: Magnitude, variability and trends. *Biogeosciences*, 10(3), 1983−2000. https://doi.org/10.5194/bg−10−1983−2013

Weiss, R. F. (1974). Carbon dioxide in water and seawater: The solubility of a non−ideal gas. *Marine Chemistry*, 2, 203−205.

Welschmeyer, N.A. (1994). Fluorometric analysis of chlorophyll a in the presence of chlorophyll b and pheopigments. *Limnology and Oceanography*, 39, 1985−1992.

Yamamoto-Kawai, M., McLaughlin, F. A., Carmack, E. C., Nishino, S., Shimada, K. (2008). Freshwater budget of the Canada Basin, Arctic Ocean, from salinity, $\delta^{18}O$, and nutrients, *Journal of Geophysical. Research: Ocean*, 113, C01007. doi:10.1029/2006JC003858

Yamamoto-Kawai, M., McLaughlin, F., Carmack, E. (2013). Ocean acidification in the three oceans surrounding northern North America. *Journal of Geophysical Research: Oceans*, 118(11), 6274-6284. https://doi.org/10.1002/2013JC009157

Yao, W. and Byrne, R.H. (1998). Simplified seawater alkalinity analysis: Use of linear array spectrometers, *Deep Sea Research Part I: Oceanographic Research Papers*, 45, 1383−1392. https://doi.org/10.1016/S0967−0637(98)00018−1

Yasunaka, S., Siswanto, E., Olsen, A., Hoppema, M., Watanabe, E., et al. (2018). Arctic Ocean CO_2 uptake: An improved multiyear estimate of the air-sea CO_2 flux incorporating chlorophyll a concentrations. *Biogeosciences*, 15(6),1643−1661. https://doi.org/10.5194/bg-15-1643-2018

Yasunaka, S., Manizza, M., Terhaar, J., Olsen, A., Yamaguchi, R., et al. (2023). An Assessment of CO_2 Uptake in the Arctic Ocean From 1985 to 2018. *Global Biogeochemical Cycles*, 37(11), e2023GB007806. https://doi.org/10.1029/2023GB007806

Zhai, W., Dai, M., Guo, X. (2007). Carbonate system and CO_2 degassing fluxes in the inner estuary of Changjiang (Yangtze) River, China. Mar. Chem. 107 (3), 342–356. https://doi.org/10.1016/j.marchem.2007.02.011

Zheng, Z., Luo, X., Wei, H., Zhao, W., Qi, D. (2021). Analysis of the seasonal and interannual variations of air−sea CO_2 flux in the Chukchi Sea using a coupled ocean−sea ice−biogeochemical model, *Journal of Geophysical Research: Oceans*, 126, e2021JC017550. https://doi.org/10.1029/2021JC017550

Zhuang, Y., Jin, H., Cai, W−J., Li, H., Jin, M., Qi, Di., Chen, J. (2021). Freshing leads to a three−decade trend of decline nutrients in the western Arctic Ocean, *Environmental Research Letters*, 16 054047. DOI 10.1088/1748−9326/abf58b

Figures and Tables

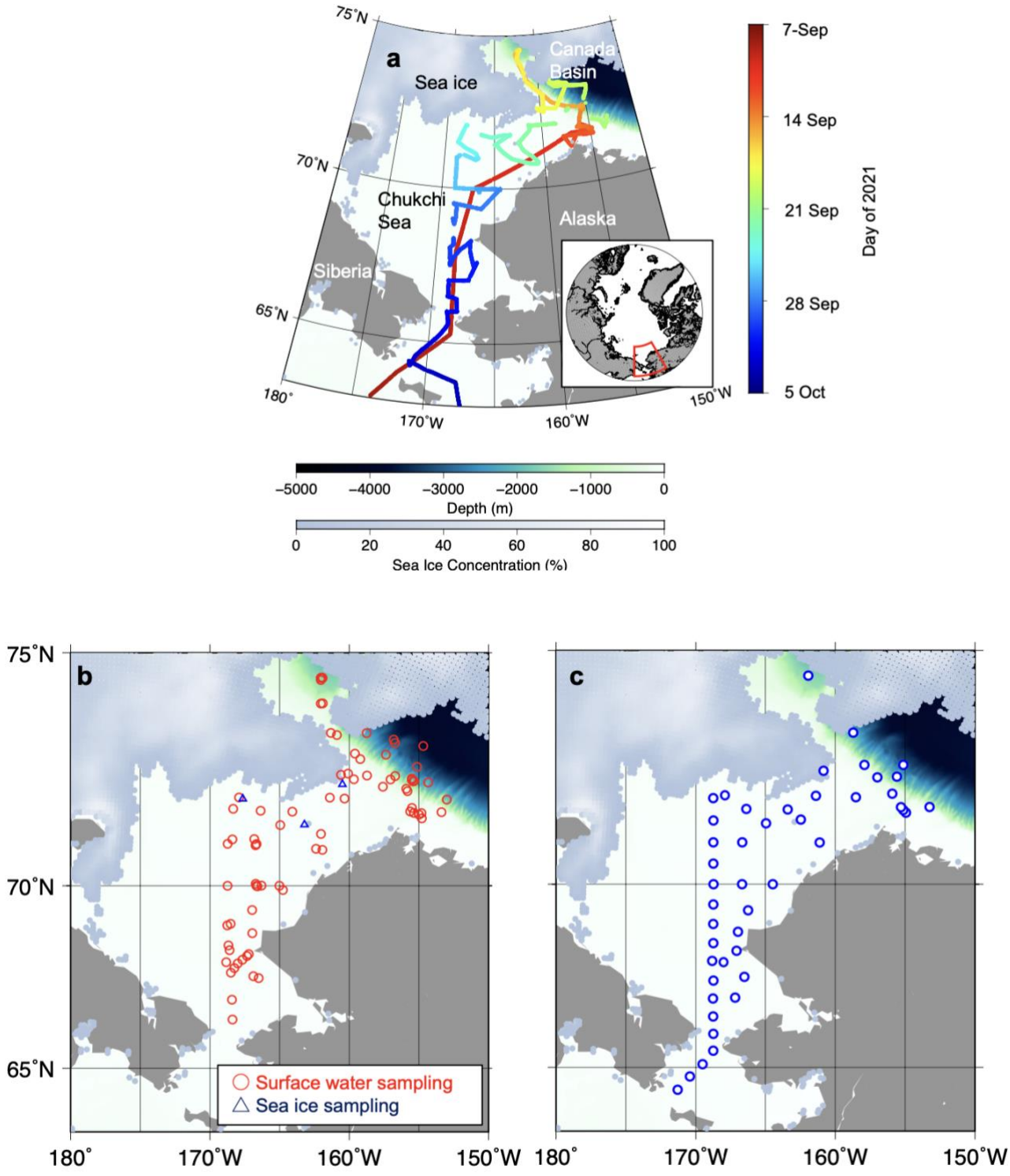

Figure 4.1. (a) Survey tracks. (b) Stations for underway (red circles) and sea ice (blue triangles) sampling. (c) Stations for CTD observations and vertical water profile sampling. Mean values of sea-ice concentrations during MR21-05C (from 31 August to 21 October 2021) are depicted based on the satellite image (CryoSat-2).

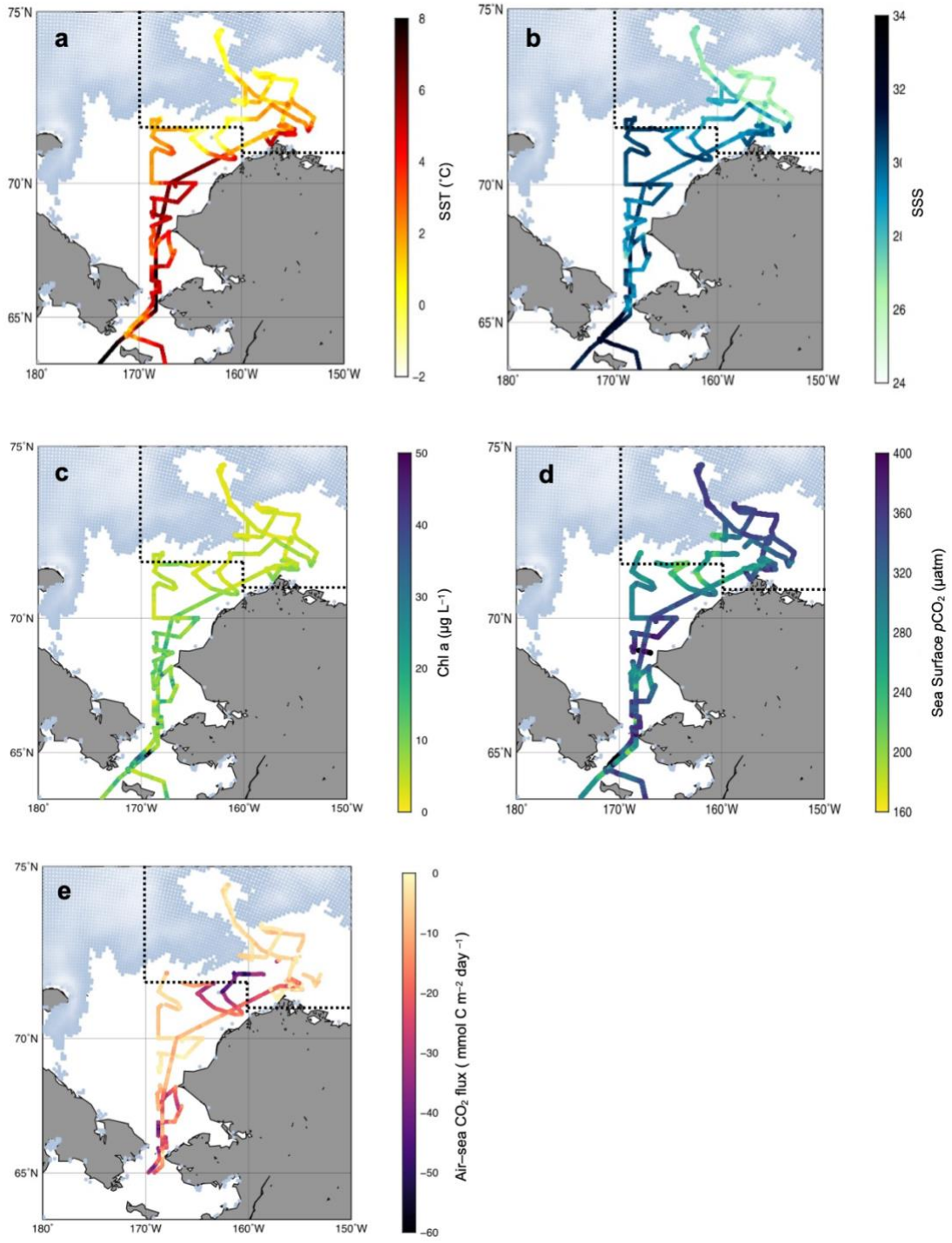

Figure 4.2. Horizontal distributions of biogeochemical parameters based on ocean surface observations. (a) Sea surface temperature (SST). (b) Sea surface salinity (SSS). (c) Chlorophyll-*a* concentration (Chl a). (d) Sea surface pCO_2. (e) Air−sea CO_2 flux. The dotted line indicates the boundary between the Chukchi Sea and the Canadian Basin in this study.

Note: In Figure 4.2c, all the values greater than 50 µmol L^{-1} are shown in the same color for clarity.

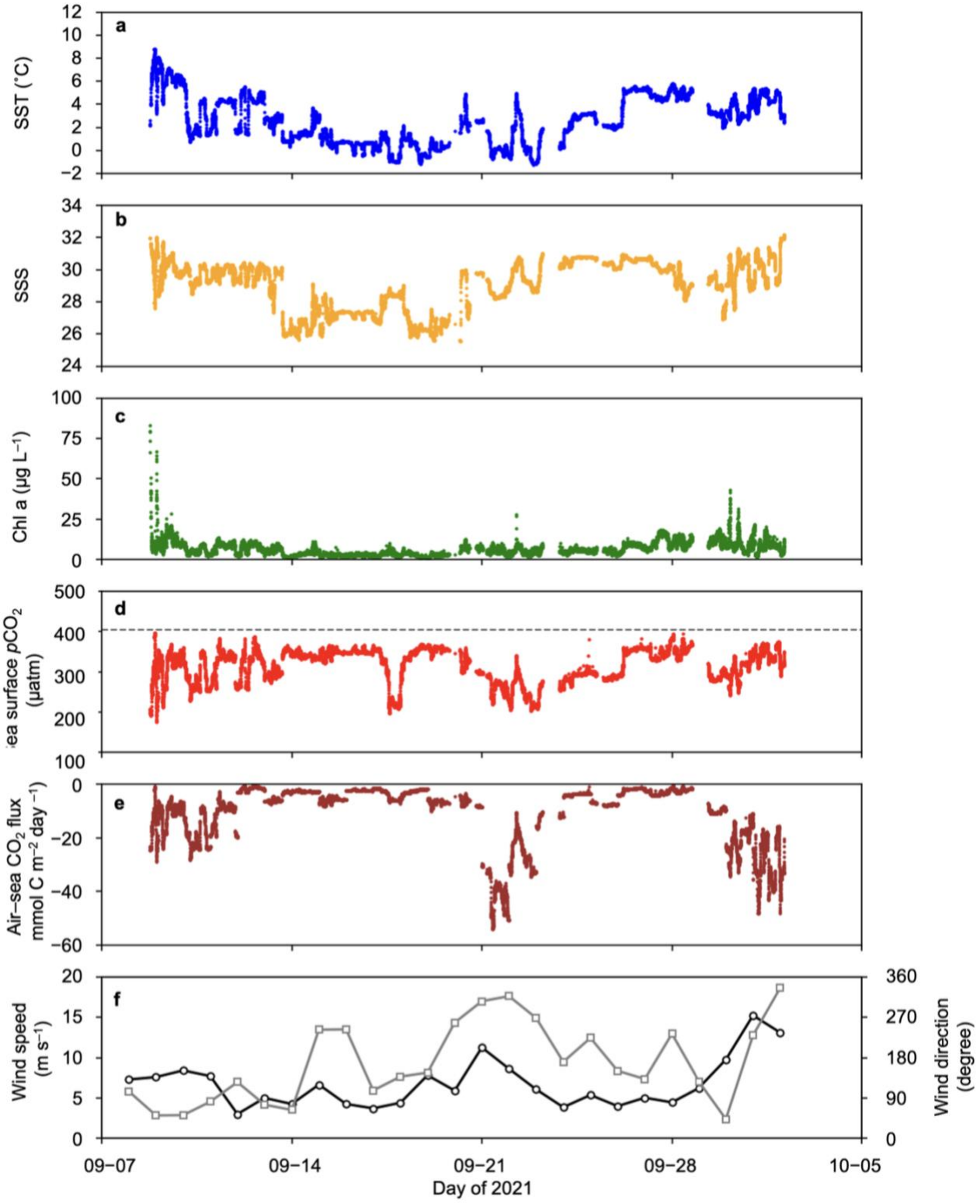

Figure 4.3. Time series of biogeochemical parameters based on ocean surface observations. (a) SST. (b) SSS. (c) Chl a. (d) Sea surface pCO_2. (e) Air−sea CO_2 flux. (f) Wind speed (black circle) and Wind direction (gray square). Wind data were averaged per day. Dashed line in (d) indicates the mean value of atmospheric pCO_2.

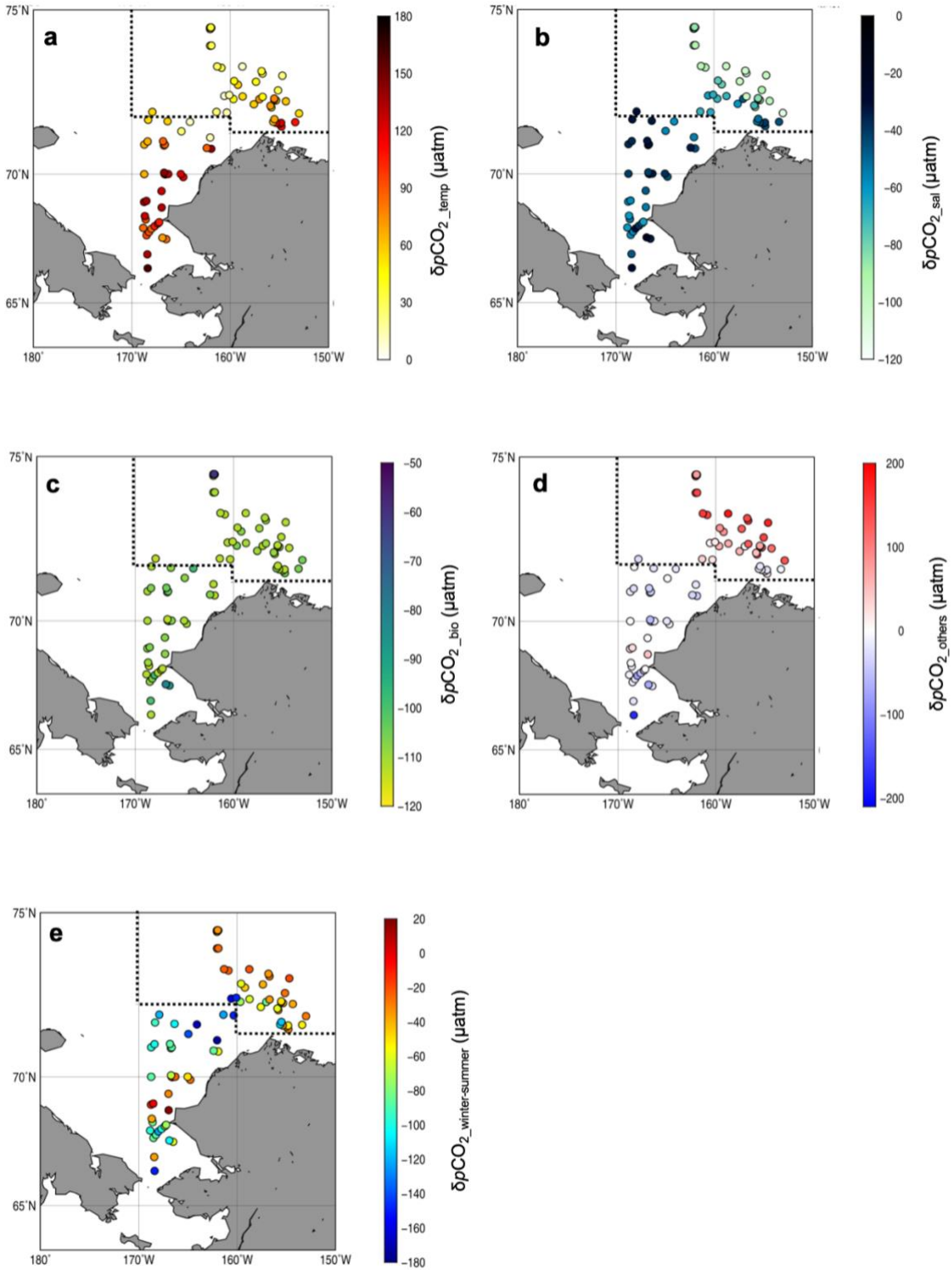

Figure 4.4. Spatial distributions of pCO_2 changes (δpCO_2). (a) δpCO_{2_temp}. (b) δpCO_{2_sal}. (c) δpCO_{2_bio}. (d) δpCO_{2_others}. (e) $\delta pCO_{2\_winter-summer}$. The dotted line indicates the boundary between the Chukchi Sea and the Canadian Basin in this study.

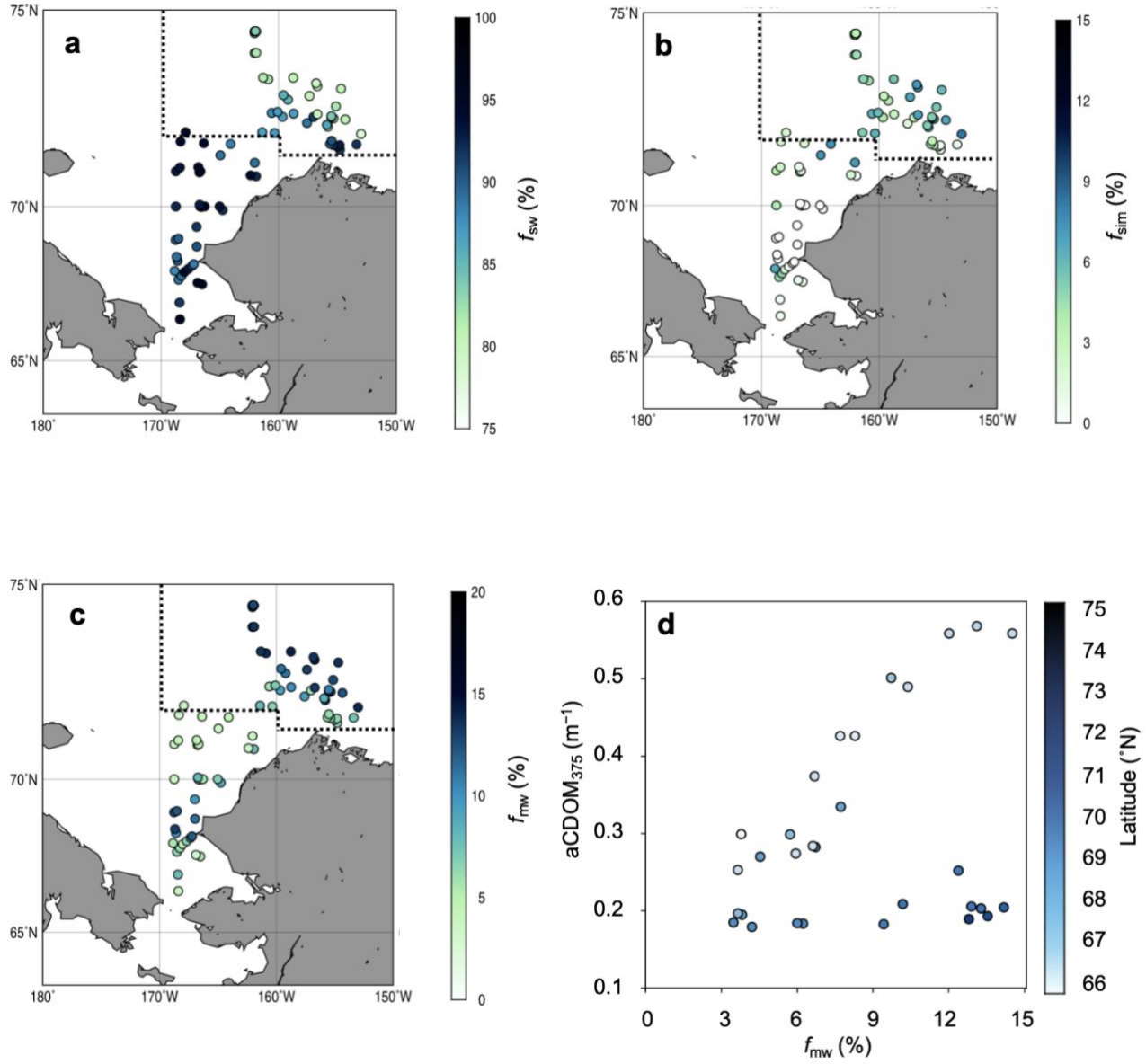

Figure 4.5. Freshwater distribution. Fractions of (a) seawater (f_{sw}); (b) sea ice meltwater (f_{sim}), and (c) meteoric water (f_{mw}). (d) Relationship between the meteoric water fraction and (aCDOM(375) (the color scale indicates latitude). The dotted line in (a)−(c) indicates the boundary between the Chukchi Sea and the Canadian Basin in this study.

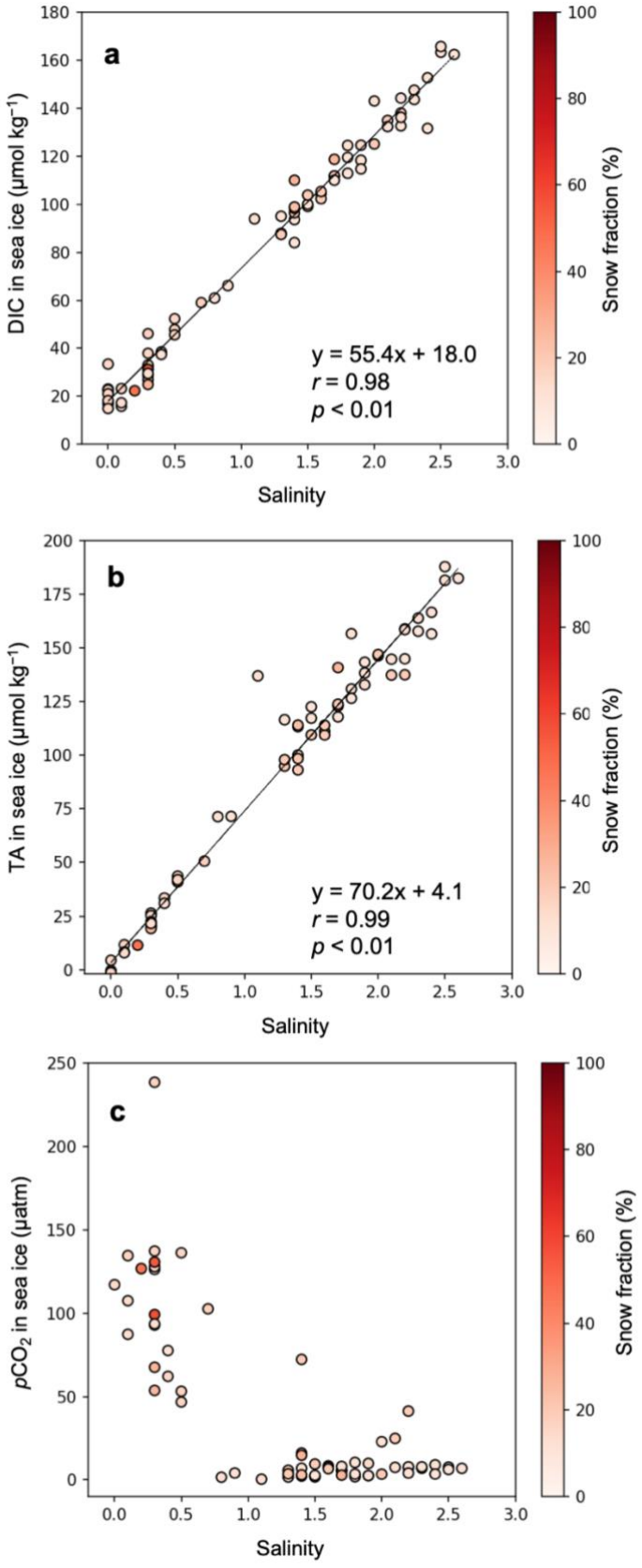

Figure 4.6. Relationship between salinity and (a) DIC and (b) TA in sea ice meltwater samples. (c) Relationship between salinity and pCO_2 calculated from the DIC and TA of sea ice meltwater. The color scales indicate the snow fraction in sea ice.

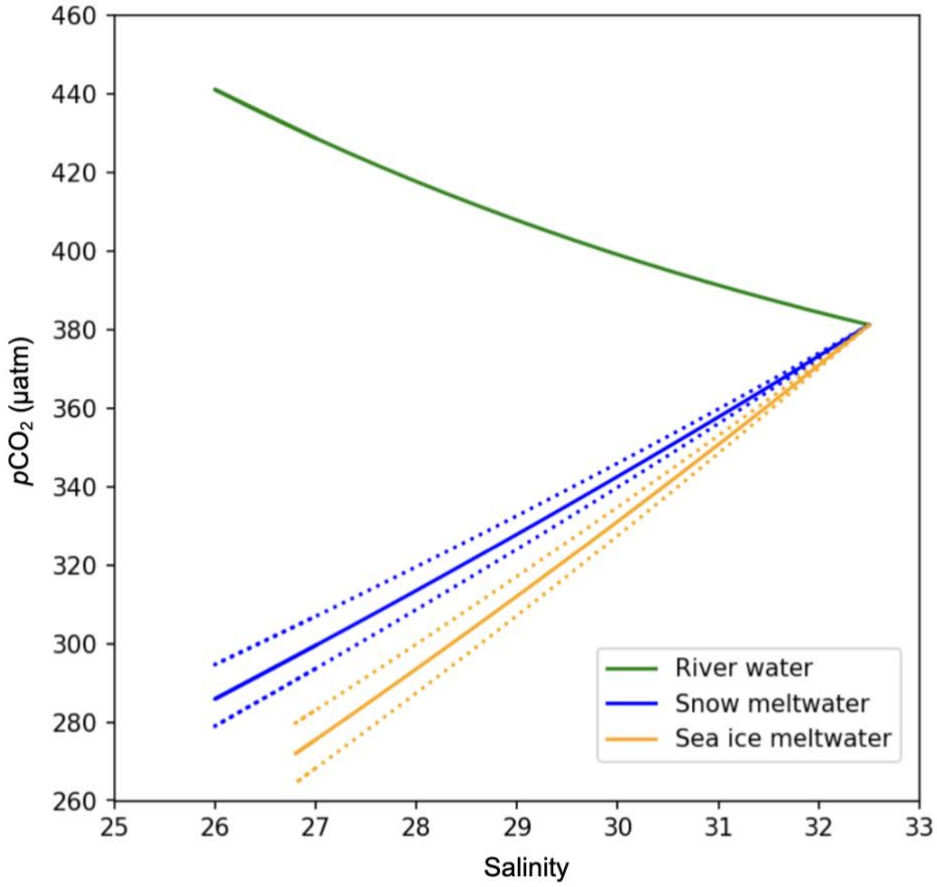

Figure 4.7. Relationship between salinity and the calculated pCO_2 for seawater mixed with freshwater of different types. Salinity and pCO_2 were calculated using the endmember value of each freshwater type (Table 4.2). Dotted lines indicate the maximum and minimum values of pCO_2.

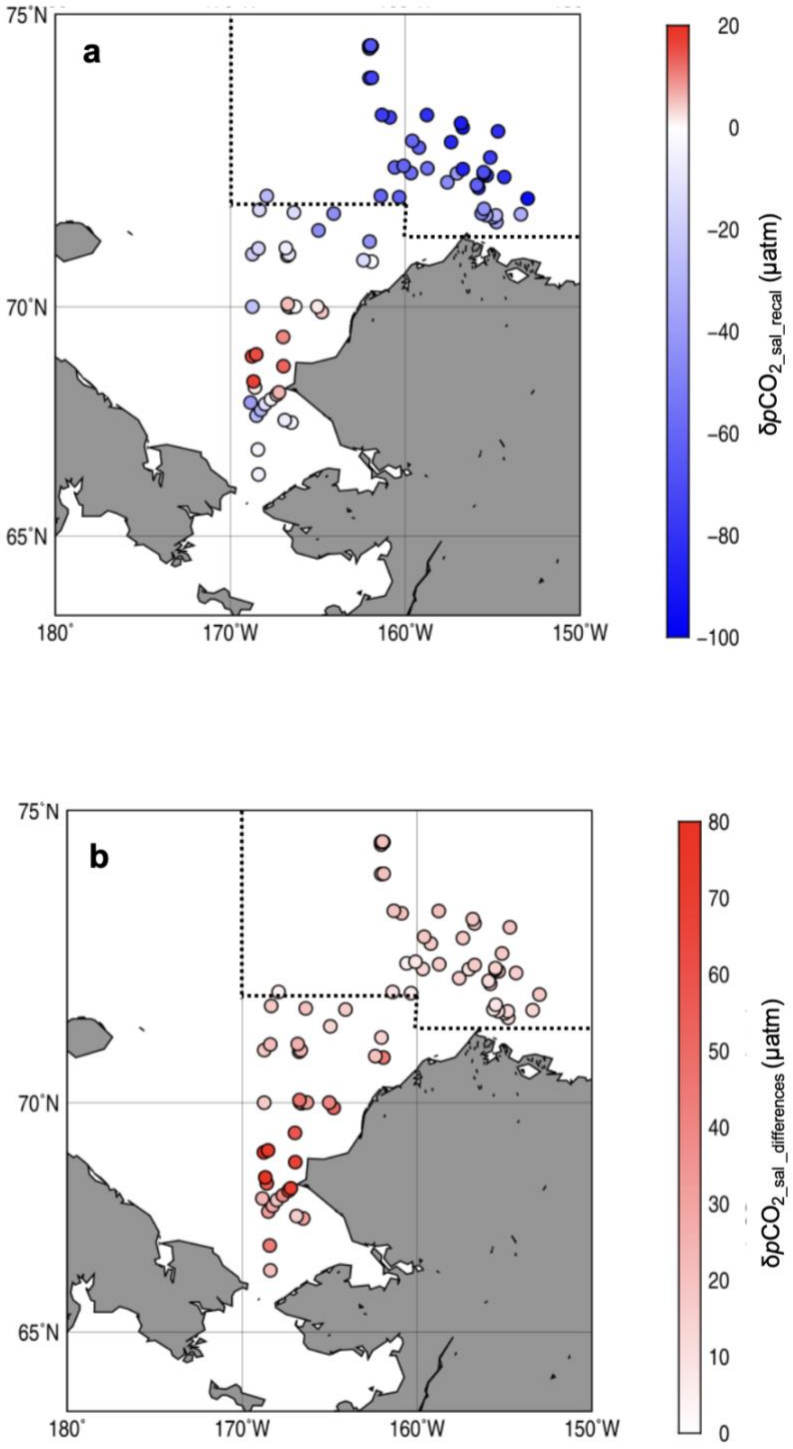

Figure 4.8. Spatial distributions of (a) $\delta pCO_{2\_sal\_recal}$, (b) $\delta pCO_{2\_sal\_differences}$ ($\delta pCO_{2\_CMSI\_sal\_recal} - \delta pCO_{2\_sal}$). The dotted line indicates the boundary between the Chukchi Sea and the Canadian Basin in this study.

Table 4.1 Endmember Values of Salinity and $\delta^{18}O$ used to Estimate Freshwater Fractions for Figure 4.5.

Water type	Salinity	$\delta^{18}O$ (‰)
Seawater	32.5 ± 0.2	−0.8 ± 0.1
Sea ice meltwater	4 ± 1	−2 ± 1.0
Meteoric water	0	−20 ± 2

Note: The seawater endmember was decided based on Yamamoto-Kawai et al. (2008).

Table 4.2 Endmember Values of Salinity, DIC, and TA Used to Calculate pCO_2 for Mixtures of Each Freshwater Type with Seawater for Figure 4.7.

Water type	Salinity	DIC (μmol kg^{-1})	TA (μmol kg^{-1})
Seawater	32.5	2168 ± 14	2269 ± 12
Alaskan river	0	1751	1628
Siberian river	0	885	816
Snow meltwater	0	18 ± 6	3 ± 10
Sea ice meltwater	4	240 ± 6	286 ± 10

Note: The seawater endmember value was obtained from the temperature minimum layer, and the sea ice and snow meltwater endmember values were determined from the regression lines in Figure 4.6. Alaskan (Yukon and Mackenzie) and Siberian rivers (Ob', Yenisey, Lena, and Kolyma) endmember values were taken from Tank et al. (2012) and Cooper et al. (2008). These river endmembers have no standard deviation because there were only a few values.

5. General Discussion

Previous studies of the factors contributing to changes in the carbonate system in the polar oceans have mostly quantitatively assessed changes of DIC or TA or qualitatively assessed changes of pCO_2. In this study, we suggested a new method to quantitatively assess the factors contributing to variations of pCO_2. The new method proposed in Chapter 2 allows us to estimate the changes of pCO_2 from winter to summer due to changes in water temperature, freshwater inflow, and biological activity, which are predicted to change with global warming in the future. In Chapter 4, the same method was successfully modified to enable its application to the Arctic Ocean by use of data for the Pacific sector of the Arctic Ocean.

By using the same method of assessment for both polar oceans, it is possible to examine the differences between the factors contributing to variations of pCO_2. The increase of pCO_2 due to changes of water temperature and the decrease of pCO_2 due to biological activity was very significant in both oceans. A difference between the two oceans was observed in terms of the influences of freshwater inflow. Freshwater in the Southern Ocean is mainly sea ice or glacial meltwater and was estimated based on salinity data. In contrast, as river water also flows into the Arctic Ocean, the impact of freshwater inflow was estimated based on the fraction calculated by using salinity and $\delta^{18}O$. Although there are some differences in the estimation methods due to the different types of freshwater, the resultant estimates are comparable. In the Southern Ocean, δpCO_{2_sal} was < -20 μatm, which is very small compared to the amount of change due to temperature changes and biological activity. In the Arctic Ocean, on the other hand, δpCO_{2_sal} was -100 to $+20$ μatm. Positive δpCO_{2_sal} values were found only for areas with river water inflow. Some stations with negative δpCO_{2_sal} values showed much larger decreases than those observed in the Southern Ocean. The indication was that the Arctic Ocean in September–October is more strongly affected by meltwater than is the Southern Ocean in December–February.

Chapter 3 presents the distribution of nutrients in the Southern Ocean. Nutrients in the eastern Indian Ocean sector of the Southern Ocean were determined by inflows of CDW and decomposition of organic matter, which were found to vary with ocean frontal structure. Chapter 2.4.5 suggests that changes of ocean surface xCO_2 from 1996 to 2018/19 may have been due in part to changes of nutrient concentrations associated with the southward shift of the SB of the ACC. These findings predict that future changes of ocean frontal structure associated with environmental change may alter the distribution of nutrients in the Southern Ocean and thereby lead to changes of

δpCO_{2_bio} and pCO_2.

In Chapter 4, the relationship between salinity and the carbonate system in Arctic Sea ice was investigated by using sea ice observation data for the Arctic Ocean. Previous studies have assumed that sea ice has zero salinity and zero DIC and TA. These characteristics would reduce pCO_2. However, our results show that sea ice with zero salinity also contains a small amount of DIC and TA, and that the balance of these components results in a relatively high pCO_2 in the meltwater of relatively low salinity ice. This result suggests that the type of melting sea ice greatly influences changes of sea surface pCO_2 and demonstrates the necessity of focusing on changes of the type of freshwater in future projections.

The new quantitative assessment methods for drivers of pCO_2 variations and findings about the surrounding environment proposed in this study will improve future predictions of pCO_2 in the polar oceans. In contrast, the fact that the estimation of δpCO_2 is based on winter data estimated from summer observations may cause errors in δpCO_2 estimation. In addition, because δpCO_{2_others} has the same absolute value as other δpCO_2 estimates, we need to improve this method and consider other drivers of pCO_2 variations. Therefore, year–round ocean observations, expansion of carbonate system observations including organic carbon, and expanded research on ocean–river interactions are required.

Acknowledgements

Firstly, I express my sincere gratitude to Associate Prof. Daiki Nomura for his enthusiastic guidance over the past six years. I also thank Prof. Atsushi Ooki, Prof. Hiromichi Ueno, Prof. Akihide Kasai, Associate Prof. Yutaka Isoda and Assistant Prof. Hiroji Onishi of the Department of Marine Environmental Science for their advice on my research.

For research in the Southern Ocean, I am grateful to Associate Prof. Hiroto Murase (Tokyo University of Marine Science and Technology), Prof. Shigeru Aoki (Institute of Low Temperature Science, Hokkaido University), Assistant Prof. Daisuke Hirano (National Institute of Polar Research), Dr. Hiroko Sasaki (Japan Fisheries Research and Education Agency), Dr. Shin-ichiro Nakaoka (National Institute for Environmental Studies) and Dr. Kaihe Yamazaki (University of Tasmania) for advice and discussions. For research in the Arctic Ocean, I am also grateful to Dr. Amane Fujiwara, Dr. Mariko Hatta, Dr. Akihiko Murata (Japan Agency for Marine-Earth Science and Technology) and Prof. Sayaka Yasunaka (Tohoku University) for their advice and discussions. In addition, I thank the crews and researchers on R/V *Kaiyo-Maru* and R/V *Mirai* for their support during the observations.

In addition, I am grateful to many researchers from the following national and international institutions who provided advice and guidance on research and observations: University of Tokyo, Tokai University, University of Tasmania (Australia), University of Calgary (Canada), University of Liège (Belgium), University of Tromsø (Norway), and Alfred Wegener Institute for Polar and Marine Research (Germany).

During my research life at the university, I was helped by many lab mates and had a great six years in the laboratory.

Finally, I express my sincere gratitude to my family for their support of my research activities.